

Hydrodynamic Phonon Transport and Phonon Transport Across Interfaces from First Principles

by

Xun Li

B.S., Energy Engineering, Zhejiang University, China, 2015

Submitted to the Graduate Faculty of the
Swanson School of Engineering in partial fulfillment
of the requirements for the degree of
Doctor of Philosophy

University of Pittsburgh

2021

UNIVERSITY OF PITTSBURGH

SWANSON SCHOOL OF ENGINEERING

This dissertation was presented

by

Xun Li

It was defended on

January 5, 2021

and approved by

Heng Ban, PhD, Professor, Department of Mechanical Engineering and Materials Science

Guofeng Wang, PhD, Professor, Department of Mechanical Engineering and Materials Science

Feng Xiong, PhD, Assistant Professor, Department of Electrical and Computer Engineering

Alan McGaughey, PhD, Professor, Department of Mechanical Engineering, Carnegie Mellon
University

Dissertation Director:

Sangyeop Lee, PhD, Assistant Professor, Department of Mechanical Engineering and Materials
Science

Copyright © by Xun Li

2021

Hydrodynamic Phonon Transport and Phonon Transport Across Interfaces from First Principles

Xun Li, PhD

University of Pittsburgh, 2021

The high demand of effective heat removal from electronic devices has drawn significant interests in exploring ultrahigh thermal conductivity materials and a better understanding of thermal transport across interfaces. We developed a deviational Monte Carlo method to study the phonon transport with a full phonon scattering matrix in time, real, and reciprocal spaces. Our method uses inputs from first-principles calculations and explicitly calculates the spatial variation of phonon distribution function, thus can accurately simulate time-space dependent heat transport in various materials.

Graphitic materials have ultrahigh thermal conductivities. The phonon transport in these materials is in the hydrodynamic regime, a new regime with unique thermal transport characteristics that are not possible in better known ballistic and diffusive regimes. The transport phenomena are fluid-like as can be seen in phonon Poiseuille flow, phonon Knudsen minimum, and second sound. We studied the characteristics of phonon Poiseuille flow in suspended graphene by introducing the concept of phonon hydrodynamic viscosity and proposed a decomposition framework to quantify the contribution from each transport regime. Also, we quantitatively predicted the transient propagation of second sound in bulk graphite and observed lattice cooling effect near the adiabatic boundary by pulse heating. Our studies provide fundamental insights on heat transport in ultrahigh thermal conductivity materials and phonon hydrodynamics in graphitic materials.

The interfacial transport phenomena have drawn significant interest but mostly been studied in the Landauer framework which neglects internal phonon scattering and non-equilibrium near the interface. This may explain the large discrepancy commonly observed between experimental data and theoretical predictions. The strong non-equilibrium is a result of complex interplay between the interface scattering and internal phonon scattering. This non-equilibrium distribution decays with distance from the interface and recovers to the bulk phonon distribution at a distance which we define as an effective interfacial region. We find that the internal phonon scattering within the interfacial region provides an important contribution to overall interfacial resistance. Our study provides insights into large discrepancies between experimentally measured interfacial resistances and those calculated from the Landauer formula, which are often found in the literature, thus providing a useful way to interpret experimental data.

Table of Contents

Acknowledgements.....	xvi
1.0 Introduction.....	1
1.1 High thermal conductivity materials	1
1.2 Hydrodynamic phonon transport.....	3
1.2.1 Internal phonon scattering and transport regimes	3
1.2.2 Characteristics of phonon hydrodynamics	6
1.2.2.1 Collective motion of phonons.....	6
1.2.2.2 Phonon Poiseuille flow	7
1.2.2.3 Second sound.....	8
1.3 Phonon transport across thermal interfaces	10
1.3.1 Interfacial thermal resistance	11
1.3.2 Experimental measurements	11
1.3.3 Theoretical models and calculations	13
1.3.3.1 The original Landauer formula	13
1.3.3.2 The modified Landauer formula	15
1.3.3.3 Model for interfacial transmissivity.....	17
1.3.4 Examining the theory	18
1.3.4.1 Large discrepancies between experiments and theories	18
1.3.4.2 Validity of DMM.....	19
1.3.4.3 Non-equilibrium phonons near the interface	22
1.4 Peierls-Boltzmann equation.....	24

1.4.1	General form	24
1.4.2	Full scattering matrix	25
1.4.3	Relaxation time approximation	26
1.4.4	Callaway's scattering model	27
1.5	Dissertation outline	28
2.0	Methodology	31
2.1	Full phonon scattering matrix from first principles	31
2.2	Deviational Peierls-Boltzmann Equation	32
2.2.1	Energy-based PBE	32
2.2.2	Deviational form of the PBE	33
2.3	Monte Carlo simulation	34
2.3.1	Defining simulation particles	35
2.3.2	Initialization	36
2.3.3	Advection	37
2.3.4	Phonon scattering	37
2.3.4.1	Internal phonon scattering	38
2.3.4.2	Boundary scattering	40
2.3.4.2.1	Periodic heat flux	40
2.3.4.2.2	Isothermal	42
2.3.4.2.3	Adiabatic	42
2.3.5	Cancellation of particles	45
2.3.6	Sampling of thermal properties	46
2.3.7	Validations	46

2.3.7.1	Infinitely large graphene at steady-state	47
2.3.8	Phonon transport across an interface.....	48
2.3.8.1	Scattering at the interface	49
2.3.8.2	Bulk phonon distribution at the boundaries.....	51
2.3.8.3	Self-consistent algorithm	53
3.0	Role of hydrodynamic viscosity on phonon transport in suspended graphene.....	55
3.1	Background.....	56
3.2	Failure of homogeneous boundary scattering.....	57
3.3	Phonon hydrodynamic viscosity from momentum balance equation.....	58
3.4	Characteristics of phonon Poiseuille flow	60
3.4.1	Temperature dependence of thermal conductivity	60
3.4.2	Sample width dependence of thermal conductivity	66
3.5	Transition from hydrodynamic to diffusive regimes	69
3.6	Conclusions	73
4.0	Crossover of ballistic, hydrodynamic, and diffusive regimes in suspended graphene	75
4.1	Background.....	75
4.2	Defining ballistic and scattered particles.....	77
4.3	Decomposition of thermal conductivity	80
4.4	Decomposition of shear stress	81
4.5	Transition from ballistic to hydrodynamic regimes	86
4.5.1	Semi-analytic solution of the PBE with the Callaway's scattering model	87
4.5.2	Phonon Knudsen minimum.....	87
4.6	Conclusions	91

5.0 Transient lattice cooling by propagation of second sound in graphite	93
5.1 Background.....	93
5.2 Dispersion and attenuation of second sound	94
5.3 Monte Carlo simulation of second sound.....	96
5.3.1 Sample geometry and boundary conditions	96
5.3.2 Simulation details.....	97
5.3.3 Comparison in different transport regimes	98
5.4 Transient lattice cooling at adiabatic center	100
5.5 Conclusion.....	103
6.0 Significant interfacial resistance from the scattering of non-equilibrium phonons	105
6.1 Method for evaluating the non-equilibrium	105
6.1.1 Symmetry of phonon distribution function	107
6.1.2 Local entropy generation.....	109
6.2 Effective interfacial region with strong non-equilibrium.....	110
6.3 Interfacial thermal resistance from MC.....	116
6.3.1 Total interfacial resistance assuming bulk thermal conductivity	116
6.3.2 Significant contribution from non-equilibrium phonons	119
6.4 Conclusions	120
7.0 Summary and future directions.....	122
7.1 Summary.....	122
7.2 Future directions.....	124
Bibliography	126

List of Figures

Figure 1 Different mechanisms of phonon scattering in the reciprocal space: (a) N-scattering, (b) U-scattering. The blue and red arrows represent wavevectors of phonons before and after scattering, respectively. The vector G is a primitive reciprocal lattice vector.	4
Figure 2 Propagation of a heat pulse in ballistic, diffusive, and hydrodynamic regimes.	9
Figure 3 Schematic of interfacial transport based on (a) Landauer formula and (b) modified Landauer formula.	15
Figure 4 MC simulation flow.	34
Figure 5 Accumulated thermal conductivity (left y-axis) and specularity of boundary scattering (right y-axis) as a function of phonon wavelength. The boundary scattering for phonons that carry most of the heat is diffuse, even with a very smooth edge (roughness of 0.1 nm).	44
Figure 6 Schematic of computational domain representing an infinitely large sample. Reproduced with permission from [16]. Copyright 2019 American Physical Society.	47
Figure 7 Thermal conductivity for an infinitely large graphene at different temperatures calculated from MC simulation and iterative solution. The error bars for MC results are smaller than the width of line. Reproduced with permission from [16]. Copyright 2019 American Physical Society.	48
Figure 8 Transmissivity from Si to Ge with different broadening factor in the Gaussian function.	50
Figure 9 Temperature dependence of thermal conductivity for different sample widths. The dashed lines represent the exponential fit of the results. Thermal conductivity increases faster than	

the ballistic case as temperature increases, indicating phonon Poiseuille flow. The exponent of temperature is obtained by fitting the data from 50 K to 80 K (5 μm and 10 μm) and from 50 K to 60 K (50 μm). Reproduced with permission from [89]. Copyright 2018 American Physical Society. 62

Figure 10 Temperature dependence of phonon viscosity and thermal conductivity. The phonon viscosity decreases with temperature, resulting in thermal conductivity increasing with temperature faster than the ballistic case. The exponent of temperature is obtained by fitting the data in the temperature range from 50 to 100 K. Reproduced with permission from [89]. Copyright 2018 American Physical Society. 63

Figure 11 Normalized heat flux profile at 50 K, for sample widths of 5, 10, and 50 μm . The displacements near the boundaries are not zero and increase as the width decreases. The non-zero displacements indicate slip boundary condition. Reproduced with permission from [89]. Copyright 2018 American Physical Society..... 64

Figure 12 Local thermal conductivity profile from the MC simulation under different conditions. (a) 100 K and 300 K for 10 μm wide sample, (b) sample widths of 10 μm and 50 μm at 100 K, and (c) sample widths of 0.1 μm , 1 μm , and 10 μm at 300 K. Reproduced with permission from [89]. Copyright 2018 American Physical Society. 66

Figure 13 Sample width dependence of thermal conductivity at 100 K and 300 K. The dashed lines represent the thermal conductivities for an infinitely large sample. The black solid line represents the ballistic case, where thermal conductivity is linearly proportional to a width. The thermal conductivity at 100 K superlinearly increases with a width, indicating the significant hydrodynamic regime. Reproduced with permission from [89]. Copyright 2018 American Physical Society. 68

Figure 14 Comparison of MFPs of N- and U-scatterings at 300 K. The filled circles are for U-scattering and the void circles are for N-scattering. Reproduced with permission from [89]. Copyright 2018 American Physical Society. 70

Figure 15 Comparison of thermal conductivity values with different boundary scattering models. Solid line is for spatially non-homogenous boundary scattering by MC simulation, and dashed line is for spatially homogenous boundary scattering. The difference between them shows the significance of the viscous damping effect. Reproduced with permission from [89]. Copyright 2018 American Physical Society. 71

Figure 16 Deviation of phonon distribution from equilibrium case from MC simulation of the PBE. The phonon distribution is sampled at the center of 1 μm wide sample at 300 K. The slope between two adjacent phonon states (circles) represent the drift velocity at the phonon state. Reproduced with permission from [89]. Copyright 2018 American Physical Society..... 73

Figure 17 A schematic picture of an infinitely long graphene sample for MC simulation. Reproduced with permission from [16]. Copyright 2019 American Physical Society..... 79

Figure 18 Ballistic and scattered particles contribution to total thermal conductivity with respect to sample width at 100 K. Reproduced with permission from [16]. Copyright 2019 American Physical Society. 80

Figure 19 The momentum balance at 100 K. The difference between the green and black lines represents the momentum destruction by U-scattering. Reproduced with permission from [16]. Copyright 2019 American Physical Society. 83

Figure 20 Normalized momentum destruction rates at different temperatures, (a) 100 K, (b) 200 K, and (c) 300 K. Dark blue, yellow, and light blue represent the ballistic, hydrodynamic,

and diffusive regimes, respectively. Reproduced with permission from [16]. Copyright 2019 American Physical Society. 85

Figure 21 The dimensionless thermal conductivity with respect to inverse Knudsen number assuming a Debye phonon dispersion model. ‘FS’ refers to the Fuchs-Sondheimer solution of the PBE assuming no N-scattering. Reproduced with permission from [16]. Copyright 2019 American Physical Society. 88

Figure 22 Thermal conductivity normalized by graphene sample width at 100, 200, and 300 K. Reproduced with permission from [16]. Copyright 2019 American Physical Society..... 89

Figure 23 Normalized thermal conductivity contributions from the ballistic and scattered particles at 100, 200 and 300 K. For (d-f), the y-axis is in log scale and W^{-1} dependence is shown as the dotted line for eye-guide. Reproduced with permission from [16]. Copyright 2019 American Physical Society. 90

Figure 24 The propagation and attenuation of second sound in graphite at 100 K. (a) The dispersion relation of second sound. (b) Theoretical speed of second sound. (c) The relaxation length of second sound..... 95

Figure 25 Schematic of a 3D graphite sample with thickness of 1 μm for the MC simulation. One quarter of the experimental setup is simulated, with adiabatic boundaries for the front, left, and top surfaces. The back, right, and bottom surfaces are at constant ambient temperature. 97

Figure 26 Temporal temperature responses in different transport regimes at 150 K (a) and 100 K (b)..... 99

Figure 27 Second sound signal from experiments and simulations at 80, 100, and 150 K. 101

Figure 28 Snapshots of temperature profile on the top surface of the graphite sample at 80 K. 102

Figure 29 MC results of the offset measurement with different distances between the pump and probe beams.	103
Figure 30 Temperature profiles for a Si/Ge system with length of 200 nm. The non-linear feature is clearly observed.....	106
Figure 31 Schematic of heat flux of deviation of distribution from local equilibrium. The red/blue shaded area represents the heat flux along $+x$ / $-x$ direction. The red and blue lines represent the heat flux based on actual phonon distribution along $+x$ and $-x$ direction, respectively.	108
Figure 32 Evaluation of symmetry of deviation of phonon distribution from local equilibrium.	111
Figure 33 Spectral heat flux from bulk phonon distribution and transmissivity for Si (a,c) and Ge (b,d). Dashed lines are for dividing different frequencies based on transmissivity.....	112
Figure 34 Quantification of non-equilibrium for systems with different lengths.	113
Figure 35 Local entropy generation rate. The horizontal dashed lines are bulk entropy generation values assuming internal phonon scattering with bulk distribution.	114
Figure 36 Quantification of non-equilibrium for systems with different lengths at (a) 500, (b) 700, and (c) 1000 K.	115
Figure 37 Local entropy generation rate at (a) 500, (b) 700, and (c) 1000 K.	115
Figure 38 Accumulated thermal conductivity as a function of phonon MFP for (a) Si and (b) Ge at different temperatures.	116
Figure 39 Temperature profiles for the Si/Ge interface from MC. The blue dashed lines are the temperature profiles with bulk thermal conductivities.	117
Figure 40 Interfacial thermal resistance from Landauer, modified Landauer, and MC.	118

Figure 41 Decomposition of total interfacial resistance from MC. The contribution from non-equilibrium phonons is significant..... 120

Acknowledgements

The past five and half years have been one of the most memorable experience in my life. It has been an eye-opening journey where I have not only gained scientific knowledge in the field of nanoscale heat transport but also learned what it takes to a successful life. I appreciate all the people I met and all the support I received through thick and thin.

First, I would like to thank my advisor, Prof. Sangyeop Lee. He made every effort to help me as a starter in research. I thank him for his countless valuable guidance and comments on my work, for being a constant source of inspiration, for being patient with me and always being there whenever I have a question. As a true scientist, he showed me how to conduct meaningful research and really make a contribution, which will definitely benefit my future career.

I also thank my committee members, Prof. Alan McGaughey, Prof. Heng Ban, Prof. Guofeng Wang, and Prof. Feng Xiong, for their precious comments and suggestions on my work. Especially, I thank Prof. Alan McGaughey for inviting me to his group meeting in CMU at the beginning of my PhD study. Over the years, I have learned a lot from all these discussions and made many friends. Also, I thank Prof. Guofeng Wang for the joint meetings we had at Pitt. I thank the supergroup family at CMU led by Prof. Alan McGaughey, Prof. Jon Manlen, Prof. Reeja Jayan, and Prof. Gerald Wang, where I enjoyed the multidisciplinary meetings as well as the parties with the friends.

I thank my lab mates in the Lee group, Amirreza Hashemi and Jinchen Han, and previous group members, Prof. Ruiqiang Guo and Dr. Hasan Babaei. They have provided many helpful questions and comments, and I have learned a lot from them. I will also remember and miss all the parties and trips we had.

I also thank my friends for the company and support during this journey. It's definitely a long list, but to name a few: Shuxin Yao, Kai Luo, for the lifelong friendship; Amirreza Hashemi, Jinchun Han, Ruiqiang Guo, Muhammad Tanveer Sharif, Li Shi at Pitt; and members in the supergroup at CMU including but not limited to Dipanjan Saha, Wee-Liat Ong, Francisco Ramirez and his wife Olga Soto, Xiaoman Wang, and the visiting scholars Cheng Shao, Bo Fu, and Qi Liang. These are the memories I will always treasure.

Last but not least, I thank my parents for the unconditional love and support. They are always the harbor of my ship, and the gas station of my car. Words cannot express enough my love and gratitude.

1.0 Introduction

Efficient energy usage is an important part of the development of modern technology. According to the annual report of energy consumption published by department of energy, a lot of heat gets tossed out in the form of waste heat. Understanding and manipulating heat flow is crucial for applications including waste heat harvesting, thermal barrier coating, and cooling of micron transistors. A good thermal management always requires improving the thermal conductivity of a bulk material to better conduct heat and engineering the thermal interfaces between different materials. Over the years, huge success has been achieved in investigating thermal transport process in high thermal conductivity materials and across thermal interfaces by both theoretical and experimental methods, such as first-principles based calculations¹⁻⁴ and thermoreflectance techniques⁵⁻⁷. However, there are still fundamental scientific interests in the topics due to the complex physics in the interaction among heat carriers and the interfaces⁸⁻¹⁰.

1.1 High thermal conductivity materials

Materials with high thermal conductivity are good candidates for applications including thermal management for electronic devices. These materials often follow four empirical rules based on their physical properties: 1) simple crystal structure, 2) strong atomic bonding, 3) light atomic mass, and 4) low anharmonicity¹⁰. Strong atomic bonding with light mass leads to high phonon frequencies and large group velocities, so that the phonons carry heat more efficiently. Low anharmonicity gives a reduced scattering phase space, which leads to a smaller number of

available scattering processes based on energy and momentum conservations. As a result, phonons experience less scattering and have longer lifetimes. Low anharmonicity of phonons could be due to many reasons such as a large bandgap between acoustic and optical phonons. Diamond generally satisfies these rules and has been known as the bulk material with the highest thermal conductivity, around 2000 W/m-K at room temperature. Thus, diamond thin film is widely used for thermal management.

Other carbon-based materials, like graphitic materials including graphene and graphite, are also good choices because of similar thermal properties and high availability. Graphene, a single layer material with carbon atoms forming a honeycomb lattice structure, has the record-breaking thermal conductivity up to 5300 W/m-K at 300 K when suspended and measured by micro-Raman spectroscopy¹¹. Even when supported by a substrate, the thermal conductivity of graphene can still reach 600 W/m-K at room temperature¹². Despite the difficulty in obtaining high quality sample in the fabrication process, the superior thermal conductivity makes graphene a promising candidate for thermal management applications.

While the first three empirical rules for high thermal conductivity apply for graphene, the flexural phonons in suspended graphene actually experience large anharmonicity¹³. The large anharmonicity is suggested by the diverging mode Grüneisen parameters and originated from the low dimensionality of the material. The phonons experience strong scattering, yet the thermal conductivity is high. It is revealed by *ab initio* calculations that the thermal transport in graphene and other two-dimensional materials is in the hydrodynamic regime^{13,14}, which is different from commonly known ballistic and diffusive transport.

1.2 Hydrodynamic phonon transport

Phonon transport regimes is distinguished by the types of phonon-phonon scattering. Phonon scattering includes defect scattering, boundary scattering, and phonon-phonon scattering. Defect scattering happens when there is a change of mass or force constants on atomic sites, for example an isotope or vacancy in a crystal. The physical boundaries of a sample may scatter phonons differently depending on boundary conditions. Phonon-phonon scattering is the internal process in thermal transport due to the anharmonic interatomic force constants. Two different types of internal phonon scattering dominate in ballistic, diffusive, and hydrodynamic phonon transport regimes.

1.2.1 Internal phonon scattering and transport regimes

In ballistic regime, there is no internal phonon scattering, and phonons fly with group velocities until hitting the boundary. The adiabatic boundary scattering is a valid assumption for boundaries parallel to a temperature gradient in a sample with finite size. Incidental phonons are reflected into the sample with partially or fully randomized directions, depending on the boundary condition. As a result, the boundary scattering destroys the net phonon momentum and is the only source of thermal resistance in ballistic transport.

The thermal transport in diffusive regime is governed by Fourier's law, where heat flux \mathbf{q} is related to temperature gradient ∇T by thermal conductivity κ . The thermal resistance is mainly caused by Umklapp scattering (U-scattering). As illustrated in Figure 1(b), U-scattering is a momentum-destroying process involving large wavevector phonons. After U-scattering, the travelling direction and the momentum of phonons are changed, causing thermal resistance in the

process. In diffusive regime, U-scattering is strong and occurs everywhere in the sample, relaxing phonons into local equilibrium Bose-Einstein distribution.

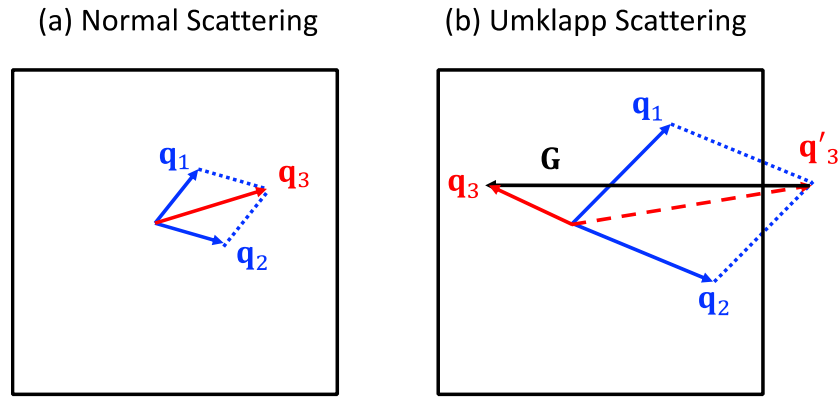


Figure 1 Different mechanisms of phonon scattering in the reciprocal space: (a) N-scattering, (b) U-scattering. The blue and red arrows represent wavevectors of phonons before and after scattering, respectively. The vector G is a primitive reciprocal lattice vector.

Hydrodynamic transport regime, on the other hand, is dominated by Normal scattering (N-scattering), making it distinguished from ballistic and diffusive regimes. As shown in Figure 1(a), N-scattering is a momentum-conserving process associated with small wavevector phonons. After N-scattering, the total momentum of phonons is conserved, and there is no direct thermal resistance in the scattering process.

Generally, the three different transport regimes occur at different ranges of temperature. Ballistic regime usually exists at low temperature or in a sample with sizes smaller than phonon mean free paths. In such cases internal phonon scattering is much weaker than boundary scattering. The thermal transport is limited by the size and shape of the sample. At relatively higher temperatures, internal phonon scattering becomes important and phonon mean free paths are smaller than the sample size. Since N-scattering mostly involves phonons with small wavevectors, it will be dominating over U-scattering, and the transport is in hydrodynamic regime. At high

temperatures when all the phonon states are occupied, U-scattering becomes significant and provides the major thermal resistance. The transport is in diffusive regime and can be described by the widely used Fourier's law. It is worth noting that there is not a clear boundary between the transport regimes, and in many realistic cases the characteristics of all three regimes coexist¹⁶.

The existence of hydrodynamic transport regime has been analytically and experimentally studied in bulk materials since more than fifty years ago¹⁷⁻²². These studies are carried out by examining the unique characteristics in the hydrodynamic regime, such as phonon Poiseuille flow and second sound, which will be explained later in more detail. The results validated the theory of hydrodynamic phonon transport and considered great triumph²³. However, these findings are only at extremely low temperatures. This is because in bulk materials, only at very low temperatures can U-scattering be frozen out such that N-scattering is relatively strong. Since then, the study on hydrodynamic phonon transport has been inactive because it is not considered as technologically relevant.

Recent advances in low dimensional materials make it possible to reconsider the importance of hydrodynamic phonon transport. The graphitic materials, including graphene, graphite, and carbon nanotubes (CNTs), have high Debye temperatures and large anharmonicity, both of which favor strong N-scattering. In these materials, it is recently found that phonon transport is in the hydrodynamic transport regime at significantly higher temperatures^{13,14}. It is found that the rate of N-scattering is larger than that of U-scattering by at least one order of magnitude. These studies have opened the door for studying hydrodynamic phonon transport in graphitic materials.

1.2.2 Characteristics of phonon hydrodynamics

N-scattering is similar to intermolecular scattering in fluid flow in a sense that the total momentum is conserved upon scattering in both of them. As a result, the phonon flow in ideal hydrodynamic regime is similar to fluid flow in terms of macroscopic behaviors.

1.2.2.1 Collective motion of phonons

In a fluid flow with a pressure gradient, molecules follow the displaced Boltzmann distribution with a drift velocity. Despite each molecule has its own velocity, all the molecules move collectively with the constant drift velocity due to the intermolecular interaction. Similarly, for a phonon flow driven by a temperature gradient with strong N-scattering, phonons show a collective motion with a drift velocity \mathbf{u} , and the equilibrium distribution is the displaced Bose-Einstein distribution

$$f_i^{\text{disp}} = \frac{1}{\exp\left[\frac{\hbar(\omega_i - \mathbf{q}_i \cdot \mathbf{u})}{k_B T}\right] - 1} \quad (1-1)$$

where i refers to a phonon state, \mathbf{q}_i is the phonon wavevector, ω_i is the phonon frequency, T is temperature, \hbar is the reduced Planck constant, and k_B is the Boltzmann constant. The drift velocity \mathbf{u} represents the displacement from the equilibrium Bose-Einstein distribution.

In ideal hydrodynamic regime, \mathbf{u} is constant for all phonon modes and much smaller than ω_i/\mathbf{q}_i . The displaced distribution can be expanded with respect to \mathbf{u} as

$$f_i^{\text{disp}} \approx f_i^{\text{eq}} + \frac{\hbar}{k_B T} f_i^{\text{eq}} (f_i^{\text{eq}} + 1) \mathbf{q}_i \cdot \mathbf{u} \quad (1-2)$$

where f_i^{eq} is the equilibrium Bose-Einstein distribution. It can be seen that \mathbf{u} is directly related to the properties of phonon flow such as momentum and heat flux. In ballistic and diffusive transport,

the value of \mathbf{u} is not a constant but depends on the specific phonon mode. It should also be noted that even with the presence of weak U-scattering, the drift motion of all phonons can still be observed¹³.

1.2.2.2 Phonon Poiseuille flow

For a hydrodynamic phonon flow in a sample with finite width, it resembles the fluid Poiseuille flow and is called phonon Poiseuille flow. In such situation, the diffuse boundary scattering provides direct thermal resistance, but it's impeded by strong N-scattering because the boundary is screened from phonons. This causes a gradient of heat flux, which is the smallest at the boundary and largest in the middle of the sample. As a result, the heat flux profile looks the same as the velocity profile in fluid Poiseuille flow and is a parabolic function of sample width. This feature of parabolic heat flux in the hydrodynamic regime clearly differs from that in the diffusive regime, where the local heat flux is constant across the sample since U-scattering happens homogeneously¹³.

Because of the dominance of N-scattering, thermal conductivity for phonon Poiseuille flow increases with temperature and sample width faster than that in the ballistic regime. This can be understood using the kinetic theory combined with a simple random walk theory^{19,24}. According to the kinetic theory, thermal conductivity is proportional to $C_V v L_{\text{eff}}$, where L_{eff} is the effective MFP of phonons, i.e., the total travel distance until a phonon particle encounters a momentum-destroying scattering process. In purely ballistic transport with fully diffuse boundary scattering, there is no internal phonon scattering, and L_{eff} is fixed at the characteristic size of a sample. Therefore, the thermal conductivity in this case follows the same trend of the ballistic thermal conductance with temperature and is linearly proportional to sample size. When the transport is in the ideal hydrodynamic regime, i.e., N-scattering is significantly strong and U-scattering is

negligibly weak compared to the diffuse boundary scattering, the boundary cannot be seen directly by phonon particles, but screened by many N-scattering processes. This circumstance can be roughly described by a random walk of phonon particles experiencing N-scattering processes. Then, L_{eff} is W^2/Λ_N , where W is the sample width and Λ_N is the MFP for N-scattering. As temperature increases, Λ_N decreases due to the increased N-scattering, making L_{eff} larger, while L_{eff} is a constant in the ballistic transport. Therefore, the thermal conductivity in the hydrodynamic regime changes with temperature faster and increases superlinearly with sample size. These unique dependences can be measured in experiments as the confirmation of the existence of hydrodynamic regime.

Past theoretical studies of the phonon Poiseuille flow in suspended graphene^{13,25,26} and graphite²⁷ showed sample size dependences of thermal conductivity that are different from ballistic case. However, they relied on a simplified Callaway's scattering model^{28,29} which cannot guarantee the accuracy in many cases. Also, some of them^{25,26} used an empirical relation for scattering rates that was developed for three-dimensional materials^{30,31}. These approximations to the scattering term hinder the quantitative guidance of future experimental efforts from first principles.

1.2.2.3 Second sound

In hydrodynamic regime, the response of the phonon system to a temporal perturbation is very different from that of ballistic and diffusive regimes. Let's consider a heat pulse applied at one end of the sample, which creates a high local phonon density. In ballistic regime where there is no interaction between phonons, phonons just fly with their group velocities. For graphitic materials, phonons have varied group velocities, thus the local phonon density will spread out and there is no significant temperature peak, as shown in Figure 2(a). In diffusive regime, strong U-

scattering destroys the net phonon momentum and scatters locally excited phonons to equilibrium distribution. As a result, the temperature pulse cannot propagate but gradually dies down, as shown in Figure 2(b). However, in hydrodynamic regime, N-scattering conserves net phonon momentum, creating a collective motion for phonons. Different phonons can travel together with drift velocity, despite they have different group velocities. The local phonon density wave can propagate along the sample with a well-maintained peak, as shown in Figure 2(c). An analogous phenomenon in fluid flow is the propagation of pressure pulse in real space, which is referred to as acoustic sound, while the propagation of temperature pulse in hydrodynamic regime is called second sound.

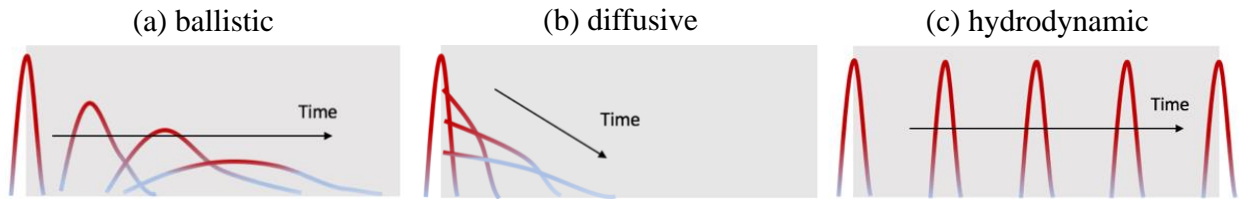


Figure 2 Propagation of a heat pulse in ballistic, diffusive, and hydrodynamic regimes.

For experimental confirmation of second sound, the most common method is a heat-pulse experiment^{22,32-34} where temporal temperature is detected with a distance from the location where a heat pulse is applied. Since the hydrodynamic regime is sensitive to temperature, different temperature signals will be observed at different ambient temperatures. Here we take a three-dimensional bulk material as an example. At low temperatures, internal phonon scattering is weak, and the temporal temperature response shows two clear peaks representing the ballistic transport of longitudinal and transverse phonons. At higher temperature when N-scattering becomes significant, a third temperature peak appears with the speed similar to theoretically calculated second sound speed. The third temperature peak is then considered second sound. At even higher temperatures when U-scattering dominates and destroys the collective motion, the second sound

peak disappears, and the temperature continues to increase. Second sound has been experimentally measured by this heat-pulse method in solid helium³², sodium fluoride^{22,33}, and bismuth³⁴ at extremely low temperatures. It is worth mentioning that second sound has recently been observed in graphite at much higher temperatures using a transient thermal grating experiment³⁵. In the experiment, second sound was observed through the shift of peak thermal expansion, different from the observation of the direct propagation in heat-pulse experiments.

1.3 Phonon transport across thermal interfaces

Thermal transport across the interfaces between solid materials has drawn significant interest due to its importance in applications including thermal management in electronic devices and energy conversion. As the device dimension shrinks to micro- and nano-scale due to the rapid miniaturization, the density of these thermal interface increases dramatically. When the size of a single thin film material becomes comparable or even smaller than the average phonon mean free path, the thermal transport is not only determined by the properties of the bulk material, but also the conditions of thermal interfaces. In these cases, the resistance brought by thermal interfaces may be larger than thermal resistance in the bulk material and plays a key role in the thermal transport in the devices. For applications where a fast heat dissipation is needed such as high-power transistors, the interfacial resistance needs to be reduced. For other applications where a large temperature gradient is desired such as thermal barrier coating, the thermal interface should be designed with large resistance. Due to the complex physical mechanisms around thermal interfaces brought by atomic structure mismatching, interaction among heat carriers, etc., a better understanding of interfacial resistance is still the center of research efforts³⁶.

1.3.1 Interfacial thermal resistance

When heat flows across an interface, the temperature discontinues at the interface due to the atomic mismatch between two solid materials. The interfacial thermal resistance R_{int} is calculated as the ratio of temperature drop ΔT at the interface and the heat flux q across the interface:

$$R_{\text{int}} = \frac{\Delta T}{q}. \quad (1-3)$$

The reverse of R_{int} is the thermal conductance G , or Kapitza conductance which was first measured experimentally between a solid and superfluid helium by Kapitza³⁷. The interfacial thermal resistance shows the ability of the system to dissipate or confine the heat across the interface, and has been studied both experimentally and theoretically for various interfaces between semiconductors, metals, amorphous materials, etc. Numerous past studies have shown great success in understanding and engineering the thermal interface, yet there are still fundamental questions unanswered because of the complex physics near the interface.

1.3.2 Experimental measurements

Since Kapitza's pioneering work, many experimental methods have been developed for measuring interfacial thermal conductance, which are systematically reviewed³⁸. Here we briefly discuss the methods that are most commonly used³⁹, which are the pump-probe thermoreflectance techniques including time-domain thermoreflectance (TDTR)^{5,40} and frequency-domain thermoreflectance (FDTR)⁴¹.

The main idea of both TDTR and FDTR is to heat a metal transducer layer with the thickness of around 100 nm on top of a substrate by a modulated pump laser beam and detect the surface temperature through the metal's reflectance by another probe laser beam. The obtained signals of reflectance are then fitted into thermal models to calculate thermal properties of the system. The difference is that in TDTR both lasers are pulsed with pulse width of 0.1 to 10 picoseconds, while in FDTR they are continuous wave with the pump laser modulated at different frequencies. Using these transient heating methods, the thermal penetration depth can be well controlled. The measurements can be sensitive to the interfacial thermal resistance as the thermal excitation can be localized to the immediate vicinity of the thermal interface³⁸.

In the measurements for interfacial thermal resistance by both methods, the thermal model is fitted with several free parameters to match detected signals^{5,40-43}. The interfacial thermal conductance is a direct fitting parameter to the ratio of in-phase and out-of-phase signals in TDTR^{5,40,42} and to the phase lag between the applied heat flux and the resulting temperature rise in FDTR^{41,43}. Other parameters that affect the fitting process include the thermal conductivity of the transducer layer and non-metal layer, the layer thickness, and the heat capacity.

The thermal conductivities for the interfacial layers or the substrate are usually the bulk values^{5,40,42-44}. For example, the fitted thermal conductivity of the thick SiO₂ layer in a TiN/SiO₂/Si system is identical to the bulk value^{40,44}. In some cases, the thermal conductivity of the metal transducer layer is determined through Wiedemann-Franz law with the measurements on electrical conductivity^{42,43} and is close to the bulk thermal conductivity at room temperature⁴². In other cases the thermal conductivities are directly set to bulk values for the metal transducer layer and the substrate⁴³. The layer thickness can also be experimentally measured^{40,42,43}, and the heat capacity

is usually set as bulk values^{40,42}. These measured or preset parameters are then used as known inputs to the fitting process.

1.3.3 Theoretical models and calculations

On the theoretical side, tremendous progress has been achieved since the pioneering work by Landauer⁴⁵ and Swartz⁴⁶ who proposed simple models to describe interfacial phonon transport. The fast-increasing computing power and the first-principles based calculations have contributed to the success of many theoretical methods including the solution to PBE, molecular dynamics (MD) simulations, atomistic Green's function, harmonic lattice dynamics calculations, and wave packet simulations. Despite their great success in understanding the fundamental physics near the thermal interface, the simple theoretical models proposed by Landauer and Swartz are still widely used especially as the references for experimental measurements.

1.3.3.1 The original Landauer formula

As shown in Eq. (1-3), the interfacial resistance is related to the heat flux and the temperature drop at the interface. The simple model Landauer proposed, originally for electron transport⁴⁵, assumes two materials are hot and cold heat reservoirs at constant temperatures, T_h and T_c , respectively, as shown in Figure 3(a). The net heat flux across the interface is then calculated by considering the heat flux in both directions as

$$q_x = \frac{1}{N_1 V_1} \sum_{i, v_{i,x} > 0} \hbar \omega_i v_{i,x} f_i^{\text{eq}}(T_h) t_{12i} + \frac{1}{N_2 V_2} \sum_{i, v_{i,x} < 0} \hbar \omega_i v_{i,x} f_i^{\text{eq}}(T_c) t_{21i} \quad (1-4)$$

where 1 and 2 represents different materials, N is the number of phonon states and V is the volume of the unit cell, $v_{i,x}$ is the group velocity in the heat transport direction for phonon state i , f_i^{eq} is

the local equilibrium Bose-Einstein distribution for phonon state i , and t_{12} (t_{21}) is the transmissivity from material 1 (2) to 2 (1). The transmissivity is a number from zero to unity that describes the possibility of the phonon transmitting across the interface and will be introduced in section 1.3.3.3. Knowing that the net heat flux should be zero if two materials are at the same temperature T_c , we have

$$\frac{1}{N_1 V_1} \sum_{i, v_{i,x} > 0} \hbar \omega_i v_{i,x} f_i^{\text{eq}}(T_c) t_{12i} + \frac{1}{N_2 V_2} \sum_{i, v_{i,x} < 0} \hbar \omega_i v_{i,x} f_i^{\text{eq}}(T_c) t_{21i} = 0, \quad (1-5)$$

and now Eq. (1-4) can be simplified to

$$q_x = \frac{1}{N_1 V_1} \sum_{i, v_{i,x} > 0} \hbar \omega_i v_{i,x} [f_i^{\text{eq}}(T_h) - f_i^{\text{eq}}(T_c)] t_{12i}. \quad (1-6)$$

Assuming a small temperature difference, the term $f_i^{\text{eq}}(T_h) - f_i^{\text{eq}}(T_c)$ can be expanded to the first order Taylor series, and Eq. (1-6) becomes

$$q_x = \frac{1}{N_1 V_1} \sum_{i, v_{i,x} > 0} \hbar \omega_i v_{i,x} \frac{\partial f_i^{\text{eq}}}{\partial T} \Delta T t_{12i} \quad (1-7)$$

and the interfacial thermal resistance is calculated as

$$R_{\text{int,E}} = \frac{\Delta T}{q_x} = \left[\frac{1}{N_1 V_1} \sum_{i, v_{i,x} > 0} \hbar \omega_i v_{i,x} \frac{\partial f_i^{\text{eq}}}{\partial T} t_{12i} \right]^{-1} \quad (1-8)$$

where the subscript E denotes the Landauer formula in the same way as in the literature⁴⁷. The equation can also be written in terms of the material 2 following the same procedure, and the interfacial resistance will be the same. This equation calculates the interfacial resistance in a simple way and has been widely used for many different systems^{5,40–42,44,46–49}.

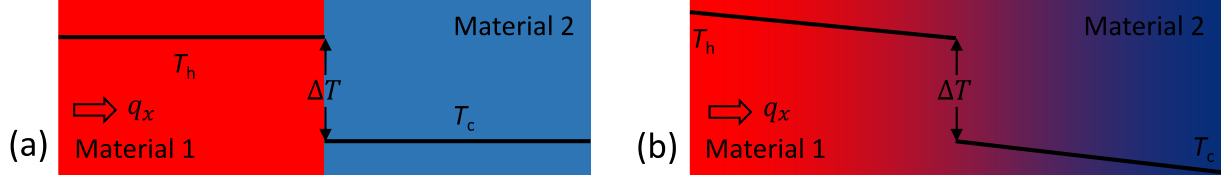


Figure 3 Schematic of interfacial transport based on (a) Landauer formula and (b) modified Landauer formula.

However, the limitation of Landauer formula is also well-known. It gives a non-zero interfacial resistance when the transmissivity t_{12} is unity which is true for a perfect crystal without thermal interface⁵⁰. In such case the interfacial resistance should be zero, and the non-zero value by Eq. (1-8) is due to the assumption of equilibrium distribution in both materials. This assumption ignores all the factors that could lead to a non-equilibrium distribution such as the interfacial scattering, the internal phonon scattering, and the complex interplay between them.

1.3.3.2 The modified Landauer formula

To replace the crude assumption in original Landauer formula that two materials are held at constant temperatures, it is natural to assume a temperature gradient due to internal phonon scattering, as shown in Figure 3(b). A modified Landauer formula was proposed by Simons⁵⁰ and generalized by Chen⁵¹ and Landry and McGaughey⁴⁷ to replace the equilibrium Bose-Einstein distribution with the bulk distribution which is for an infinitely large sample under a constant temperature gradient. The bulk distribution with a commonly used homogenous approximation and relaxation time approximation (to be introduced in section 1.4.3) is given as:

$$f_i = f_i^0 - \tau_i \mathbf{v}_i \frac{\partial f_i^0}{\partial T} \frac{dT}{dx}. \quad (1-9)$$

Now if we replace the equilibrium distribution in Eq. (1-4) with the bulk distribution for each material, and follow the same derivation (note that dT/dx is zero in both materials if they are at

the same temperature), we end up with the interfacial thermal resistance for the bulk distribution as

$$R_{\text{int,B}} = R_{\text{int,E}} \left[1 - \frac{1}{N_1 V_1 \kappa_1} \sum_{i, v_{x,i} > 0} \hbar \omega_i \tau_i v_{x,i}^2 \frac{\partial f_i^{\text{eq}}}{\partial T} t_{12i} - \frac{1}{N_2 V_2 \kappa_2} \sum_{i, v_{x,i} < 0} \hbar \omega_i \tau_i v_{x,i}^2 \frac{\partial f_i^{\text{eq}}}{\partial T} t_{21i} \right] \quad (1-10)$$

where κ is the bulk thermal conductivity. In the derivation, the diffusive transport is assumed by applying $q_x = -\kappa_1 \left(\frac{dT}{dx} \right)_1 = -\kappa_2 \left(\frac{dT}{dx} \right)_2$.

The modified Landauer formula gives reasonable results between highly similar materials with a zero $R_{\text{int,B}}$ when t_{12} and t_{21} are set to unity which means no thermal interface. The interfacial resistance is much smaller than that from the original Landauer formula, and has been compared with MD simulations^{50,49}. It is found that the thermal resistance from the modified Landauer formula is significantly less than the MD-predicted values for a Si/Ge interface, and the difference is attributed to the inaccuracy of the assumption of bulk phonon distribution on both sides of the interface⁴⁷. The assumption of bulk distribution near the interface is invalid because of the non-equilibrium introduced by the interface. When phonons strike the interface and are partially (or fully) reflected backwards, the distribution significantly changes into a non-equilibrium distribution. The modified Landauer formula, although more advanced than the original one by considering internal phonon scattering, ignores this non-equilibrium effect which can be significant when the reflection of phonons at the interface is frequent.

1.3.3.3 Model for interfacial transmissivity

To calculate the resistance from either the Landauer or the modified Landauer formula, the transmissivity (or called transmission coefficient) is needed which describes the probability for phonons to across the interface. Two models have been extensively used depending on the conditions of the interface: the acoustic mismatch model (AMM) and the diffuse mismatch model (DMM).

The AMM was first proposed by solving the continuum elasticity equations for the acoustic transmission and reflection⁵². In this model, the interface is treated as a specular boundary and the resistance comes from the mismatch of acoustic sound speeds between two materials. The transmissivity for phonons across the interface, ignoring the complex mode conversions and the incident angle, is simply written as

$$t_{12} = \frac{4\rho_1 c_1 \rho_2 c_2}{(\rho_1 c_1 + \rho_2 c_2)^2} \quad (1-11)$$

where ρ is the material mass density and c is the speed of sound. The assumption of a specular interface is appropriate for long wavelength phonons as they are typically less affected by an interface. The AMM has successfully predicted the interfacial resistance at cryogenic temperatures below 30 K where long wavelength phonons dominate the thermal transport⁴⁶. At higher temperatures, the AMM fails as the specular reflection or refraction at the interface is not valid anymore even for perfect interfaces. Phonons at elevated temperatures experience diffuse reflection by the interface, which is well described by the diffuse mismatch model (DMM).

The DMM has been the most commonly used model since proposed 30 years ago⁴⁶. The model states that phonons experience diffuse scattering at the interface and lose the memory of their initial status except the frequency (the assumption of elastic scattering). Thus, the

transmissivity from material 1 to 2 is related with that from material 2 to 1, and is a function of phonon frequency as

$$t_{12}(\omega) = 1 - t_{21}(\omega). \quad (1-12)$$

The detailed balance is applied for each frequency:

$$\begin{aligned} t_{12}(\omega) \frac{1}{N_1 V_1} \sum_i \hbar \omega_i f^{\text{eq}} |v_{i,x}| \delta(\omega_i - \omega) \\ = t_{21}(\omega) \frac{1}{N_2 V_2} \sum_j \hbar \omega_j f^{\text{eq}} |v_{j,x}| \delta(\omega_j - \omega) \end{aligned} \quad (1-13)$$

where the δ function sets the constraint on phonon frequency. The spectral transmissivity is calculated as

$$t_{12}(\omega) = \frac{\frac{1}{N_2 V_2} \sum_j |v_{j,x}| \delta(\omega_j - \omega)}{\frac{1}{N_1 V_1} \sum_i |v_{i,x}| \delta(\omega_i - \omega) + \frac{1}{N_2 V_2} \sum_j |v_{j,x}| \delta(\omega_j - \omega)}. \quad (1-14)$$

The DMM is more accurate than AMM at noncryogenic temperatures or rough interfaces. In these cases, the wavelengths of thermal phonons are comparable or shorter than the roughness of the interface, thus the phonons are mainly reflected randomly.

1.3.4 Examining the theory

1.3.4.1 Large discrepancies between experiments and theories

The theory of Landauer formula combined with DMM has been widely used for predicting interfacial thermal resistance and comparing with experimental measurements^{5,7,36,38,40,42,44,53-59}. Some studies have shown good agreements for metal/semiconductor interfaces^{53,54,59}, however, they are most likely to be coincident because of the crude assumptions in DMM that ignore the complex physics near the interface³⁶. In many other studies, large discrepancies between

experimental measurements and the Landauer theory with DMM have been observed for various interfaces between metals, metal alloys, metal dioxides, and semiconductors^{5,40,42,44,56}. The experimentally measured interfacial resistances are generally several times larger than those predicted by the theory. Many efforts have been put to explain the discrepancies focusing on the validity of DMM for the interfacial transmissivity.

1.3.4.2 Validity of DMM

As discussed in section 1.3.3.3, the DMM requires knowledge of harmonic phonon properties. A poor description of phonon dispersion may lead to incorrect transmissivity. One explanation for the large difference between theoretical interfacial resistances and the early measurements by 3- ω ⁴⁴ and TDTR⁴⁰ methods is that the Debye model was used for phonon dispersion relation, which cannot capture the mode dependent group velocities, especially at high temperatures. Although an accurate phonon dispersion can be calculated from first-principles, the crude assumptions in the DMM still make it difficult to compare the results with experimental measurements directly. Firstly, the DMM ignores complex disorder commonly induced near the interface such as segregation of elements and strain field. For a realistic interface, atomic structure is rarely crystalline-like due to defects in the material (point defect, grain boundary, etc.) and the strain caused by atomic mismatch between two materials. Secondly, only elastic interfacial scattering is allowed, and high frequency phonons cannot cross the interface if there are not available phonons with the same frequency on the other side. Due to these assumptions in DMM, there have been many discussions on the validity and accuracy of the model.

Past MD studies have shown that considering the realistic atomic structure at the interface is important because there exist interfacial phonon modes that are different from bulk phonon modes⁶⁰⁻⁶². Gordiz and Henry defined the interfacial phonon modes by comparing the eigen modes

near the interface and in the bulk material. They found that 15% of the total conductance for an interface between Si and Ge comes from the interfacial modes that are less than 0.1% of the total modes. Feng *et al.*⁶² distinguished the interfacial and bulk modes in a Si/Ge system by calculating local phonon density of states (DOS). By calculating mode contribution to interfacial conductance, they found that the interfacial modes enable inelastic scattering for bulk phonon modes in Si and Ge by serving as a bridge, and the resulting inelastic transport can contribute more than 50% of total conductance. These studies identified the interfacial modes and emphasized the importance of them to interfacial thermal conductance. However, these interfacial modes exist only within several atomic layers near the interface, which means their influence is limited to several angstroms in the bulk materials. For a large system with the size of several micrometers, whether the effect of the interfacial modes is still significant is not clear.

To consider the atomic disorder at the interface, the atomic Green's function (AGF) has been applied to study the phonon transmission across the interface^{63,64}. In AGF, the sample is usually divided into two contacts (semi-infinite bulk materials) and one device (the interface with realistic atomic structures). Lattice dynamics calculations are performed for the contacts and devices to obtain the dynamical matrix, which is then used to calculate the transmission coefficient for the interface. The AGF in principle describes the realistic interface as it is and the force constants can be calculated from first-principles⁶⁵, thus it is considered more accurate than DMM. There is still assumption made in AGF, for example, the interfacial scattering is limited to elastic where the frequency of transmitted phonon does not change, and that there is no anharmonicity in bulk materials that introduces internal phonon scattering. It is worth pointing out that an anharmonic AGF that considers internal phonon scattering has been recently developed for three-dimensional interfaces and the interfacial conductance is improved⁶⁶.

Inelastic interfacial scattering has been examined and shown to be less important than other mechanisms such as internal phonon scattering. To address the effect of inelastic interfacial scattering, Hopkins *et al.*^{67,68} proposed models that go beyond the elastic limit and include energy exchange among three or more phonons at the interface. These models gave improved agreements between calculations and experiments. However, these models do not consider the selection rules for momentum conservation for phonon scattering³⁶ and lack physical explanation. Nevertheless, the inelastic interfacial scattering has been suggested to be important as a linear increase in interfacial conductance with temperature has been observed in both simulations and experiments^{47,69-71}. However, it is not clear to distinguish the inelastic interfacial scattering from internal phonon scattering which is also inelastic and strengthened by increasing temperature. Although inelastic scattering enabled by the interfacial modes was found to be important in previous MD simulations^{61,62}, the effect is much weaker than internal phonon scattering in the bulk materials⁷². Wu and Luo⁷² found that the anharmonicity inside bulk materials has much large impact on interfacial conductance than the anharmonicity at a solid-solid interface through MD simulations. Murakami *et al.*⁷³ calculated spectral phonon transmission for two thermal interfaces by MD simulations to examine the effect of inelastic interfacial scattering. They concluded that the contribution from inelastic channels is severely limited by internal phonon scattering within a close distance from the interface. Cheng *et al.*⁷⁴ recently measured the conductance for a high-quality aluminum and sapphire interface and found that elastic interfacial scattering dominates other mechanisms on the transport process.

Internal phonon scattering in the bulk material can also affect the thermal transport across an interface. It has been included in the modified Landauer formula⁵⁰ and is shown to decrease the interfacial resistance^{47,49}. The effect of internal phonon scattering has been investigated using

AGF⁶⁶, MD^{72,73,75,76}, and the PBE⁷⁷. While phonons with frequencies higher than the maximum frequency in the other material cannot cross the interface under the assumption of elastic interfacial scattering, internal scattering provides additional channels for them⁷⁷. High frequency phonons decay into multiple low frequency phonons through scattering, and these low frequency phonons transfer the energy across the interface. As a result, the interfacial resistance is reduced. The inelastic nature in internal phonon scattering enables high frequency phonons near the interface to travel across the interface, even in DMM or other models where only elastic interfacial scattering is allowed.

1.3.4.3 Non-equilibrium phonons near the interface

While the validity of DMM has been extensively studied, the Landauer theory and its modified version have been widely used with much less doubt. Both of them assume that phonons are at local equilibrium throughout the system, following Bose-Einstein distribution and bulk distribution, respectively. However, these assumptions fail to describe the non-equilibrium phonon distribution near the interface. When phonons transmit through or are reflected by the interface, which is referred to as interfacial phonon scattering, their phonon states are randomly redistributed. Thus, phonons coming toward the interface and going away from the interface follow different distribution, and this difference causes non-equilibrium phenomena. The non-equilibrium has been observed in previous studies using solutions to the PBE^{78,79} and MD simulations^{62,80–83}. A non-linear temperature profile has been found near the interface as a result of non-equilibrium. It has been suggested that different phonon modes can have different local temperatures based on their phonon frequencies^{62,78,80,81}, phonon branches^{62,81,82}, or even phonon states^{62,81}. These studies also showed that non-equilibrium impedes the thermal transport process, because of a largely reduced temperature drop at the interface for acoustic phonons based on their modal temperatures⁶². A non-

equilibrium Landauer approach was proposed⁸³ where phonons near the interface have modal equivalent equilibrium temperatures that include the effect of phonons coming from the interface. They combined this approach with the DMM and obtained interfacial resistance between metals and semiconductors that agree well with experimental measurements. These studies provided good ways to examine the effect of non-equilibrium.

However, it is not physically clear if phonons of the same frequency, phonon branch, or phonon state should have the same local temperature, which is the assumptions of previous studies. Phonons with the same frequency or phonon branch can have quite different internal phonon scattering rates due to the requirement of energy and momentum conservations upon scattering, thus they may not be relaxed at the same time. Even for phonons with the same phonon states, different local spatial positions will lead to different temperatures. More importantly, the concept of temperature is only well-defined at thermodynamic equilibrium. When non-equilibrium exists, the temperature is usually calculated as a temperature that can lead to the same local internal energy in the equilibrium case. While the equivalent temperature may reflect the average thermal property, it cannot describe the detailed transport process on a phonon mode basis. Thus, the effect of non-equilibrium on thermal transport may need to be carefully examined without using the concept of equivalent temperature.

The entropy generation is a good measure of thermal resistance even the system is at non-equilibrium. For a heat flow \dot{Q} at temperature T across a control volume of volume V with a small temperature difference ΔT (small deviation from equilibrium), the entropy generation rate can be calculated as

$$\dot{S} = \frac{1}{V} \left(\frac{\dot{Q}}{T} - \frac{\dot{Q}}{T + \Delta T} \right). \quad (1-15)$$

With Taylor expansion to the first order, Eq. (1-15) can be written as

$$\dot{S} = \frac{q}{T^2} \left(-\frac{dT}{dx} \right). \quad (1-16)$$

The entropy generation rate is also a measure of thermal resistance R if we use the fact that resistance is the ratio of temperature drop and the heat flux:

$$\dot{S} = \frac{A q^2}{V T^2} R \quad (1-17)$$

where A is the cross-section area. For diffusive thermal transport in bulk materials with a linear temperature profile, Eq. (1-16) gives a constant entropy generation rate, indicating the thermal resistance is uniform too. This is true because internal phonon scattering is dominating and not dependent on spatial position. For phonon transport across a thermal interface, however, a larger thermal resistance near the interface is expected because of additional interfacial scattering. Thus, Local entropy generation is a better measure of the effect of non-equilibrium and can directly show local thermal resistance.

1.4 Peierls-Boltzmann equation

1.4.1 General form

The Peierls-Boltzmann transport equation (PBE) is the governing equation of phonon flow based on the assumption of phonon gas particles. The general form of the PBE is

$$\frac{\partial f_i(\mathbf{r}, t)}{\partial t} + \mathbf{v}_i \cdot \nabla_{\mathbf{r}} f_i(\mathbf{r}, t) = \left[\frac{\partial f_i(\mathbf{r}, t)}{\partial t} \right]_{\text{scatt}} \quad (1-18)$$

where f_i is the phonon distribution at the phonon state i , \mathbf{v}_i is the group velocity of phonons at the state i , \mathbf{r} is the position vector in the three-dimensional real space, and t is time. The PBE describes the balance of the change of phonon distribution (the first term) due to phonon advection (the second term) and phonon scattering (the third term). The advection term represents the change of phonon distribution in the real space in the presence of a temperature gradient by allowing phonons travel with their velocities. The scattering term describes the change of phonon distribution in the reciprocal space due to the scattering among phonon states. The explicit form of the scattering term is presented by a full scattering matrix that includes all the scattering events. The full scattering matrix is accurate in describing internal phonon scattering but makes the solution to the PBE more difficult. A more detailed explanation for the full scattering matrix along with several simplifications will be discussed in the following sections.

1.4.2 Full scattering matrix

The PBE with a full scattering matrix is written as

$$\frac{\partial f_i(\mathbf{r}, t)}{\partial t} + \mathbf{v}_i \cdot \nabla_{\mathbf{r}} f_i(\mathbf{r}, t) = \sum_j C_{ij} f_j(\mathbf{r}, t) \quad (1-19)$$

where C_{ij} is the element of scattering matrix \mathbf{C} showing the rate of scattering from phonon state j to i . The scattering matrix can be calculated from first-principles, which will be briefly introduced in section 2.1.

The scattering matrix naturally includes both N- and U-scattering, making it the most accurate in describing internal phonon scattering. However, the accuracy comes with the cost of

computational effort. The PBE with scattering matrix is an integrodifferential equation, with an integral term in the reciprocal space and differential terms in the time and real space domains. The solution exists in seven dimensions, which makes it very challenging to solve analytically. The equation has been simplified for steady-state phonon transport in an infinitely large sample assuming a constant temperature gradient and a small deviation from equilibrium state:

$$\mathbf{v}_i \cdot \nabla_{\mathbf{r}} f_i^{\text{eq}} = \sum_j C_{ij} f_j. \quad (1-20)$$

The spatial varying phonon distribution in the advection term is replaced with a homogeneous distribution. The advection term can be directly calculated, and the equation becomes a homogeneous integral equation. The equation has been solved by the iterative method⁸⁴ and the variational method⁸⁵.

However, for problems that require spatial resolution of phonon distribution, the assumptions mentioned above are not valid and Eq. (1-20) fails for describing the phonon transport. Such problems include the phonon transport in the hydrodynamic regime, with phonon Poiseuille flow where the heat flux shows a spatial dependence, and second sound where a temporally and spatially varying phonon distribution is needed. To solve the PBE with scattering matrix without any assumptions, several methods have been developed such as the solution based on the eigenstates of the scattering matrix⁸⁶, the eigendecomposition method⁸⁷, and the Monte Carlo (MC) method^{88,89}.

1.4.3 Relaxation time approximation

As the PBE with scattering matrix is difficult to solve, another simplification is made on the scattering term called relaxation time approximation (RTA). In RTA, the off-diagonal terms in

the scattering matrix are set to zero, eliminating the coupling between different phonon states. As a result, the PBE with RTA at steady-state is written as

$$\mathbf{v}_i \cdot \nabla_{\mathbf{r}} f_i = -\frac{f_i - f_i^0}{\tau_i} \quad (1-21)$$

where f_i^0 is the equilibrium Bose-Einstein distribution at local temperature T_0 , and τ_i is the lifetime for phonon state i . The RTA describes the independent relaxation process of each phonon state within the lifetime τ_i , which means that the corresponding phonon state exhibits relaxation from the non-equilibrium distribution to the equilibrium distribution while all other phonon states are kept at equilibrium. The RTA eliminates the integration in the scattering term and can be easily solved analytically. It can be seen from Eq. (1-21) that all the scattering processes bring the distribution to the equilibrium Bose-Einstein distribution, so there is no distinguish between N- and U-scattering. The RTA is a good approximation for phonon transport in materials with low thermal conductivity, or at extremely high temperatures where U-scattering is the dominant scattering mechanism. For materials with high thermal conductivity or lower dimensionality, the RTA is likely to fail because N-scattering becomes important in internal phonon scattering.

1.4.4 Callaway's scattering model

When N-scattering is significant compared to U-scattering, the PBE with RTA cannot properly describe phonon transport since N-scattering scatters phonons into the displaced Bose-Einstein distribution f^{disp} . Based on this idea, Callaway proposed a scattering model in which N- and U-scattering relax the distribution into f^{disp} and f^0 , respectively²⁸. The steady-state PBE with Callaway's scattering model is thus written as

$$\mathbf{v}_i \cdot \nabla_{\mathbf{r}} f_i = -\frac{f_i - f_i^{\text{disp}}}{\tau_{i,N}} - \frac{f_i - f_i^0}{\tau_{i,U}} \quad (1-22)$$

where $\tau_{i,N}$ and $\tau_{i,U}$ are the lifetimes for phonon state i for N- and U-scattering, respectively. This model was developed initially from intuition, but was later proved analytically¹⁷. Eq. (1-22) provides solution to phonon transport when N-scattering is strong and cannot be ignored, and has been solved by a discrete ordinate method²⁶ and a MC simulation⁹⁰. Despite its success in certain situations, the PBE with Callaway's scattering model is not accurate for a quantitative purpose particularly when neither N- nor U-scattering is significantly stronger than the other^{29,91}.

1.5 Dissertation outline

This dissertation discusses the fundamental physics of phonon transport in bulk graphitic materials characterized by hydrodynamic phonon transport and across thermal interfaces. Chapter 2 introduces the deviational MC method to solve the PBE. Chapters 3 and 4 focus on the hydrodynamic regime in suspended graphene, and Chapter 5 discusses transient hydrodynamic phenomenon in graphite. Chapter 6 provides physical understanding of phonon transport between crystalline silicon and germanium.

Chapter 3 discusses the peculiar temperature and sample width dependences of thermal conductivity in suspended graphene. We show that thermal conductivity increases as T^α where α ranges from 1.89 to 2.49 depending on the sample width at low temperatures, much larger than 1.68 of the ballistic case. The thermal conductivity has a width dependence of $W^{1.17}$ at 100 K, clearly distinguished from the sublinear dependence of the ballistic-diffusive regime. These peculiar features are explained with a phonon viscous damping effect of the hydrodynamic regime.

We derive an expression for the phonon hydrodynamic viscosity from the Peierls-Boltzmann equation, and discuss that the phonon viscous damping explains well those peculiar dependences of thermal conductivity at 100 K. The phonon viscous damping still causes significant thermal resistance when a temperature is 300 K and a sample width is around 1 μm , even though the hydrodynamic regime is not dominant over other regimes at this condition.

Chapter 4 proposes a framework to distinguish three phonon transport regimes when none of them is dominant. In many cases, the transport cannot be characterized by a single regime, but the features of all three regimes – ballistic, hydrodynamic, and diffusive regimes – exist to some extent. Here we assess the extent of three regimes by comparing momentum destruction rates by three different mechanisms, each of which represents a different regime: diffuse boundary scattering without internal phonon scattering (ballistic regime), diffuse boundary scattering combined with normal scattering (hydrodynamic regime), and umklapp scattering (diffusive regime). We sample distribution functions of ballistic and scattered particles separately, and thereby compare the momentum destruction rates by the three different mechanisms. This framework helps us identify the major transport characteristics when transport phenomena are complex. Using this framework, we also discuss a well-known phenomenon of ballistic-to-hydrodynamic crossover, called phonon Knudsen minimum.

Chapter 5 presents the propagation of second sound in bulk graphite. We theoretically calculate the dispersion of second sound from wave equations and determine the optimal conditions for the propagation of second sound. These conditions include the duration of laser pulse, the distance between pump and probe beams, etc. We simulate the heat pulse measurement for a 3D crystalline graphite using our MC simulations. We observe strong signal of second sound propagation that is clearly different from ballistic and diffusive transport. The evidence of direct

propagation of second sound has been shown in solids at cryogenic temperatures but has never been experimentally verified at elevated temperatures. Our simulation results are confirmed by experimental measurements using a picosecond transient thermoreflectance system. Transient lattice cooling is observed in graphite for the first time and provides important insight on hydrodynamic transport in graphitic materials.

Chapter 6 presents our examination of phonon transport across an interface between silicon and germanium. We show that both the Landauer formula and its modified version fail for interfacial phonon transport due to their assumptions neglecting a strongly non-equilibrium distribution near the interface. This non-equilibrium distribution decays with distance from the interface and recovers to the bulk phonon distribution at the distance which we define as an effective interfacial region. We find that the internal phonon scattering within the interfacial region provides an important contribution to the overall interfacial resistance. Our study provides insights into large discrepancies between experimentally measured interfacial resistances and those calculated from the Landauer formula, which are often found in the literature, thus providing a useful way to interpret experimental data.

At last, Chapter 7 concludes the dissertation and discusses possible future directions for continued work.

2.0 Methodology

2.1 Full phonon scattering matrix from first principles

The first-principles based calculations have demonstrated great success in predicting phonon transport in various systems since been proposed more than ten years ago¹⁻³. The harmonic and anharmonic phonon properties are described by the second and third order force constants, respectively, which can be calculated from density functional theory. This method is well-known and documented in many previous studies, and here we briefly introduce the calculation process that leads to the full scattering matrix for three-phonon scattering.

The second and third order interatomic force constants are calculated by density functional theory using the Vienna Ab initio Simulation Package^{92,93} (VASP). The third order force constants, $\phi_{lmn}^{\alpha\beta\gamma}$, describe the anharmonic interaction among atoms l , m , and n in α , β , and γ directions, and are used to calculate the scattering matrix elements given by

$$V_{ijk}^{\pm} = \sum_{lmn} \sum_{\alpha\beta\gamma} \phi_{ijk}^{\alpha\beta\gamma} \frac{\mathbf{e}_{\mathbf{q},s}^{\alpha}(i) \mathbf{e}_{\pm\mathbf{q}',s'}^{\beta}(j) \mathbf{e}_{-\mathbf{q}'',s''}^{\gamma}(k)}{\sqrt{M_l M_m M_n}} \quad (2-1)$$

where M_i is the atomic mass for atom l , $e_{\mathbf{q},s}$ is the normalized eigenfunction for phonon state i with wavevector \mathbf{q} and polarization s . The sign \pm represents the coalescence process (+) or the decay process (-). The three-phonon scattering rate is then calculated as⁴

$$\Gamma_{ijk}^+ = \frac{\hbar\pi}{4} \frac{f_j^{\text{eq}} - f_k^{\text{eq}}}{\omega_i \omega_j \omega_k} |V_{ijk}^+|^2 \delta(\omega_i + \omega_j - \omega_k) \quad (2-2)$$

for coalescence process, and

$$\Gamma_{ijk}^- = \frac{\hbar\pi f_j^{\text{eq}} + f_k^{\text{eq}} + 1}{4 \omega_i \omega_j \omega_k} |V_{ijk}^-|^2 \delta(\omega_i - \omega_j - \omega_k) \quad (2-3)$$

for decay process. The δ function ensures energy conservation during the scattering event.

The phonon scattering rates are then formulated into the scattering matrix \mathbf{C} to be used in the PBE. The element C_{ij} describes the rate of phonon state j changing to phonon state i , and is calculated by summing up the scattering rates for all the scattering processes for phonon state i that involves phonon state j . The scattering element C_{ij} is written as

$$C_{ij} = \sum_k \left\{ \left[-\Gamma_{ijk}^+ \frac{f_i^{\text{eq}}(f_i^{\text{eq}} + 1)}{f_j^{\text{eq}}(f_j^{\text{eq}} + 1)} + \Gamma_{ijk}^+ \frac{f_i^{\text{eq}}(f_i^{\text{eq}} + 1)}{f_k^{\text{eq}}(f_k^{\text{eq}} + 1)} \right] + \frac{1}{2} \left[\Gamma_{ijk}^- \frac{f_i^{\text{eq}}(f_i^{\text{eq}} + 1)}{f_j^{\text{eq}}(f_j^{\text{eq}} + 1)} + \Gamma_{ijk}^- \frac{f_i^{\text{eq}}(f_i^{\text{eq}} + 1)}{f_k^{\text{eq}}(f_k^{\text{eq}} + 1)} \right] \right\}. \quad (2-4)$$

2.2 Deviational Peierls-Boltzmann Equation

2.2.1 Energy-based PBE

We solve the energy-based PBE instead of the regular PBE. The energy-based PBE can be obtained by multiplying phonon energy, $\hbar\omega$, on the both sides of the PBE with the full scattering matrix:

$$\frac{\partial e_i(\mathbf{r}, t)}{\partial t} + \mathbf{v}_i \cdot \nabla_{\mathbf{r}} e_i(\mathbf{r}, t) = \sum_j B_{ij} e_j(\mathbf{r}, t) \quad (2-5)$$

where e_i is the energy distribution function at state i defined as $\hbar\omega_i f_i$ and here ω_i is the phonon frequency. The matrix \mathbf{B} is the scattering operator in the energy-based PBE, with the element B_{ij}

defined as $C_{ij} \frac{\omega_i}{\omega_j}$. An advantage of solving the energy-based PBE is that the total energy is strictly conserved in the MC simulation which will be introduced later. If each sampling particle carries the same amount of energy, energy conservation can be strictly satisfied by simply conserving the total number of particles⁹⁴.

2.2.2 Deviation form of the PBE

As discussed in Section 1.4.2, the integral-differential equation is extremely difficult to solve. People have used the stochastic MC method to sample the phonon distribution function over reciprocal and real spaces successfully, but the variance of this stochastic method can be very large. When the deviation from equilibrium state is small, for example, with small temperature gradient in the sample, the variance can be even larger than the result. In this sense, we will lose the ability to solve such small deviation problems.

Here we use the deviational MC method^{88,94} to solve Eq. (2-5). While the typical MC method for solving the PBE samples distribution function⁹⁵⁻⁹⁷, the deviational MC method samples the deviation of distribution function from the already known equilibrium distribution^{88,94}. As the deviation of distribution is significantly small compared to the distribution, sampling the deviation has much reduced stochastic uncertainty compared to sampling the distribution function itself. The deviational PBE is developed from Eq. (2-5) and written as

$$\frac{\partial e_i^d(\mathbf{r}, t)}{\partial t} + \mathbf{v}_i \cdot \nabla_{\mathbf{r}} e_i^d(\mathbf{r}, t) = \sum_j B_{ij} e_j^d(\mathbf{r}, t) \quad (2-6)$$

Also, e^d is $e - e^0$ where e^0 is the Bose-Einstein energy distribution defined as $\hbar\omega f^0$.

2.3 Monte Carlo simulation

The deviational MC scheme will be used with phonon dispersion and scattering matrix that are calculated from *ab initio* lattice dynamics calculations. This does not require any fitting parameter and can fully capture the complex scattering mechanisms unlike Callaway's model. The algorithm of the deviational MC method is shown in Figure 4.

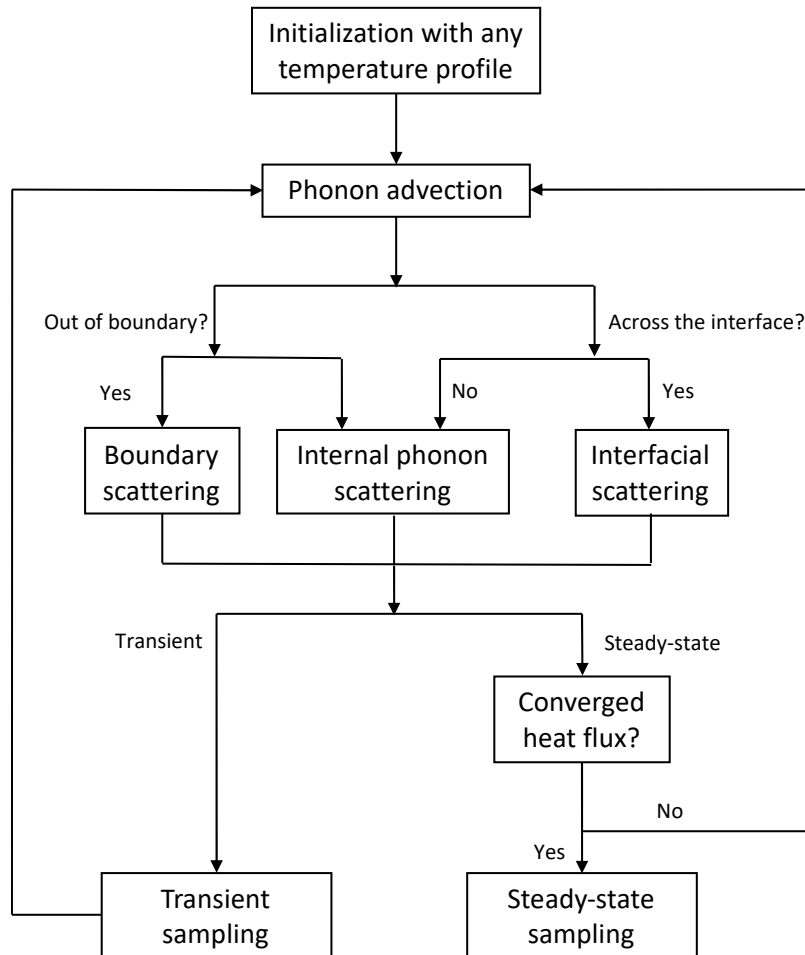


Figure 4 MC simulation flow.

The simulation particles are initialized in the sample based on initial conditions. At the beginning of each time step, the particles that already exist in the sample or newly generated from

boundaries are free to travel with their group velocities. This step is called advection. At the end of time step, the positions of the particles are updated, and internal phonon scattering will be applied. The particles will also experience boundary/interface scattering if their travel across the boundaries/interface. This advection-scattering step is repeated until the particle distribution is converged. Then the thermal properties will be sampled in small control volumes based on the number of particles and their phonon states.

2.3.1 Defining simulation particles

The number of phonons in an actual system is huge and beyond the capability of the simulation. To reduce the amount of computational cost, the simulation particle is a bundle of phonons that are at the same phonon state, as shown in Figure 4. Each simulation particle carries the same amount of energy despite the phonon state, which represents the energy that is deviated from the energy at equilibrium. The unit deviational energy that each particle carries $e_{\text{unit}}^{\text{d}}$ can be determined by the total energy in the system at equilibrium E_{tot} and an expected number of particles N_{part} which is an input parameter. For a system with length L , width W , and height H , contacting with a hot reservoir at T_{h} and a cold reservoir at T_{c} , the total deviational energy is

$$E_{\text{tot}} = \frac{1}{NV_{\text{uc}}} \sum_i \hbar\omega_i \frac{\partial f_i^{\text{eq}}}{\partial T} (T_{\text{h}} - T_{\text{c}}) LWH. \quad (2-7)$$

The number of particles N_{part} is usually on the order of millions. The deviational energy for each particle $e_{\text{unit}}^{\text{d}}$ is simply $E_{\text{tot}}/N_{\text{part}}$.

2.3.2 Initialization

The deviational MC simulation starts with generating phonon particles based on the initial temperature profile in the sample. For example, a linear temperature profile is a good initial guess for a heat flow driven by a constant temperature gradient. In this case, the local temperature T_0 at any control volume in the real space can be easily calculated. The number of phonon particles for the control volume is then

$$N_{CV,T_0} = \frac{1}{e_{\text{unit}}^d} \frac{1}{NV_{\text{uc}}} \sum_i \hbar\omega_i \frac{\partial f_i^{\text{eq}}}{\partial T} |T_0 - T_{\text{eq}}| V_{\text{CV}}. \quad (2-8)$$

Assuming that phonons follow the equilibrium Bose-Einstein distribution at T_0 , the phonon states of the particles can be determined by an accumulation function of $\hbar\omega_i \frac{\partial f_i^{\text{eq}}}{\partial T}$ through a MC algorithm described below:

- (1) For each new particle, generate a random number R .
- (2) Find the phonon state i that satisfy

$$\sum_{k=1}^{i-1} \hbar\omega_k \frac{\partial f_k^{\text{eq}}}{\partial T} \leq R < \sum_{k=1}^i \hbar\omega_k \frac{\partial f_k^{\text{eq}}}{\partial T} \quad (2-9)$$

where k loops over all the phonon states. The sign of unit energy that each particle carries will be determined by the local temperature in the control volume: if it is larger than the global equilibrium temperature, the particles carry positive energy, otherwise they carry negative energy. The particles with a positive energy contribute to the distribution larger than the equilibrium case, and those with a negative energy contribute to the distribution smaller than the equilibrium case.

It is worth mentioning that the initial temperature profile can be chosen arbitrarily depending on the system. The simulation would speed up if the initial condition is a good guess

for the steady-state condition. The initialization, however, is not mandatory for the simulation. The system can also start from an empty state and phonon particles will come from the boundaries.

2.3.3 Advection

At the beginning of each time step, the advection is applied for all particles in the system, including particles generated from boundaries (which will be discussed in section 2.3.4.2). This step corresponds to the left terms of Eq. (2-6),

$$\frac{\partial e_i^d(\mathbf{r}, t)}{\partial t} + \mathbf{v}_i \cdot \nabla_{\mathbf{r}} e_i^d(\mathbf{r}, t) = 0, \quad (2-10)$$

which describes the ballistic motion of phonon particles by updating the position of each particle at phonon state i during the time step Δt ,

$$\mathbf{r}_i(t + \Delta t) = \mathbf{r}_i(t) + \mathbf{v}_i \Delta t. \quad (2-11)$$

The new position of the particle will be used for calculating local thermal properties at the current time step $t + \Delta t$.

2.3.4 Phonon scattering

The scattering step is applied after the advection. The phonon particles experience internal phonon scattering due to anharmonicity, and boundary scattering when they come across the boundaries.

2.3.4.1 Internal phonon scattering

Internal phonon scattering is described by the scattering term on the right side of the deviational form of PBE with the full scattering matrix

$$\frac{\partial e_i^d(\mathbf{r}, t)}{\partial t} = \sum_j B_{ij} e_j^d(\mathbf{r}, t). \quad (2-12)$$

To implement the system of ordinary differential equations into a particle simulation with discretized time space, we follow the procedures proposed by Colin D. Landon⁹⁸. The change of phonon energy distribution during the given time interval is described with a matrix \mathbf{P} :

$$\mathbf{P}(\Delta t) = e^{\mathbf{B}\Delta t} = \sum_{k=0}^{\infty} \frac{\Delta t^k}{k!} \mathbf{B}^k. \quad (2-13)$$

The matrix \mathbf{P} is defined such that the phonon energy distribution in the future time step is related to the distribution in the current time step as

$$e_i^d(t + \Delta t) = \sum_j P_{ij}(\Delta t) e_j^d(t) \quad (2-14)$$

where \mathbf{r} of the distribution function is dismissed since internal scattering does not change the spatial position of phonons. Eq. (2-14) is not adequate to be simulated using a stochastic method because \mathbf{P} is a matrix with elements that can be negative or larger than unity. To describe the dynamics of transition between phonon states, we need to reform $P_{ij}(\Delta t)$ to scattering probabilities that range from 0 to 1. First, we note that because of energy conservation, we have

$$\sum_{i, P_{ij} \geq 0} P_{ij}(\Delta t) + \sum_{i, P_{ij} < 0} P_{ij}(\Delta t) = 1. \quad (2-15)$$

We then define column normalization parameters as

$$p_j^+ = \sum_{i, P_{ij} \geq 0} |P_{ij}(\Delta t)|, \quad (2-16)$$

$$p_j^- = \sum_{i, P_{ij} < 0} |P_{ij}(\Delta t)|, \quad (2-17)$$

$$p_j = \sum_i |P_{ij}(\Delta t)|. \quad (2-18)$$

It is trivial to find that

$$p_j^+ = 1 - \sum_{i, P_{ij} < 0} P_{ij}(\Delta t) = 1 + p_j^-, \quad (2-19)$$

$$p_j = p_j^+ + p_j^- = 1 + 2p_j^-. \quad (2-20)$$

Now Eq. (2-14) can be written as

$$e_i^d(t + \Delta t) = \sum_j \frac{P_{ij}(\Delta t)}{p_j} p_j e_j^d(t). \quad (2-21)$$

The first term in the summation $P_{ij}(\Delta t)/p_j$ describes the change from phonon state j to i with the probability of $|P_{ij}(\Delta t)|/p_j$. If $P_{ij}(\Delta t) < 0$, it comes with a sign change. For the second term p_j , we apply Eq. (2-20) and use the same expansion on p_j^- :

$$\begin{aligned} e_i^d(t + \Delta t) &= \sum_j \frac{P_{ij}(\Delta t)}{p_j} (1 + 2p_j^-) e_j^d(t) \\ &= \sum_j \frac{P_{ij}(\Delta t)}{p_j} \left(1 + \frac{2p_j^-}{p_j} p_j \right) e_j^d(t) \\ &= \sum_j \frac{P_{ij}(\Delta t)}{p_j} \left(1 + \frac{2p_j^-}{p_j} (1 + 2p_j^-) \right) e_j^d(t) \\ &= \sum_j \frac{P_{ij}(\Delta t)}{p_j} \left(1 + \frac{2p_j^-}{p_j} + \left(\frac{2p_j^-}{p_j} \right)^2 p_j \right) e_j^d(t) \\ &= \dots \end{aligned} \quad (2-22)$$

and so on. Finally, we come to a power series

$$e_i^d(t + \Delta t) = \sum_j \text{sgn}[P_{ij}(\Delta t)] \frac{|P_{ij}(\Delta t)|}{p_j} \left[1 + \sum_{n=1}^{\infty} \left(\frac{p_j^-}{p_j} \right)^n 2^n \right] e_j^d(t) \quad (2-23)$$

where sgn is a sign function.

The power series can be stochastically simulated by implementing the following algorithm:

For a sampling particle in phonon state j ,

(1) Generate a random number R .

(2) Find the phonon state i satisfying

$$\sum_{k=1}^{i-1} \frac{|P_{kj}|}{p_j} \leq R < \sum_{k=1}^i \frac{|P_{kj}|}{p_j}. \quad (2-24)$$

The phonon state i can be found with a probability of $|P_{ij}(\Delta t)|/p_j$. Then, change the particle state from j to i , and change the sign of energy the particle carries according to $\text{sgn}[P_{ij}(\Delta t)]$.

(3) If $\text{sgn}[P_{ij}(\Delta t)]$ is negative in the step (2), which occurs with a probability of p_j^-/p_j , we simulate the term with the first order in p_j^-/p_j in Eq. (2-23). In this case, we simply generate two sampling particles in state j . The steps from (1) to (3) are applied for these two particles. The terms with second and higher order in p_j^-/p_j in Eq. (2-23) can be recursively simulated during this process.

2.3.4.2 Boundary scattering

The boundary scattering is also applied if phonon particles travel out of the real space domain. Different boundary conditions are implemented in the simulation corresponding to various situations in experiments.

2.3.4.2.1 Periodic heat flux

When a sample is large enough and the boundaries can be neglected, the transport is essentially a one-dimensional problem. For an infinitely large sample, phonon distribution is

spatially uniform. A periodic boundary condition of heat flux^{94,97} is used in the heat transport direction. For other two directions, fully specular reflections are applied for each particle representing infinitely long sample in these directions.

A single control volume is used for the real space sampling, with two boundaries in the heat transport direction assigned with different temperatures T_h and T_c . The temperature difference is the driving force for the system and a source for new phonon particles. Phonon particles come out of the boundaries at assigned temperatures with the time step dt . The number of new phonon particles is calculated by

$$N_{\text{source}} = \frac{1}{e_{\text{unit}}^d} \frac{1}{NV_{\text{uc}}} \sum_i \hbar\omega_i \frac{\partial f_i^{\text{eq}}}{\partial T} (T_h - T_c) |v_{i,x}| \Delta t W \quad (2-25)$$

where W is the sample width. These new particles will have random positions, and the phonon state for each particle will be determined in the same procedure as described in Section 2.3.2. For a particle with positive velocity in the heat transport direction, the sign of energy it carries will be positive; otherwise, it will be negative. This ensures energy conservation with no extra energy added to the system, while maintaining the expected heat flux. The newly generated particles will then travel along with other existing particles.

At the boundaries with periodic heat flux condition, the deviation of the phonon distribution from local equilibrium is periodic. This is achieved by, besides generating new particles from boundaries, moving periodically the existing particles⁹⁴. When phonon particles hit the periodic boundaries within a time step, the position on the boundary will be recorded and the remaining time will be calculated. Then they will reenter the system through the boundary on the other side at the same position and travel for the remaining time.

2.3.4.2.2 Isothermal

Isothermal boundaries are used for a system attached with heat reservoirs at fixed temperatures T_h and T_c . When a particle hits the isothermal boundaries, it is absorbed by the boundaries and discarded in the simulation. The boundaries also constantly emit phonon particles following the equilibrium Bose-Einstein distribution at the wall temperature. For a hot reservoir at temperature T_h higher than the reference temperature T_{eq} , the number of particles generated is

$$N_{\text{wall,hot}} = \frac{1}{e_{\text{unit}}^d} \frac{1}{NV_{\text{uc}}} \sum_{i, v_i \hat{n}_{\text{wall}} > 0} \hbar \omega_i \frac{\partial f_i^{\text{eq}}}{\partial T} (T_h - T_{\text{eq}}) v_i \hat{n}_{\text{wall}} \Delta t W \quad (2-26)$$

where \hat{n}_{wall} is the inward normal vector for the wall and $v_i \hat{n}_{\text{wall}} > 0$ ensures the generated particle is coming into the sample. Similarly, for a cold reservoir at temperature T_c lower than the reference temperature T_{eq} , the number of particles generated is

$$N_{\text{wall,cold}} = \frac{1}{e_{\text{unit}}^d} \frac{1}{NV_{\text{uc}}} \sum_{i, v_i \hat{n}_{\text{wall}} > 0} \hbar \omega_i \frac{\partial f_i^{\text{eq}}}{\partial T} (T_{\text{eq}} - T_c) v_i \hat{n}_{\text{wall}} \Delta t W. \quad (2-27)$$

The phonon state of each particle will be determined in the same procedure as described in Section 2.3.2, but with an accumulation function of $\hbar \omega_i \frac{\partial f_i^{\text{eq}}}{\partial T} v_i \hat{n}_{\text{wall}}$. The particles will be randomly placed on the boundaries and then travel into the sample in the next time step.

2.3.4.2.3 Adiabatic

Adiabatic boundaries reflect all the incident phonon particles, not allowing energy transfer across the boundaries. The boundary reflection can be fully specular, fully diffuse, and partially specular, depending on the situation.

Specular reflection represents an infinitely long sample in that direction or a perfectly smooth boundary. When a phonon particle hit the boundary, its phonon state will be changed from state i to state j which satisfy

$$v_i \hat{n}_{\text{wall}} = -v_j \hat{n}_{\text{wall}} \quad (2-28)$$

with all other phonon properties between i and j remain the same.

For fully diffuse scattering, an incident particle is reflected by the boundary with the traveling direction randomized. The boundaries absorb all incident particles and emit the same number of particles with random velocities. Specifically, the diffuse boundary is divided into many subsegments. During each time step, the number of particles that hit each subsegment of the boundary is recorded. At the beginning of next time step, each subsegment will emit the same number of particles randomly sitting on the boundary. Their phonon states will be determined through the same procedure as described in Section 2.3.2, with their traveling directions pointing into the sample.

A partially specular reflecting boundary is the combination of specular and diffuse boundaries. For a boundary with roughness, phonon particles with different wavelengths will experience the boundary scattering differently. A rough edge of the boundary is likely to scatter small/large wavelength phonons diffusely/specularly. Whether a specific phonon mode will experience diffuse or specular boundary scattering is determined by Ziman's formula^{99,100}

$$p(\lambda) = \exp\left(-\frac{16\pi^2\eta^2}{\lambda^2}\right) \quad (2-29)$$

where λ is phonon wavelength, η is boundary roughness, and the specularity p suggests diffuse ($p = 0$) or specular ($p = 1$) boundary scattering.

It is worth pointing out here that the boundary condition, whether specular or diffuse reflection, can have a significant effect on the overall phonon transport. We would like to prove

here that fully diffuse boundary scattering is valid for thermal transport in suspended graphene. For the roughness of graphene, previous experimental study¹⁰¹ has shown that the cleaved edges of mechanically exfoliated single-layer graphene exhibit a roughness of 3 nm. With this roughness, we plot the specularity with phonon wavelength in Figure 5. It is shown that all the phonon modes in our study will experience fully diffuse boundary scattering.

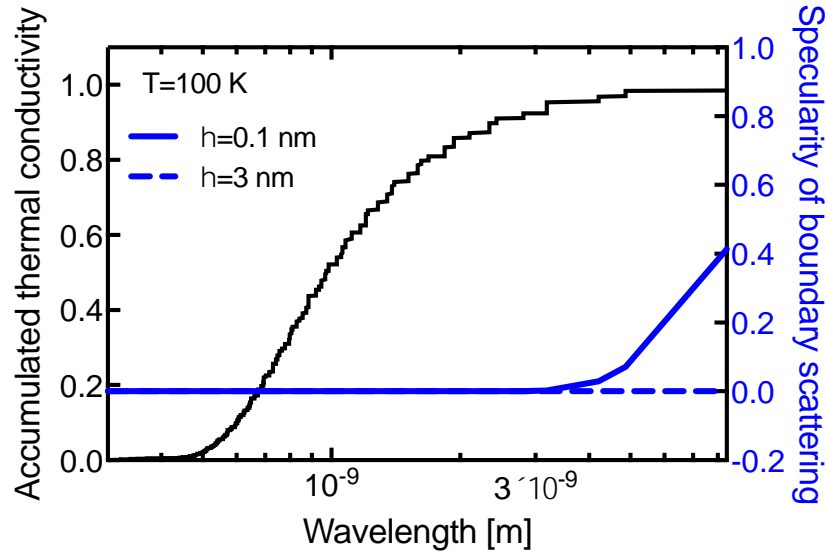


Figure 5 Accumulated thermal conductivity (left y-axis) and specularity of boundary scattering (right y-axis) as a function of phonon wavelength. The boundary scattering for phonons that carry most of the heat is diffuse, even with a very smooth edge (roughness of 0.1 nm).

Now even if we change the roughness to 0.1 nm, assuming an ideal case with almost perfect edges, we see that for phonons with wavelengths smaller than 3 nm, fully diffuse boundary scattering is completely correct. To study the effect of this boundary roughness on thermal transport, we calculate the accumulated thermal conductivity with respect to phonon wavelength, as shown in Figure 5. It is clear that phonons with wavelengths less than 3 nm carry almost all the heat. This shows that fully diffuse boundary scattering is a reasonable assumption for suspended graphene, which will be used in Chapter 3 and 4.

2.3.5 Cancellation of particles

At every time step in the simulation, new phonon particles will be generated from the temperature gradient, the boundaries, and internal phonon scattering. Even though some existing particles will hit the isothermal boundaries and be discarded, it cannot balance out the number of generated particles, and the total number of particles in the simulation will continue to grow and go beyond the limit imposed by available memory. The growth of number of particles is controlled by a cancellation step. The cancellation of particles is based on the idea that two phonon particles with the same phonon state, same spatial position, but opposite sign of energy, will have the exactly opposite contribution to heat flow. Thus, these two phonon particles can be both discarded without affecting the phonon transport. In this way the total number of particles can be largely reduced, and the system will be stable.

The cancellation is performed at the end of each time step, before the sampling of thermal properties. First, the number of particles in every spatial control volume, at every phonon state, and for positive and negative signs of energy, will be counted and recorded. Two phonon particles that have opposite sign of energy, but the same other attributes, will form a pair. Then pairs of particles will be randomly chosen and deleted. It should be noted that the cancellation of particles diminishes the difference of spatial phonon distribution within the control volume, so the size of control volume should be similar to the average phonon mean free path to avoid losing local information of phonon distribution. Also, the cancellation is time consuming and will slow down the simulation, so the frequency of this step should be adjusted considering both the stability and speed of the simulation.

2.3.6 Sampling of thermal properties

The spatial dependent thermal properties in phonon transport are calculated based on phonon distribution in control volumes in the space domain. In our deviational scheme for particle transport, the deviational temperature in a control volume is

$$T_d = \frac{1}{V_{CV}C_v} \sum_{i=1}^{N_{pp}} \text{sgn}(E_i) e_{\text{unit}}^d \quad (2-30)$$

where V_{CV} is the volume of the control volume, N_{pp} is the number of phonon particles in the control volume, and $\text{sgn}(E_i)$ is the sign of energy that a particle carries. Similarly, the heat flux along x direction in the control volume is

$$q_x = \frac{1}{V_{CV}} \sum_{i=1}^{N_{pp}} \text{sgn}(E_i) e_{\text{unit}}^d v_{i,x}. \quad (2-31)$$

Note that the sampling can be performed at every time step so that transient phenomena are captured, or over multiple time steps for steady-state sampling.

2.3.7 Validations

The proposed deviational MC method for solving the PBE has been validated against analytic solution of the PBE with the assumption of single mode relaxation time^{88,94}. The validation from the previous studies includes the transient 1D ballistic phonon transport and steady-state phonon transport in thin films. We use the same algorithm except for the scattering process as we employ a full scattering matrix.

2.3.7.1 Infinitely large graphene at steady-state

In order to validate our MC method employing a full scattering matrix, we calculate thermal conductivity in an infinitely large sample using MC method (κ_{MC}) and compare the thermal conductivity value to the thermal conductivity obtained from the full-iterative method ($\kappa_{iterative}$). The full-iterative method has been widely used to study high thermal conductivity materials in recent studies^{1-4,102-104}. In Figure 6, we show the schematic of computational domain, which represents the infinitely large sample. In Figure 7, we compare κ_{MC} and $\kappa_{iterative}$ in a wide range of temperature. As can be seen, κ_{MC} is identical to $\kappa_{iterative}$, validating the MC algorithm of scattering with a full scattering matrix.

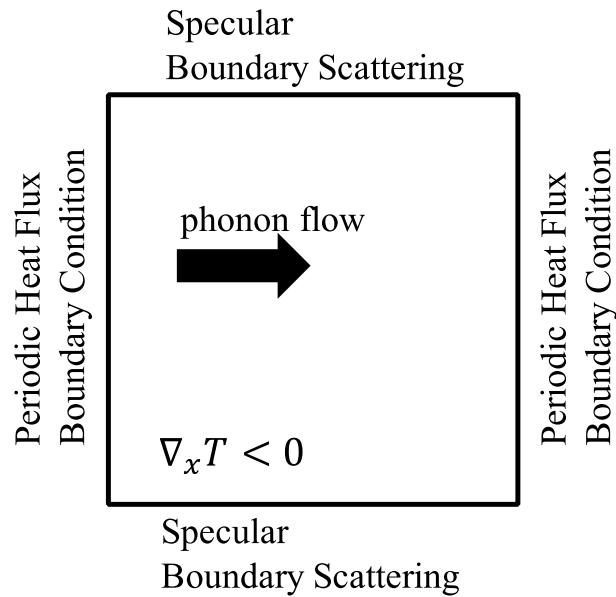


Figure 6 Schematic of computational domain representing an infinitely large sample. Reproduced with permission from [16]. Copyright 2019 American Physical Society.

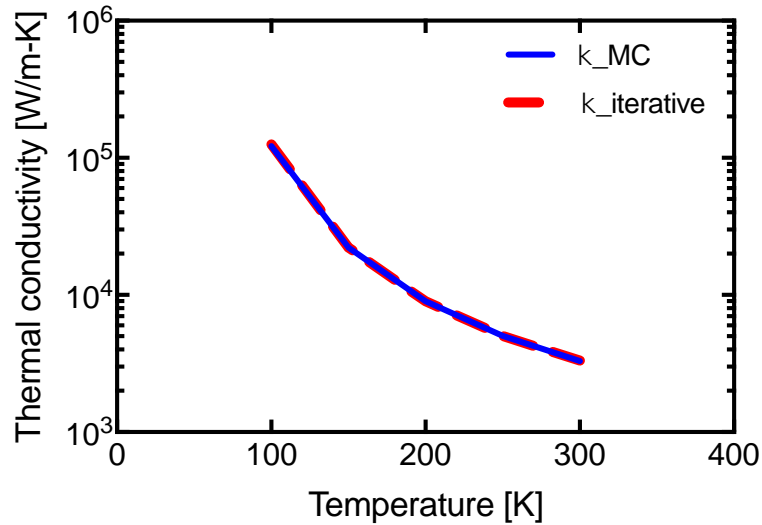


Figure 7 Thermal conductivity for an infinitely large graphene at different temperatures calculated from MC simulation and iterative solution. The error bars for MC results are smaller than the width of line. Reproduced with permission from [16]. Copyright 2019 American Physical Society.

2.3.8 Phonon transport across an interface

The MC method is also used to simulate phonon transport between different materials with the knowledge of phonon transmissivity across the interface. The MC algorithm for interfacial phonon transport is similar to that for phonon transport in bulk materials, with a few changes at the interface and boundaries. Firstly, phonons scattered by the interface will change the phonon state that is described by the DMM. Secondly, for simulating semi-infinite system on each side of the interface, the periodic heat flux boundary condition discussed in section 2.3.4.2.1 cannot be implemented because phonons in one material cannot directly enter into the other material. To simulate infinitely large system, phonons generated at the boundaries will follow the bulk phonon distribution rather than the local equilibrium distribution, and the temperature gradient needed for the bulk distribution is determined through a self-consistent algorithm.

2.3.8.1 Scattering at the interface

In the MC simulation, when phonons hit the interface during their advection, they will be scattered by the interface. The interfacial scattering could allow the phonon to transmit across the interface, or be reflected back, depending on the transmissivity. The transmissivity is a function of phonon frequency and calculated through the DMM as shown in Eq. (1-14). Since the DMM assumes elastic scattering, the frequency of the transmitting phonon should not be changed. However, due to the fact that the harmonic properties of phonons and the discretization of reciprocal space in two different materials are not necessarily the same, a certain phonon frequency may not exist in both materials. Thus, instead of using a δ function as in Eq. (1-14) to ensure energy conservation at each frequency, the frequency domain is discretized into many frequency bins for each material in the MC simulation. In addition, a Gaussian function is used to eliminate the large difference between frequency bins. The Gaussian function is

$$G(|\omega_i - \omega_0|, \sigma) = \frac{1}{\sqrt{2\pi}\sigma} \exp\left(-\frac{|\omega_i - \omega_0|^2}{2\sigma^2}\right) \quad (2-32)$$

where ω_0 is the maximum frequency for each frequency bin, and σ is a broadening factor. The frequencies for phonons before and after interfacial scattering may not be exactly the same, but they will be most likely be in the same frequency bin as described by the Gaussian function. To determine the proper value of σ , we calculate the transmissivity from Si to Ge with different σ , as shown in Figure 8. The $d\omega$ is the size of frequency bin, and Figure 8(a) shows the transmissivity when energy conservation is enforced within frequency bins without the Gaussian broadening. A value of $2d\omega$ for σ is chosen such that the transmissivity is a smooth function of frequency and also contains local details when σ is small.

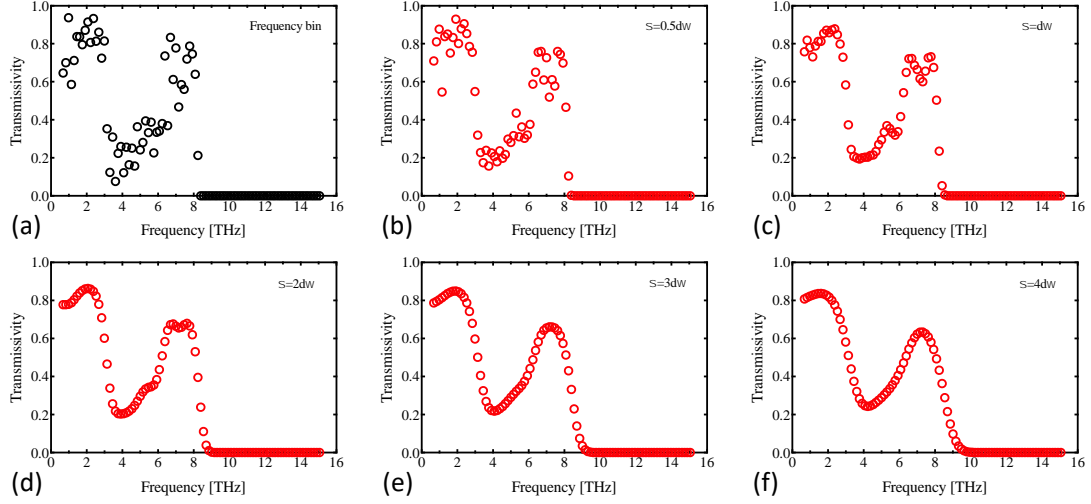


Figure 8 Transmissivity from Si to Ge with different broadening factor in the Gaussian function.

With the Gaussian function, the detailed balance in Eq. (1-13) is modified as

$$\begin{aligned}
 t_{12}(\omega) & \frac{1}{N_1 V_1} \sum_i \hbar \omega_i f_i^{\text{eq}} |v_{i,x}| G(|\omega_i - \omega_0|, \sigma) \\
 & = t_{21}(\omega) \frac{1}{N_2 V_2} \sum_j \hbar \omega_j f_j^{\text{eq}} |v_{j,x}| G(|\omega_j - \omega_0|, \sigma)
 \end{aligned} \tag{2-33}$$

for energy conservation in MC simulation with coarse mesh in the reciprocal space. The spectral transmissivity for each frequency bin with maximum frequency ω_0 is then

$$\begin{aligned}
 & t_{12}(\omega_0) \\
 & = \frac{\frac{1}{N_2 V_2} \sum_j \hbar \omega_j f_j^{\text{BE}} |v_{x,j}| G(|\omega_j - \omega_0|, \sigma)}{\frac{1}{N_1 V_1} \sum_i \hbar \omega_i f_i^{\text{BE}} |v_{x,i}| G(|\omega_i - \omega_0|, \sigma) + \frac{1}{N_2 V_2} \sum_j \hbar \omega_j f_j^{\text{BE}} |v_{x,j}| G(|\omega_j - \omega_0|, \sigma)}.
 \end{aligned} \tag{2-34}$$

Although the energy conservation may not be satisfied for a single event of interfacial scattering, for a large number of phonons the total energy is well conserved. The algorithm for interfacial scattering is further explained below.

When a phonon hits the interface, a random number R will be generated and compared to the phonon's transmissivity t . If R is less than or equal to t , the phonon will transmit across the interface and join the other material; otherwise, it will be reflected back into the same material. After interfacial scattering, the phonon state will be randomly determined due to the fact that phonons are scattered diffusely. To determine the new phonon state of the scattered phonon, we firstly count all the phonon states that satisfy two requirements: 1) the phonon state should be in the same material as the scattered phonon if it is reflected, and in the other material if the scattered phonon is transmitted, and 2) the phonon state should have the same/opposite sign of velocity in the heat transport direction as the scattered phonon if it is transmitted/reflected. A summation of absolute value of modal heat flux with the Gaussian function for all available states will be calculated as

$$Q_{\text{total}} = \sum_i \hbar\omega_i f_i^{\text{BE}} |v_{i,x}| G(|\omega_i - \omega_0|, \sigma) \quad (2-35)$$

where ω_0 is the maximum frequency of the frequency bin that the incoming phonon lies in, and $v_{i,x}$ is the velocity for state i with the correct sign. Then a random number R will be generated, and the scattered phonon will be assigned the phonon state i satisfying

$$\sum_{k=1}^{i-1} \frac{\hbar\omega_k f_k^{\text{BE}} |v_{k,x}| G(|\omega_k - \omega_0|, \sigma)}{Q_{\text{total}}} < R \leq \sum_{k=1}^i \frac{\hbar\omega_k f_k^{\text{BE}} |v_{k,x}| G(|\omega_k - \omega_0|, \sigma)}{Q_{\text{total}}}. \quad (2-36)$$

The time that the scattered phonon spent to hit the interface will also be accounted, and the phonon continues to travel for the remaining time after the scattering process.

2.3.8.2 Bulk phonon distribution at the boundaries

To simulate semi-infinite materials on both sides of the interface, the temperature inside each boundary will vary and follow the same temperature gradient as in the material, rather than

being constant as in the isothermal boundary. This means that the boundaries are virtual extensions of the system. When phonons hit the boundaries, they will be absorbed in the same way as hitting isothermal boundaries. The boundaries also emit phonons into the system with the bulk distribution, not the local equilibrium Bose-Einstein distribution. The bulk distribution for heat transport along x direction can be calculated from an iterative solution⁴ of Eq. (1-20) as

$$f_{i,\text{bulk}} = f_i^0 - \mathbf{F}_{x,i} \frac{\partial f_i^0}{\partial T} \frac{dT}{dx} \quad (2-37)$$

where \mathbf{F} represents the deviation from equilibrium with the dimension of length. The number of phonon particles coming out from the hot and cold boundary during the timestep is then calculated as

$$N_{\text{wall,hot,bulk}} = \frac{1}{e_{\text{unit}}^d} \frac{1}{N_1 V_{\text{uc}1}} \sum_{i,v_i \hat{n}_{\text{wall}} > 0} \hbar \omega_i \frac{\partial f_i^{\text{eq}}}{\partial T} \left[(T_{\text{h}} - T_{\text{eq}}) + \left(-\frac{dT}{dx} \right)_1 (\mathbf{F}_{x,i} + v_{i,x} \Delta t) \right] v_i \hat{n}_{\text{wall}} \Delta t W, \quad (2-38)$$

$$N_{\text{wall,cold,bulk}} = \frac{1}{e_{\text{unit}}^d} \frac{1}{N_2 V_{\text{uc}2}} \sum_{i,v_i \hat{n}_{\text{wall}} > 0} \hbar \omega_i \frac{\partial f_i^{\text{eq}}}{\partial T} \left[(T_{\text{eq}} - T_{\text{c}}) + \left(-\frac{dT}{dx} \right)_2 (\mathbf{F}_{x,i} + v_{i,x} \Delta t) \right] v_i \hat{n}_{\text{wall}} \Delta t W \quad (2-39)$$

where subscript 1 and 2 represents material 1 and material 2, respectively. The state for each phonon particle coming out of the boundary is determined as the same procedure in Section 2.3.2, but with an accumulation function of

$$\hbar \omega_i \frac{\partial f_i^{\text{eq}}}{\partial T} |v_{x_i}| \left| T_{\text{h}} - T_{\text{eq}} + \left(-\frac{dT}{dx} \right)_1 (\mathbf{F}_{x,i} + v_{x_i} \Delta t) \right| \quad (2-40)$$

for hot boundary with material 1, and

$$\hbar\omega_i \frac{\partial f_i^{\text{eq}}}{\partial T} |v_{x_i}| \left| T_{\text{eq}} - T_c + \left(-\frac{dT}{dx} \right)_2 (\mathbf{F}_{x,i} + v_{x_i} \Delta t) \right| \quad (2-41)$$

for cold boundary with material 2.

2.3.8.3 Self-consistent algorithm

To calculate the accumulation function in Eqs. (2-40) and (2-41), the temperature gradient in each material should be known. For semi-infinite materials, the thermal conductivity should recover to bulk value because the effect of the interface is negligible, and the temperature gradient can be calculated with the heat flux in the system. However, the heat flux is unknown prior to the MC simulation. Assuming an initial temperature gradient for the boundaries to start the simulation, the temperature gradient in the system may be different after the simulation. Thus, an iteration for a self-consistent result is needed to obtain the converged heat flux and temperature gradient.

To start with, the temperature gradient in one of the boundaries, for example, the cold boundary, is set to be $(T_h - T_c)/L$ where L is the total length of the system, then the temperature gradient in the hot boundary can be determined by Fourier's law knowing that the thermal conductivities in two materials are bulk values and that the heat flux is a constant. The heat flux in the boundaries (reservoirs) is then obtained as

$$q_{\text{res}} = \kappa_1 \left(-\frac{dT}{dx} \right)_{1,b} = \kappa_2 \left(-\frac{dT}{dx} \right)_{2,b} \quad (2-42)$$

and denoted as q_{res} . The subscript b means the temperature gradient in the boundary. The system (device) will start with the heat flux of q_{res} but then reach steady state with a heat flux q_{dev} . If the system is small and quasi-ballistic effect is strong, q_{dev} will be much different from q_{res} , otherwise, if the system is large enough to fully recover to diffusive phonon transport at the boundary, q_{dev} will be similar to q_{res} . After the first iteration is finished, q_{res} will be set to q_{dev} ,

and the temperature gradient at each boundary will be recalculated under the new q_{res} , and the MC simulation will start again with the new boundary conditions. A factor s will then be calculated as $q_{\text{dev}}/q_{\text{res}}$ and compared to unity. If $|s - 1| \leq 5\%$, then the simulation is considered converged, and the heat flux and temperature imposed in the reservoirs are consistent.

3.0 Role of hydrodynamic viscosity on phonon transport in suspended graphene

When phonon transport is in the hydrodynamic regime, the thermal conductivity exhibits peculiar dependences on temperatures (T) and sample widths (W). These features were used in the past to experimentally confirm the hydrodynamic phonon transport in three-dimensional bulk materials. Suspended graphene was recently predicted to exhibit strong hydrodynamic features in thermal transport at much higher temperature than the three-dimensional bulk materials, but its experimental confirmation requires quantitative guidance by theory and simulation. Here we quantitatively predict those peculiar dependences using the MC solution of the PBE with an *ab initio* full three-phonon scattering matrix. Thermal conductivity is found to increase as T^α where α ranges from 1.89 to 2.49 depending on a sample width at low temperatures, much larger than 1.68 of the ballistic case. The thermal conductivity has a width dependence of $W^{1.17}$ at 100 K, clearly distinguished from the sublinear dependence of the ballistic-diffusive regime. These peculiar features are explained with a phonon viscous damping effect of the hydrodynamic regime. We derive an expression for the phonon hydrodynamic viscosity from the PBE, and discuss that the phonon viscous damping explains well those peculiar dependences of thermal conductivity at 100 K. The phonon viscous damping still causes significant thermal resistance when a temperature is 300 K and a sample width is around 1 μm , even though the hydrodynamic regime is not dominant over other regimes at this condition.

3.1 Background

Graphene has extremely high thermal conductivity and thus has a great potential for thermal management applications. Past experimental studies^{11,12} show that the thermal conductivity is around 4000 W/m-K (up to 5300 W/m-K) at room temperature for suspended graphene, and can still be as high as 600 W/m-K when graphene is supported by a substrate. This high thermal conductivity is explained by graphene's large Debye temperature resulted from the small atomic mass of carbon and strong carbon-carbon bonding³. The high Debye temperature leads to large group velocity of acoustic phonon modes. In addition, phonons are predominantly populated near the center of the first Brillouin zone, leading to weak U-scattering. Both features together can cause strong N-scattering and its rate is larger than that of U-scattering by at least one order of magnitude¹⁰². The hydrodynamic regime is thus considered another important regime of phonon transport in suspended graphene^{13,14}.

As discussed in section 1.2.2.2, phonon Poiseuille flow is a peculiar phenomenon in hydrodynamic regime. A noteworthy difference between the phonon Poiseuille flow and the common diffusive phonon flow governed by the Fourier's law is the mechanism of thermal resistance. While U-scattering directly cause thermal resistance in the diffusive flow, the thermal resistance in the phonon Poiseuille flow is due to viscous effects. The viscous effects occur when the drift velocity has a spatial gradient due to boundaries. In the Poiseuille flow, phonons exhibit a maximum drift velocity at the center of a sample and a minimum drift velocity at the boundaries due to diffuse boundary scattering. With the spatial gradient of drift velocity from the center to the boundaries, the momentum of phonons is transferred through many N-scattering processes and finally destroyed by the diffuse boundary scattering, leading to thermal resistance.

The phonon Poiseuille flow has been theoretically studied^{19,24} and experimentally confirmed by observing a peculiar temperature dependence of thermal conductivity that increases faster than ballistic case²⁰. For example, thermal conductivity of solid He was observed to follow T^8 trend while the thermal conductivity of ballistic limit should follow T^3 . For suspended graphene, it has not been discovered yet if graphene exhibits a temperature dependence of thermal conductivity that is significantly different from ballistic case so that the Poiseuille flow can be clearly observed in experiment. Here, we quantitatively discuss the details of the phonon Poiseuille flow in suspended graphene by solving the PBE with a full scattering matrix from first-principles.

3.2 Failure of homogeneous boundary scattering

The homogenous approximation eliminates the differentiation in the advection term. It is valid when the sample size is infinitely large or the spatial variation of the distribution function due to the diffuse boundary scattering is small enough to be ignored. In order to include the reduction of thermal conductivity due to the classical size effect, the boundary scattering rate is often calculated with a simple relation^{102,105}:

$$\tau_B^{-1} = \frac{2v_y}{W} \quad (3-1)$$

where v_y is the group velocity of phonon in the normal direction to the boundary. Then, the calculated boundary scattering rate is added to the diagonal terms of the scattering matrix. Although the homogenous boundary scattering model can qualitatively predict the decreasing thermal conductivity as a sample size decreases, its assumption is not valid when phonon distribution significantly varies in space. In the phonon Poiseuille flow, we expect that the

distribution function along the normal direction to the temperature gradient is significant. This is because U-scattering, which provides spatially uniform momentum sink and thus causes uniform distribution function, is weaker than diffuse boundary scattering. Therefore, the homogenous approximation cannot be used for the hydrodynamic regime.

3.3 Phonon hydrodynamic viscosity from momentum balance equation

The momentum transfer through N-scattering to the boundaries combined with the diffuse boundary scattering, i.e., viscous damping effect, is the major source of thermal resistance in the hydrodynamic regime. Therefore, it would be interesting to define the phonon hydrodynamic viscosity which represents the rate of momentum transfer at a given drift velocity gradient. Here we derive the expression for the phonon hydrodynamic viscosity and the momentum balance equation from the PBE with Callaway's scattering model. We assume that the MFP of N-scattering is much smaller than the characteristic sample size. The displaced Bose-Einstein distribution with the deviation from global temperature ΔT is

$$f_i^{\text{disp}} = \frac{1}{\exp\left[\frac{\hbar(\omega_i - q_{i,x} \cdot u_x)}{k_B(T + \Delta T)}\right] - 1} \quad (3-2)$$

and can be linearized as

$$f_i^{\text{disp}} = f_i^{\text{eq}} + \frac{\hbar\omega_i}{k_B T} T' f_i^{\text{eq}} (f_i^{\text{eq}} + 1) + \frac{\hbar}{k_B T} f_i^{\text{eq}} (f_i^{\text{eq}} + 1) q_{i,x} \cdot u_x \quad (3-3)$$

by assuming $q_{i,x} \cdot u_x \ll \omega_i$, and $T' = \Delta T/T \ll 1$ where T' is the ratio of temperature difference to the equilibrium temperature. The momentum balance equation can be derived by multiplying

q_x on the both sides of the PBE with Callaway's scattering model, as in Eq. (1-22), and integrate over the first Brillouin zone. The resulting equation is:

$$\sum_i q_{i,x} v_{i,x} \frac{df_i}{dx} + \sum_i q_{i,x} v_{i,y} \frac{df_i}{dy} = \sum_i -q_{i,x} \frac{f_i - f_i^0}{\tau_{i,U}}. \quad (3-4)$$

The first and second terms on the left side represent the flux along x and y directions, respectively, of x direction momentum in a two-dimensional material. Note that the momentum change due to scattering in the right-hand side includes only U-scattering because N-scattering conserves total momentum.

The distribution function f_i can be found by solving Eq. (1-22) with the following approximation:

$$\nabla_{\mathbf{r}} f_i \approx \nabla_{\mathbf{r}} f_i^{\text{disp}}, \quad (3-5)$$

which corresponds to the first order in Chapman-Enskog expansion of gas kinetics theory¹⁰⁶ and is also called the mean free time approximation. This approximation is valid if the phonon MFP is much smaller than the characteristic length of a sample. Applying the mean free time approximation to Eq. (1-22) gives

$$\mathbf{v}_i \cdot \nabla_{\mathbf{r}} f_i^{\text{disp}} = -\frac{f_i - f_i^{\text{disp}}}{\tau_{i,N}} - \frac{f_i - f_i^0}{\tau_{i,U}}. \quad (3-6)$$

Inserting the solution of Eq. (3-6) into Eq. (3-4) and assuming the fully developed flow case $du_x/dx = 0$ gives

$$\frac{dT'}{dx} = \mu_{\text{ph}} \frac{\partial^2 u_x}{\partial y^2} - \beta u_x \quad (3-7)$$

where

$$\mu_{\text{ph}} = \frac{\sum_i q_{i,x}^2 v_{i,y}^2 f_i^{\text{eq}} (f_i^{\text{eq}} + 1) \tau_{i,N}}{\sum_i q_{i,x} v_{i,x} f_i^{\text{eq}} (f_i^{\text{eq}} + 1) \omega_i}, \quad (3-8)$$

$$\beta = \frac{\sum_i q_{i,x}^2 f_i^{\text{eq}} (f_i^{\text{eq}} + 1) \tau_{i,U}^{-1}}{\sum_i q_{i,x} v_{i,x} f_i^{\text{eq}} (f_i^{\text{eq}} + 1) \omega_i}. \quad (3-9)$$

Here we assume $\tau_{i,N}^{-1} \gg \tau_{i,U}^{-1}$. Equation (3-7) can be understood as a momentum balance of phonon system: the phonon system gains net momentum from the temperature gradient in the left-hand side and the gained momentum is either spatially distributed by the viscous effect represented by phonon viscosity (μ_{ph}) or destroyed by U-scattering represented by β . A similar equation was provided elsewhere¹³ without derivation. Note that the momentum balance equation in the previous work¹³ includes $|\mathbf{v}|^2$ in the viscosity, but it should be corrected to v_y^2 . The thermal conductivity can then be calculated by solving Eq. (3-7) with an assumption of zero drift velocity at the boundary so called no-slip boundary condition and the assumption of negligible U-scattering¹³:

$$\kappa_{\text{drift}} = \frac{\hbar^2}{k_B N V} \frac{\sum_i \omega_i q_{i,x} v_{i,x} f_i^{\text{eq}} (f_i^{\text{eq}} + 1)}{\mu_{\text{ph}} T^2} W^2. \quad (3-10)$$

3.4 Characteristics of phonon Poiseuille flow

3.4.1 Temperature dependence of thermal conductivity

The temperature dependence of thermal conductivity is different for all three regimes of phonon transport. The thermal conductivity in the diffusive regime decreases with temperature due to the increased rates of U-scattering. In the ballistic regime, thermal conductivity follows the trend of the ballistic thermal conductance, $C_v v$, where C_v is the volumetric specific heat and v is the phonon group velocity. The ballistic thermal conductance of three-dimensional Debye crystal increases as T^3 , since the phonon group velocity is a constant and the specific heat increases with

T^3 at temperatures below the Debye temperature. However, in the hydrodynamic regime, thermal conductivity was found to increase with temperature faster than the ballistic case^{19,20,24}. This unique temperature dependence in the hydrodynamic regime was used to experimentally confirm the steady-state hydrodynamic flow of phonons. In the past study, the thermal conductivity of solid He increases as T^8 at low temperature, much different from the T^3 trend of the ballistic case¹⁰⁷. For the experimental confirmation of the phonon Poiseuille flow in graphene, it would be important to see if the thermal conductivity of graphene exhibits a peculiar temperature dependence that is clearly distinguished from the ballistic case.

In Figure 9, we show the temperature dependence of thermal conductivity in suspended graphene from the MC simulation. The dashed lines serve as an eye guide for the ballistic transport. Note that the ballistic thermal conductance in graphene increases as $T^{1.68}$, different from the three-dimensional Debye crystal case¹⁰⁸. This is because graphene has a flexural acoustic phonon branch that has a quadratic dispersion relation in a two-dimensional space. In Figure 9, it is observed that thermal conductivity increases with temperature faster than that of the ballistic transport in the temperature range from 50 to 100 K. The temperature dependence of thermal conductivity in this temperature range varies from $T^{1.89}$ to $T^{2.49}$ for different widths, which is clearly distinguished from the trend of $T^{1.68}$ of the ballistic case. When the temperature is higher than 100 K, the thermal conductivity decreases with temperature due to the increased U-scattering rate.

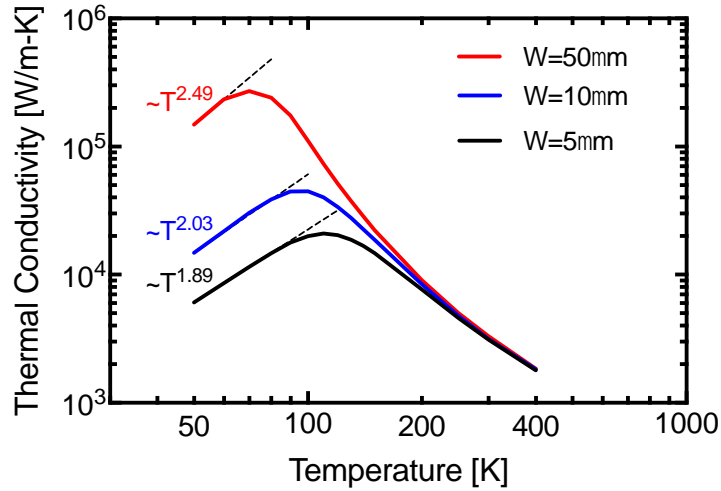


Figure 9 Temperature dependence of thermal conductivity for different sample widths. The dashed lines represent the exponential fit of the results. Thermal conductivity increases faster than the ballistic case as temperature increases, indicating phonon Poiseuille flow. The exponent of temperature is obtained by fitting the data from 50 K to 80 K (5 μm and 10 μm) and from 50 K to 60 K (50 μm). Reproduced with permission from [89].

Copyright 2018 American Physical Society.

This peculiar temperature dependence can be explained, as discussed in section 1.2.2.2, by the kinetic theory combined with a simple random walk theory^{19,24}. Here we propose that it can also be explained by the momentum balance equation (Eq. (3-7)) and the concept of phonon hydrodynamic viscosity. The phonon hydrodynamic viscosity is inversely proportional to the N-scattering rate according to Eq. (3-8), meaning that a momentum transfer rate decreases as N-scattering becomes stronger. This observation agrees with the aforementioned random walk picture. With higher N-scattering rate, the boundary can be more effectively screened and the momentum transfer rate to the boundary becomes less. Therefore, if the viscous damping effect is the major contributor to thermal resistance, strong N-scattering can decrease thermal resistance. In Figure 10, we present the phonon hydrodynamic viscosity of suspended graphene that is calculated with phonon dispersion and scattering rates from the first principles calculation. The phonon

hydrodynamic viscosity decreases with temperature because N-scattering rate is increased. Thus, the thermal conductivity should exhibit a steep increase with temperature if the viscous damping effect significantly contributes to the total thermal resistance. We show the temperature dependence of thermal conductivity (Eq. (3-10)) in Figure 10. The calculated thermal conductivity from the momentum balance equation increases approximately as T^2 , similar to our MC results shown in Figure 9.

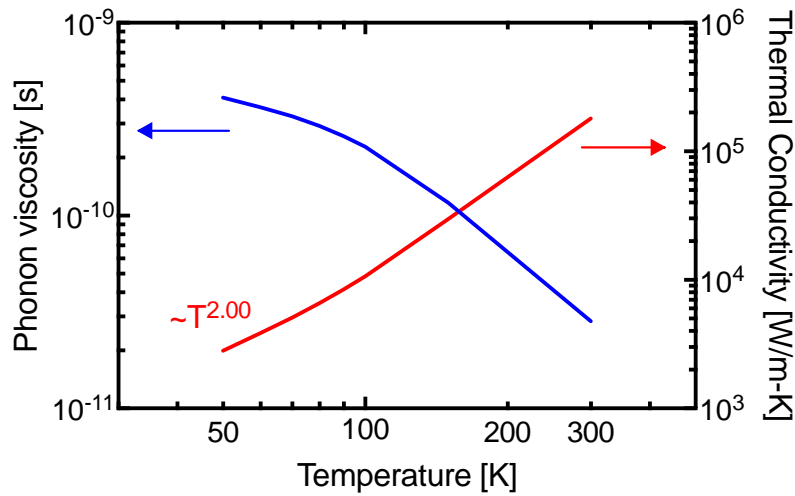


Figure 10 Temperature dependence of phonon viscosity and thermal conductivity. The phonon viscosity decreases with temperature, resulting in thermal conductivity increasing with temperature faster than the ballistic case. The exponent of temperature is obtained by fitting the data in the temperature range from 50 to 100 K.

Reproduced with permission from [89]. Copyright 2018 American Physical Society.

It should be noted from Eq. (3-10) that thermal conductivity is inversely proportional to hydrodynamic viscosity. As viscosity decreases, viscous damping becomes smaller and thermal conductivity can be larger, as shown in Figure 10. Equation (3-10) also indicates that thermal conductivity should have the same exponent value of temperature regardless of widths. This contradicts to our results from MC solution shown in Figure 9. It is observed in Figure 9 that different widths result in different values of exponent; the exponent value increases with the width.

The exponent value from our MC simulation depends on the width because the no-slip boundary condition assumed in Eq. (3-10) is not completely satisfied in the actual cases. The normalized heat flux profile in Figure 11 shows non-zero heat flux near the boundaries. The heat flux near the boundaries becomes larger as the width becomes smaller.

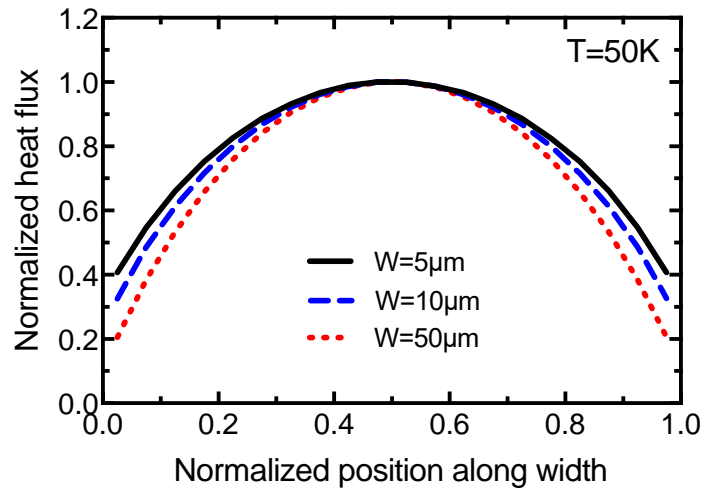


Figure 11 Normalized heat flux profile at 50 K, for sample widths of 5, 10, and 50 μm . The displacements near the boundaries are not zero and increase as the width decreases. The non-zero displacements indicate slip boundary condition. Reproduced with permission from [89]. Copyright 2018 American Physical Society.

This slip boundary condition occurs due to a ballistic effect. In the limit of very strong N-scattering and very short MFP of N-scattering, the displacement near the boundary should approach to zero. However, if MFP of N-scattering is not much smaller than the width, the displacement can be larger than zero, due to the contributions of phonons travelled without scattering from the center of a sample where the displacement is large. The slip displacement reduces the viscous damping effect by flattening the heat flux profile. This can lead to smaller exponent value of temperature in the thermal conductivity shown in Figure 9.

The role of viscous damping effect in thermal resistance can also be found from the shape of heat flux profile. The heat flux profile shape is almost uniform when U-scattering is the major source for the thermal resistance as U-scattering can occur at any place of a sample. However, when the viscous damping by N-scattering is important, the heat flux profile varies in space and the momentum transfer along the drift velocity gradient can occur. In Figure 12(a), we present the profiles of local thermal conductivity, i.e., heat flux per temperature gradient, at 100 K and 300 K. At 300 K, the local thermal conductivity is almost constant in the entire cross-section, indicating that the direct destroy of momentum by U-scattering is the largest contributor to the total thermal resistance. At 100 K, the local thermal conductivity nearly follows the parabolic shape that is observed in molecular Poiseuille flow. Due to the drift velocity gradient, momentum can be transferred to the wall through many N-scattering events. In this case, the thermal resistance is mostly due to the viscous damping effect, as also can be seen from the peculiar temperature dependence of thermal conductivity shown in Figure 9.

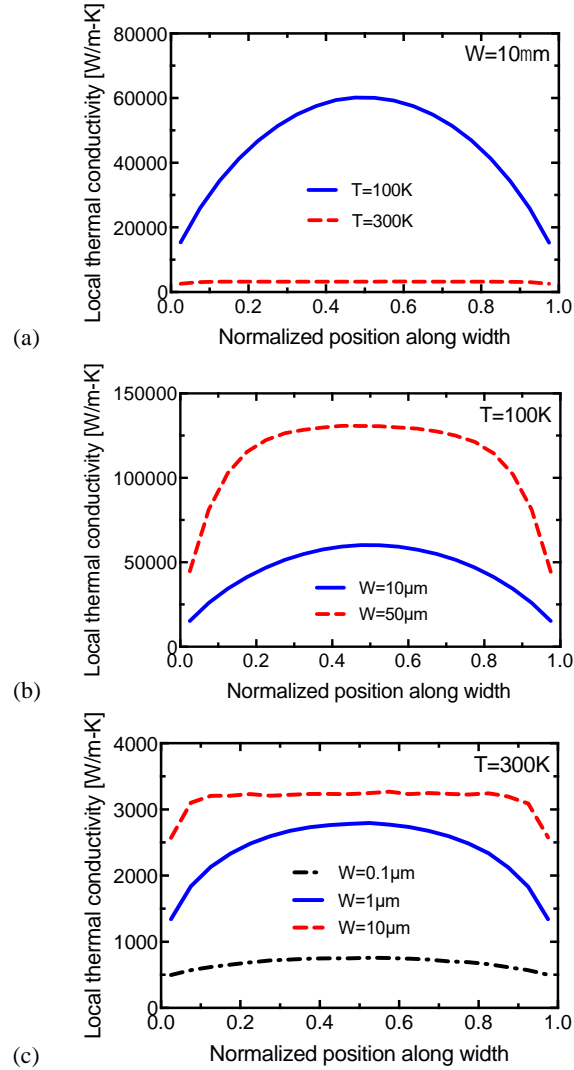


Figure 12 Local thermal conductivity profile from the MC simulation under different conditions. (a) 100 K and 300 K for 10 μm wide sample, (b) sample widths of 10 μm and 50 μm at 100 K, and (c) sample widths of 0.1 μm , 1 μm , and 10 μm at 300 K. Reproduced with permission from [89]. Copyright 2018 American Physical Society.

3.4.2 Sample width dependence of thermal conductivity

All three transport regimes exhibit different behavior of thermal conductivity changes as the sample width changes. In the ballistic regime, phonon MFP is limited to the characteristic sample size, thus thermal conductivity increases linearly with a width. In the diffusive regime,

thermal conductivity does not change with a width. In contrast, thermal conductivity in the hydrodynamic regime increases superlinearly with a sample width^{13,25,26,108}. In the ideal hydrodynamic regime where there is no U-scattering and a sample size is much larger than the MFP of N-scattering, thermal conductivity should increase as W^2 . This can be easily shown from the random walk picture or the momentum balance equation (Eq. (3-7)), assuming there is no U-scattering. However, with the existence of U-scattering, thermal conductivity would follow the trend of W^α where α is less than 2.

In Figure 13, we present the dependence of thermal conductivity on sample widths from our MC simulation. At 300 K, thermal conductivity depends on sample widths very weakly; the width dependence is $W^{0.17}$ in the range of width from 1 to 5 μm . For widths larger than 5 μm , the thermal conductivity is almost the same as the thermal conductivity of infinitely large sample. This suggests that the momentum destroy by U-scattering is stronger than the viscous damping effect at 300 K.

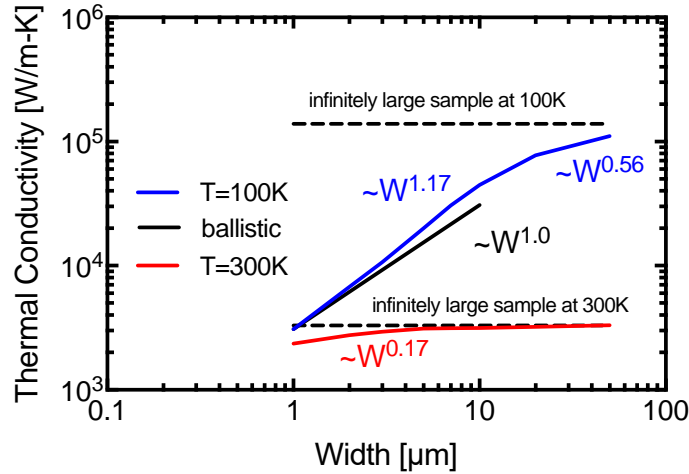


Figure 13 Sample width dependence of thermal conductivity at 100 K and 300 K. The dashed lines represent the thermal conductivities for an infinitely large sample. The black solid line represents the ballistic case, where thermal conductivity is linearly proportional to a width. The thermal conductivity at 100 K superlinearly increases with a width, indicating the significant hydrodynamic regime. Reproduced with permission from [89]. Copyright 2018 American Physical Society.

In contrast, the thermal conductivity at 100 K clearly shows a superlinear increase with a width; the dependence is $W^{1.17}$ in the range of widths from 1 to 10 μm . As a width is further increased, the width dependence is weaker, showing a sublinear dependence. The transition from the strong dependence $W^{1.17}$ to the weak dependence $W^{0.56}$ at 100 K can be explained by the relative strength of viscous damping and U-scattering. At a fixed temperature, the thermal resistance by U-scattering is constant regardless of widths. However, the viscous damping effect varies with sample widths. From the momentum balance equation, the momentum transfer rate is proportional to hydrodynamic phonon viscosity and the gradient of drift velocity. As a width increases, the gradient of drift velocity is decreased, making the viscous damping effect smaller. When a width is between 1 and 10 μm , the viscous damping effect is relatively stronger than the momentum destruction by U-scattering, giving the superlinear dependence of thermal conductivity

on widths. However, as the width further increases, the viscous damping effect decreases, and the transport regime becomes closer to the diffusive limit. This behavior can be also seen in the local thermal conductivity profile shown in Figure 12(b). When the width is 10 μm , the local thermal conductivity has nearly parabolic profile shape, indicating that the viscous damping is the major source of thermal resistance. However, when a width is 50 μm , the local thermal conductivity profile is flattened and the momentum transfer to the wall is relatively insignificant compared to the 10 μm case.

3.5 Transition from hydrodynamic to diffusive regimes

We have focused on the peculiar behaviors of thermal conductivity at 100 K where the hydrodynamic regime is dominant over other regimes. Although 300 K case does not exhibit the peculiar behaviors of temperature and width dependent thermal conductivity of the hydrodynamic regime, the MFP of N-scattering is still significantly smaller than those of U-scattering as shown in Figure 14. This suggests that N-scattering and the resulting viscous damping may still play an important role in the thermal transport.

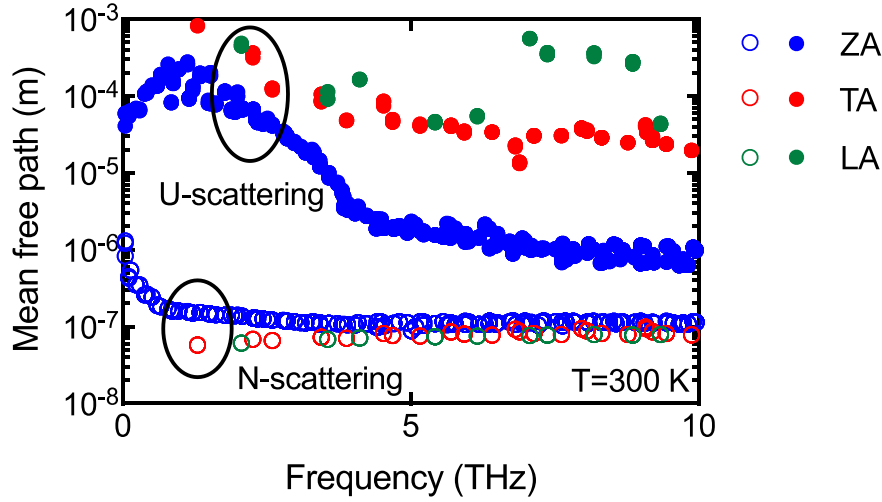


Figure 14 Comparison of MFPs of N- and U-scatterings at 300 K. The filled circles are for U-scattering and the void circles are for N-scattering. Reproduced with permission from [89]. Copyright 2018 American Physical Society.

In Figure 15, we compare the thermal conductivity values from two different methods. One is from our MC solution where we consider the spatial variation of phonon distribution and solve the PBE in both real and reciprocal spaces (hereafter κ_{MC} represents the thermal conductivity values from MC solution). The other is from the iterative solution where we ignore the spatial variation of phonon distribution and assume a simple homogenous boundary scattering¹⁰² (hereafter κ_{homo} represents the thermal conductivity values from the homogenous boundary scattering). This comparison was reported in recent two papers^{26,109} and the difference between the two methods was used to explain the friction effects in the relaxon framework⁸⁶. Here we use the conventional phonon concept to explain the difference. In the homogenous boundary scattering model (Eq. (3-1)), the boundary scattering acts like a momentum sink that is homogeneously distributed in space, and its rate is based on the assumption of ballistic transport to the boundary. Therefore, the homogenous boundary scattering model cannot capture the viscous damping effect

that occurs due to many N-scattering events and the gradient of drift velocity. As the homogenous boundary scattering assumes that the phonon particles directly see the boundary, it overestimates thermal resistance compared to the actual case where the boundary is screened by many N-scattering events.

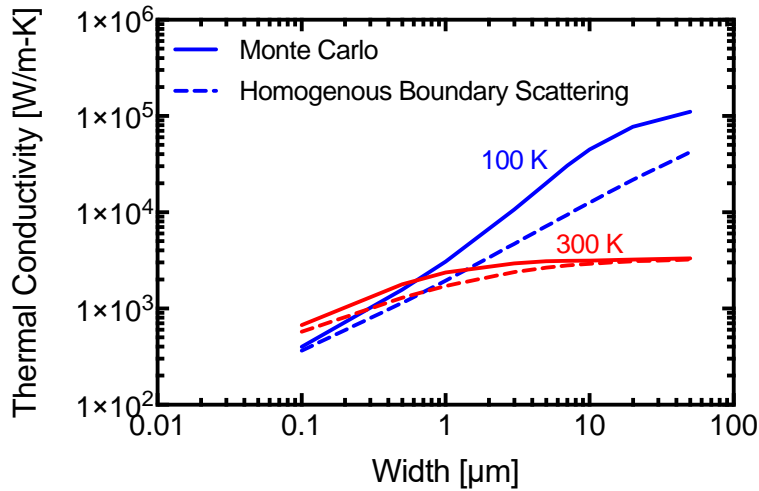


Figure 15 Comparison of thermal conductivity values with different boundary scattering models. Solid line is for spatially non-homogenous boundary scattering by MC simulation, and dashed line is for spatially homogenous boundary scattering. The difference between them shows the significance of the viscous damping effect.

Reproduced with permission from [89]. Copyright 2018 American Physical Society.

It is found in Figure 15 that κ_{MC} is significantly larger than κ_{homo} at 100 K where we predicted the hydrodynamic regime is dominant over other regimes. In this case, the viscous damping is the major contributor to the thermal resistance, and therefore the homogenous boundary scattering model cannot accurately predict the thermal conductivity values. When a width is very small (0.1 μm) or exceedingly large ($> 50 \mu\text{m}$) representing the cases that are close to the ballistic or diffusive limits, respectively, the difference between κ_{MC} and κ_{homo} is small. It is noteworthy that κ_{MC} is larger than κ_{homo} by 40% even at 300 K where the peculiar temperature and width dependences of thermal conductivity in the hydrodynamic regime do not exist. This

indicates that the viscous damping effect can still play an important role at 300 K, even though the transport is not clearly in the hydrodynamic regime but in between the hydrodynamic and diffusive limits.

The phonon distribution and heat flux profile also support that the viscous damping effect is still important at 300 K. For the hydrodynamic viscosity to be well defined, a collective motion of phonon particles with the same drift velocity is necessary. We show in Figure 16 that the phonon particles at 300 K form a clear collective motion. The slope in Figure 16 represents the drift velocity of each phonon state. It is clear that all phonon modes, regardless of phonon wavevector and polarization, exhibit the same drift velocity in the phonon states with small wavevectors which contribute the most of heat flux. In addition, the local thermal conductivity profile in Figure 12(c) also indicates that viscous damping effect can be significant at 300 K when a width is around 1 μm . The local thermal conductivity profile in this case exhibits a large gradient along the width-direction, indicating that the viscous damping effect can be significant. However, when a width is 0.1 μm or 10 μm , the local thermal conductivity profile is almost uniform, and the viscous damping effect is almost negligible.

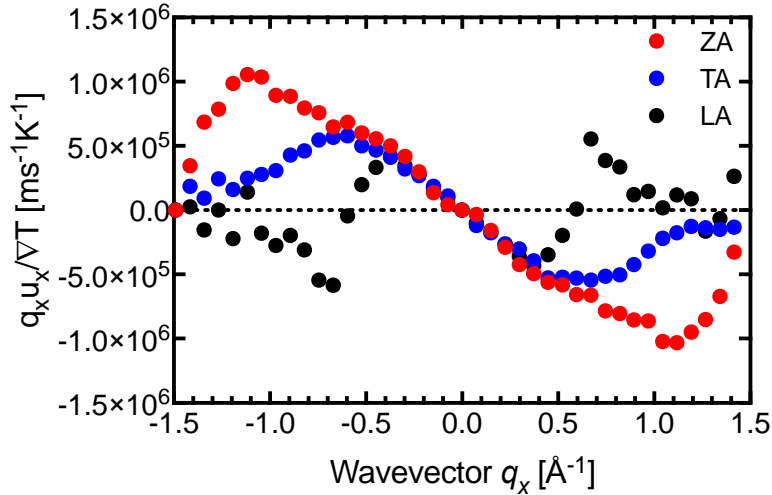


Figure 16 Deviation of phonon distribution from equilibrium case from MC simulation of the PBE. The phonon distribution is sampled at the center of 1 μm wide sample at 300 K. The slope between two adjacent phonon states (circles) represent the drift velocity at the phonon state. Reproduced with permission from [89]. Copyright 2018 American Physical Society.

3.6 Conclusions

We have discussed the hydrodynamic phonon transport in suspended graphene using the MC solution of the PBE in both real and reciprocal spaces. Our solution of the PBE is based on the deviational MC method using the full scattering matrices from first principles lattice dynamics calculation, and thus holds the predictive power of the first principles calculations. We focus on the peculiar temperature and width dependences of thermal conductivity when the hydrodynamic regime is dominant over the diffusive and ballistic regimes. The calculation shows that thermal conductivity values follow the trends of T^α where α ranges from 1.89 to 2.49, and $W^{1.17}$ when the temperature is around 100 K and widths are from 1 to 10 μm . These behaviors are clearly distinguishable from those of the ballistic and diffusive limits, thus can serve as an indicator of

hydrodynamic regime. Our calculation results can be used to guide future experimental studies to confirm the phonon Poiseuille flow.

The peculiar behaviors of thermal conductivity are qualitatively explained with the concept of phonon hydrodynamic viscosity. We derived a momentum balance equation from the PBE using the Callaway's scattering model to separate N- and U-scatterings and defined the phonon hydrodynamic viscosity. It is found that the hydrodynamic viscous damping is a significant contributor to thermal resistance at 100 K where the hydrodynamic regime is dominant. The viscous damping effect still plays an important role in thermal transport when the temperature is 300 K and the width is around 1 μm , even though the transport regime in this condition is not clearly hydrodynamic but in a transition between the hydrodynamic and diffusive regimes.

4.0 Crossover of ballistic, hydrodynamic, and diffusive regimes in suspended graphene

Many of past studies on hydrodynamic phonon transport have focused on the cases where the hydrodynamic regime is significantly stronger than other regimes such that hydrodynamic features can be clearly observed. However, this often requires stringent conditions of temperature and sample size. In many cases, the transport cannot be characterized by a single regime, but the features of all three regimes – ballistic, hydrodynamic, and diffusive regimes – exist to some extent. Here we assess the extent of three regimes by comparing momentum destruction rates by three different mechanisms, each of which represents a different regime: diffuse boundary scattering without internal phonon scattering (ballistic regime), diffuse boundary scattering combined with N-scattering (hydrodynamic regime), and U-scattering (diffusive regime). We solve the PBE with an *ab initio* full scattering matrix using the deviational MC method. We sample distribution functions of ballistic and scattered particles separately, and thereby compare the momentum destruction rates by the three different mechanisms. Using this framework, we discuss a well-known phenomenon of ballistic-to-hydrodynamic crossover, called phonon Knudsen minimum.

4.1 Background

The strong hydrodynamic regime has been discussed using two representative phenomena: phonon Poiseuille flow^{13,14,19,20,24,26,89,110,111} and second sound^{13,14,19,22,34,112}. However, in many practical situations when the conditions for the strong hydrodynamic regime are too stringent to

be met, the transport is in the crossover of different regimes. In these cases, the features from all three regimes – the ballistic, hydrodynamic, and diffusive regimes – can coexist. The transport phenomena then become complicated and not easy to understand. A map of three transport regimes in the temperature and sample size space was often determined by comparing mode-averaged MFP with sample size^{13,14,19,113}. For example, Guyer and Krumhansl suggested a condition for the phonon Poiseuille flow as

$$\lambda_N \ll R \ll \sqrt{\lambda_N \lambda_U} \quad (4-1)$$

where λ_N and λ_U are mode-averaged MFPs of N- and U-scattering¹⁹. The R is a characteristic sample size, e.g., the diameter of a rod for three-dimensional materials. If R is much smaller than λ_N , the transport is ballistic; if R is much larger than $\lambda_N \lambda_U$, the transport is diffusive. However, the MFPs of N- and U-scattering often have an extensively wide range with respect to phonon frequency, causing an overlap with each other in some cases. In addition, the criteria are useful only when the characteristics of one regime are significantly stronger than those from other regimes and cannot properly describe a transition across two different regimes. The three parameters (λ_N , R , and $\lambda_N \lambda_U$) are often in the similar order, and thus the transport regime has the characteristics of all three regimes in many cases. Then, the transport phenomena cannot be described by a single transport regime, and the detailed understanding of such cases is still lacking.

For the cases where the transport features from all three regimes coexist, it is desired that we can quantitatively measure the extent of all three regimes. For this purpose, we can check the momentum balance of a phonon system. Regardless of its transport regime, phonons are driven by a temperature gradient. In other words, the phonon system gains a net momentum from a temperature gradient. When the phonon flow is at steady state, the momentum gain is balanced with momentum destruction by three mechanisms, each of which represents a different regime:

the diffuse boundary scattering without internal phonon scattering (ballistic regime), the diffuse boundary scattering combined with N-scattering (hydrodynamic regime), and U-scattering (diffusive regime). Analyzing the momentum balance is directly relevant to understanding thermal transport phenomena when the hydrodynamic regime contributes to the actual phonon transport. In an ideal hydrodynamic regime where phonons exhibit a collective motion, the heat flux is linearly proportional to the net momentum of the phonon system.

We quantitatively measure the momentum destruction rates by the aforementioned three mechanisms in suspended graphene. An advantage of MC simulation is that we can sample distribution functions for scattered and unscattered particles separately¹¹⁴. By doing so, we can quantitatively show the contributions of thermal conductivity and momentum destruction rate from the three regimes.

4.2 Defining ballistic and scattered particles

In this work, we divide phonon particles into scattered and ballistic particles depending on whether a particle has experienced internal phonon scattering (scattered) or not (ballistic). In the MC simulation, each particle carries a label indicating ballistic or scattered. All particles generated from initialization, temperature gradient, or diffuse boundary scattering are labeled as ballistic particles as they did not experience internal phonon scattering. The diagonal terms of the matrix \mathbf{P} represent the case where neither N- nor U-scattering occurs during Δt and thus the phonon state is not changed. Therefore, upon an internal phonon scattering, the energy distribution function for the ballistic particles can be updated with

$$e_{i,\text{ballistic}}^{\text{d}}(t + \Delta t) = P_{ii}(\Delta t)e_{i,\text{ballistic}}^{\text{d}}(t) \quad (4-2)$$

which describes a ballistic particle at t remains as ballistic at $t + \Delta t$. The energy distribution function of scattered particles can be updated with

$$e_{i,\text{scattered}}^{\text{d}}(t + \Delta t) = \sum_{j \neq i} P_{ij}(\Delta t)e_{j,\text{ballistic}}^{\text{d}}(t) + \sum_j P_{ij}(\Delta t)e_{j,\text{scattered}}^{\text{d}}(t). \quad (4-3)$$

The first term includes off-diagonal terms of \mathbf{P} representing scattering. The second term is the contribution from scattered particles at t regardless of whether those particles experienced scattering or not during the time from t to $t + \Delta t$. Simply speaking, if a particle that is labeled as ballistic does not change its phonon state after t , it remains as ballistic. If a particle is determined to change its state, it is labeled as scattered. The ballistic and scattered distributions are calculated at each time step, by counting the number of particles for each label.

The local heat flux at \mathbf{r} from the ballistic and scattered particles can be expressed as

$$q''_{\alpha,x}(\mathbf{r}) = \frac{1}{NV} \sum_i \hbar\omega_i f_{\alpha,i}(\mathbf{r}) v_{i,x} \quad (4-4)$$

where α indicates ballistic or scattered label. The local heat flux can be calculated by summing the heat fluxes of all particles in a small grid volume. Then, the local thermal conductivity, $\kappa_{\alpha,xx}(\mathbf{r})$, can be simply found as $-q''_{\alpha,x}(\mathbf{r})/\nabla_{\mathbf{r}}T$.

For the momentum balance analysis, we would need to calculate the wall shear stress, which can be defined as the rate of momentum destruction by the diffuse boundary scattering per given time and area. The wall shear stress at the bottom wall ($y = 0$) can be expressed as

$$\tau_{\alpha}(y = 0) = \frac{1}{NV} \sum_{i, v_{i,y} < 0} q_{i,x} v_{i,y} f_{\alpha,i}(y = 0). \quad (4-5)$$

The wall shear stress in our MC simulation can be calculated by summing the x direction momentum of particles that cross the boundary during a given time interval.

A schematic of sample geometry and thermal gradient direction is shown in Figure 17. The sample is infinitely long in x direction. In this case, the phonon distribution function is invariant along the x direction except for the change due to a temperature gradient. Therefore, our boundary conditions at $x = 0$ and $x = L$ are⁹⁷

$$e(x = 0) = e(x = L) + \frac{de^0}{dT} L \nabla_x T. \quad (4-6)$$

For the top and bottom boundaries at $y = 0$ and $y = W$, an adiabatic boundary condition with complete diffuse boundary scattering is applied. The time, real, and reciprocal space domains are discretized. The time step is chosen such that it is smaller than the minimum lifetime of the phonons with frequencies below $k_B T / \hbar$. The real-space domain is discretized uniformly into 20 control volumes along y direction and one control volume with a length of 10 nm along x direction where a temperature gradient of 1000 K/m is applied. A 40×40 grid is used to sample the reciprocal space. It was confirmed that the calculation results reasonably converge with respect to all discretization variables.

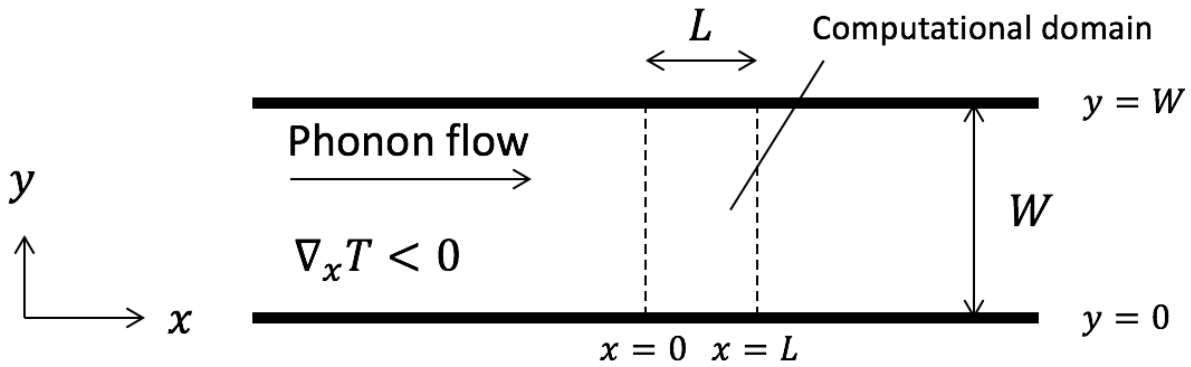


Figure 17 A schematic picture of an infinitely long graphene sample for MC simulation. Reproduced with permission from [16]. Copyright 2019 American Physical Society.

4.3 Decomposition of thermal conductivity

In Figure 18, we show the total and decomposed thermal conductivity values with respect to sample width at 100 K. Both contributions from the ballistic and scattered particles increase with increasing sample width, but the dominant contributor differs for different sample width. At small width below 100 nm, the ballistic contribution is much larger than the scattered contribution since internal phonon scattering is very weak compared to the diffuse boundary scattering. In the mid-range of sample width, the ballistic and scattered contributions have a crossover, indicating that the dominant transport regime is changed from ballistic to non-ballistic regimes. As width increases further and becomes larger than 1 μm , most of the heat flux comes from the scattered particles.

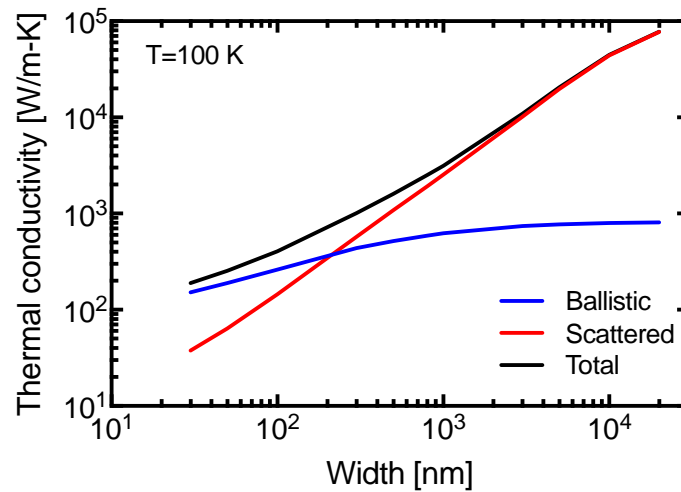


Figure 18 Ballistic and scattered particles contribution to total thermal conductivity with respect to sample width at 100 K. Reproduced with permission from [16]. Copyright 2019 American Physical Society.

This decomposition of thermal conductivity clearly distinguishes the ballistic regime from the other two regimes (i.e., the hydrodynamic and diffusive regimes) at small sample width and

shows the transition of transport regimes. However, for large sample width, there still exists a need to distinguish between the hydrodynamic and diffusive regimes.

4.4 Decomposition of shear stress

A fundamental difference between the hydrodynamic and diffusive regimes lies in the momentum conservation upon a phonon-phonon scattering process. In an ideal hydrodynamic regime where N-scattering is the only internal scattering mechanism, the total phonon momentum is always conserved upon internal phonon scattering; however, the total phonon momentum in an ideal diffusive regime is destroyed upon internal phonon scattering. Therefore, analyzing phonon momentum can serve as a basis to distinguish between the hydrodynamic and diffusive regimes. The x direction momentum (Φ_x) of the phonon system can be defined as the sum of the momentum of all phonon states, i.e.,

$$\Phi_x = \frac{1}{NV} \sum_i q_{i,x} f_i. \quad (4-7)$$

Phonon flow is driven by a temperature gradient, creating a net phonon momentum ($\dot{\Phi}_{VT,x}$). If we assume a steady-state phonon flow, the momentum creations should be balanced with momentum destructions by the direct diffuse boundary scattering without internal phonon scattering (ballistic, $\dot{\Phi}_{B,x}$), the diffuse boundary scattering combined with N-scattering (hydrodynamic, $\dot{\Phi}_{H,x}$), or internal U-scattering (diffusive, $\dot{\Phi}_{D,x}$). The momentum balance can be expressed as

$$\dot{\Phi}_{VT,x} = \dot{\Phi}_{B,x} + \dot{\Phi}_{H,x} + \dot{\Phi}_{D,x}. \quad (4-8)$$

The momentum gain from a temperature gradient, $\dot{\Phi}_{\nabla T,x}$, for the computational domain shown in Figure 17 can be found as

$$\dot{\Phi}_{\nabla T,x} = \frac{W\delta}{NV} \sum_i q_{i,x} v_{i,x} \frac{\partial f_i^{\text{eq}}}{\partial T} L(-\nabla_x T) \quad (4-9)$$

where δ is the thickness of graphene assumed as 0.335 nm. The ballistic and hydrodynamic momentum destructions, $\dot{\Phi}_{B,x}$ and $\dot{\Phi}_{H,x}$, can be calculated based on the wall shear stress from the ballistic and scattered particles as follows:

$$\dot{\Phi}_{B,x} = L\delta(\tau_{\text{ballistic},y=0} + \tau_{\text{ballistic},y=L}), \quad (4-10)$$

$$\dot{\Phi}_{H,x} = L\delta(\tau_{\text{scattered},y=0} + \tau_{\text{scattered},y=L}). \quad (4-11)$$

Then, the momentum destruction due to internal U-scattering, $\dot{\Phi}_{D,x}$, is simply calculated as $\dot{\Phi}_{\nabla T,x} - \dot{\Phi}_{B,x} - \dot{\Phi}_{H,x}$ from the momentum balance in Eq. (4-8).

In Figure 19, we show the momentum balance as width increases. The black line represents the momentum destruction rate by the wall shear stress of both ballistic and scattered particles ($\dot{\Phi}_{B,x} + \dot{\Phi}_{H,x}$), calculated from the MC solution of the PBE. The green dashed line shows the momentum gain from a temperature gradient, $\dot{\Phi}_{\nabla T,x}$, from Eq. (4-9). When sample width is small and less than 3 μm , the momentum destructions by the wall shear stress are equal to the momentum gains from a temperature gradient, indicating that all the momentum gains from a temperature gradient are dissipated by the wall shear stress and that the internal momentum destruction by U-scattering is negligible. Therefore, for width less than 3 μm , the diffusive regime can be ignored, and the actual transport regime is ballistic or hydrodynamic. In order to distinguish between the ballistic and hydrodynamic regimes, we separate the ballistic and scattered particles. When width is smaller than 100 nm, the ballistic contribution is dominant, indicating a strong ballistic regime. For width between 100 nm and 500 nm, the scattered contribution gradually increases, showing a

smooth transition from the ballistic to hydrodynamic regimes. For width from 500 nm to 3 μm , the scattered contribution is dominant and the major mechanism of thermal resistance in this width range is the diffuse boundary scattering combined with N-scattering, namely the viscous damping⁸⁹. Again, as $\dot{\Phi}_{B,x} + \dot{\Phi}_{H,x}$ is equal to $\dot{\Phi}_{\nabla T,x}$ and $\dot{\Phi}_{D,x}$ is negligible, most of the internal phonon scattering processes that particles experience are N-scattering type in this width range. When width is further increased and larger than 3 μm , $\dot{\Phi}_{B,x} + \dot{\Phi}_{H,x}$ deviates from $\dot{\Phi}_{\nabla T,x}$. The difference between $\dot{\Phi}_{B,x} + \dot{\Phi}_{H,x}$ and $\dot{\Phi}_{\nabla T,x}$ represents the momentum destruction by U-scattering according to the momentum balance in Eq. (4-8). From the width of 3 μm , U-scattering starts to cause thermal resistance and the importance of the diffusive regime gradually increases as width increases.

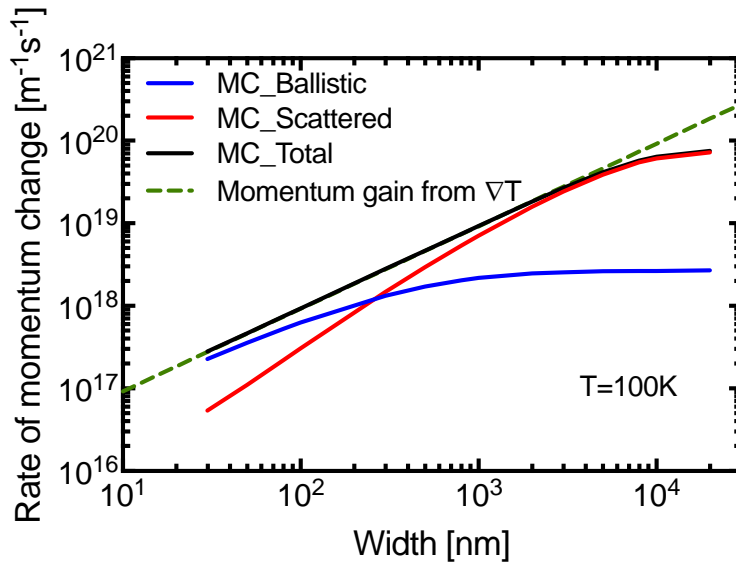


Figure 19 The momentum balance at 100 K. The difference between the green and black lines represents the momentum destruction by U-scattering. Reproduced with permission from [16]. Copyright 2019 American Physical Society.

In Figure 20, we show the rates of momentum destruction, $\dot{\Phi}_{B,x}$, $\dot{\Phi}_{H,x}$, and $\dot{\Phi}_{D,x}$ normalized by $\dot{\Phi}_{VT,x}$ at different temperatures. In Figure 20(a), the ballistic regime is strong for width below 100 nm, while the hydrodynamic regime is significant in a range of width from 300 nm to 10 μm . With sample width increasing, the ballistic-hydrodynamic-diffusive transition is clearly shown in Figure 20(a). At higher temperatures shown in Figure 20(b) and Figure 20(c), U-scattering becomes stronger, making the diffusive regime stronger than the 100 K case. The significance of the hydrodynamic regime is thus weakened. The hydrodynamic regime is significant only for a narrow window of sample width or is not strong in the entire range of sample width depending on temperature. For example, at 200 K shown in Figure 20(b), the hydrodynamic regime accounts for more than 50 % of total momentum destructions in a width range from 300 nm to 500 nm, which is narrower than that at 100 K. When temperature is 300 K as shown in Figure 20(c), the hydrodynamic regime is not important for any sample width.

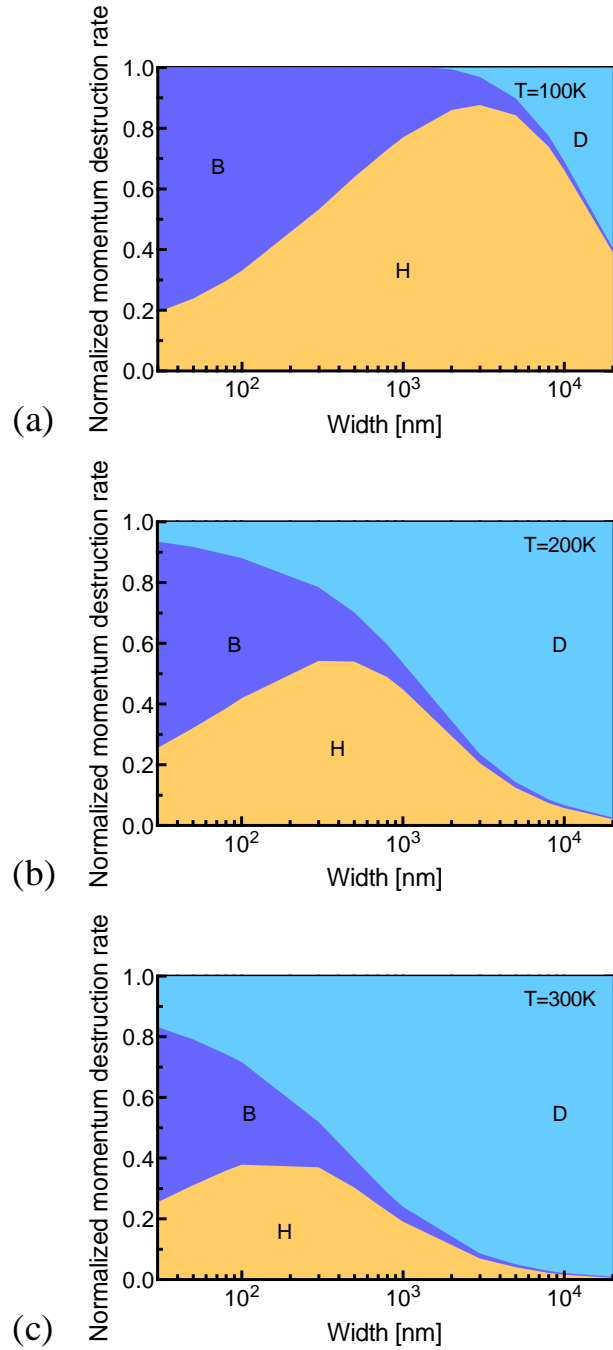


Figure 20 Normalized momentum destruction rates at different temperatures, (a) 100 K, (b) 200 K, and (c) 300 K. Dark blue, yellow, and light blue represent the ballistic, hydrodynamic, and diffusive regimes, respectively.

Reproduced with permission from [16]. Copyright 2019 American Physical Society.

The four-phonon scattering was recently predicted to be important for graphene using the optimized Tersoff potential¹¹⁵. The momentum analysis to study the behavior of transport regime crossover can be applicable regardless of the type of phonon scattering and is valid with four-phonon scattering. However, the inclusion of four-phonon scattering would reduce the MFPs of N- and U-scattering from the three-phonon scattering only case, thereby changing the length scale where the crossover occurs shown in Figure 20.

4.5 Transition from ballistic to hydrodynamic regimes

The Knudsen minimum is a representative phenomenon of ballistic-to-hydrodynamic transition. Molecular Knudsen minimum was reported by Knudsen¹¹⁶ around a century ago and had been debated for its existence until the Boltzmann transport equation for molecules was carefully solved in 1960s¹¹⁷. Phonon Knudsen minimum was observed at extremely low temperatures^{118,119} and its existence in graphite at much higher temperatures was recently predicted using *ab initio* phonon dispersion and scattering rates²⁷. Phonon Knudsen minimum can be found in the dimensionless thermal conductivity defined as

$$\kappa^* = \frac{\kappa T}{C v_0 W} \quad (4-12)$$

where C is the energy density in phonon hydrodynamics such that $C u_x$ is the heat flux where u_x is the drift velocity¹²⁰. The v_0 is an average group velocity. The dimensionless thermal conductivity is defined such that it only depends on Knudsen number and its physical meaning is a space-averaged dimensionless drift velocity at a given dimensionless temperature gradient.

4.5.1 Semi-analytic solution of the PBE with the Callaway's scattering model

The dimensionless thermal conductivity can be calculated from a semi-analytic solution of the PBE. A similar solution for the Boltzmann equation of molecules can be found in literature¹¹⁷, and it was recently applied for phonons in graphite²⁷. A difference between phonons and molecules is that phonons experience momentum-destroying scattering (U-scattering). For our derivation, we use the Callaway's scattering model which can be understood as the Bhatnagar-Gross-Krook scattering model of the molecule system with an additional momentum-destroying scattering term. For the sake of simplicity, the detailed derivation is not discussed here, but can be found in the supplementary information of our recent study¹⁶.

4.5.2 Phonon Knudsen minimum

In Figure 21, we present the dimensionless thermal conductivity for a Debye phonon dispersion from the semi-analytic solution of the PBE¹⁶. When there is no U-scattering, i.e., $\tau_N/\tau_U = 0$ where τ_N^{-1} and τ_U^{-1} represent the N- and U-scattering rates, respectively, the dimensionless thermal conductivity has a minimum point around $\text{Kn} = 1$, so called phonon Knudsen minimum. For $\tau_N/\tau_U = 0.1$, the dimensionless thermal conductivity exhibits a slow decrease when inverse Knudsen number is below 5, but then rapidly decreases, leaving no minimum point. As U-scattering rate is further increased, the dimensionless thermal conductivity is converged to the Fuchs-Sondheimer solution^{8,121} which assumes all scattering events destroy the net momentum described by the RTA.

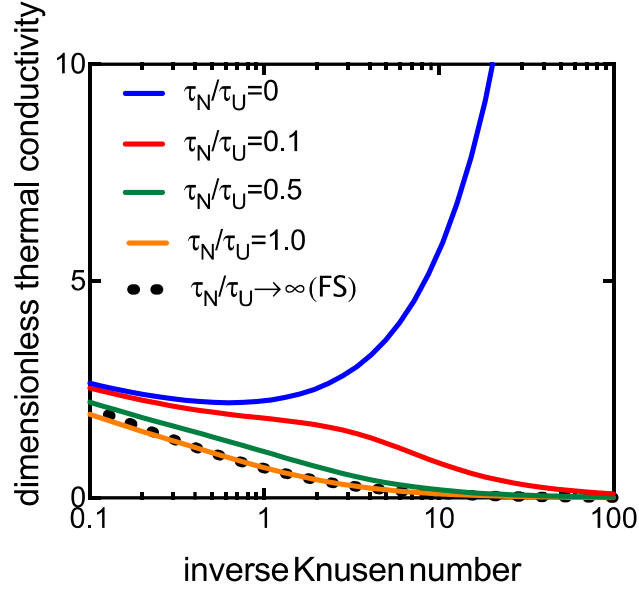


Figure 21 The dimensionless thermal conductivity with respect to inverse Knudsen number assuming a Debye phonon dispersion model. ‘FS’ refers to the Fuchs-Sondheimer solution of the PBE assuming no N-scattering.

Reproduced with permission from [16]. Copyright 2019 American Physical Society.

In Figure 22, we present the thermal conductivity normalized by sample width (κ/W), similar to the dimensionless thermal conductivity defined in Eq. (4-12), for suspended graphene at different temperatures. At 100 K, the normalized thermal conductivity exhibits phonon Knudsen minimum when width is around 1 μm , similar to the case without U-scattering in Figure 21. However, when width becomes larger than 10 μm , the κ/W decreases, implying the significant effect of U-scattering on thermal transport. At 200 K, the κ/W slowly decreases for width from 100 to 500 nm, but then rapidly decreases without a minimum point, similar to the case of $\tau_N/\tau_U = 0.1$ in Figure 21. At 300 K, the κ/W rapidly decreases for the entire width range.

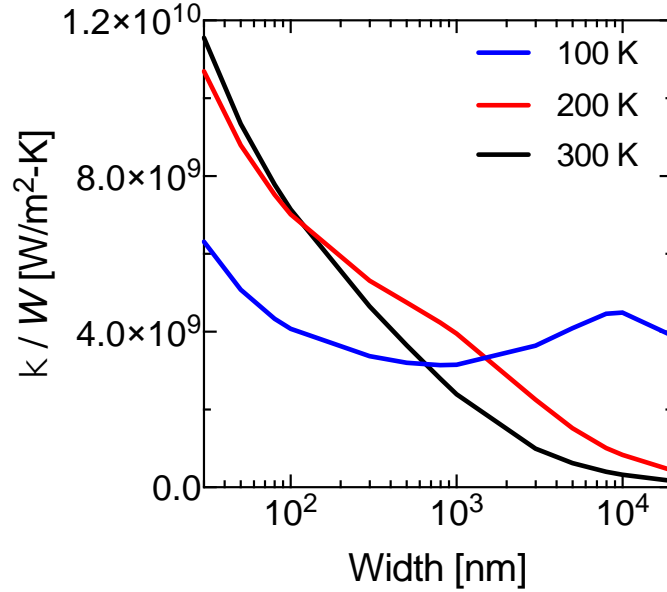


Figure 22 Thermal conductivity normalized by graphene sample width at 100, 200, and 300 K. Reproduced with permission from [16]. Copyright 2019 American Physical Society.

In Figure 23, we decompose κ/W into the ballistic and scattered contributions to further understand Knudsen minimum and the crossover of ballistic, hydrodynamic, and diffusive regimes. At 100 K in Figure 23(a), the thermal conductivity is mostly from ballistic particles for width below 300 nm, similar to the momentum balance shown in Figure 20(a). From 300 nm to 10 μm , the scattered contribution is much larger than the ballistic contribution. The scattered contribution of κ/W increases with width, and this behavior is particularly significant for width from 1 to 10 μm . The increasing trend of the scattered κ/W indicates that the hydrodynamic regime is much more significant than the diffusive regime⁸⁹, which also agrees well with the momentum balance in Figure 20(a). Due to the strong hydrodynamic behavior, the total κ/W increases with width, leaving a minimum point at 1 μm . When width is larger than 10 μm , the scattered κ/W decreases with width, which agrees well with the momentum balance in Figure 20(a) showing that the diffusive regime becomes significant at 10 μm .

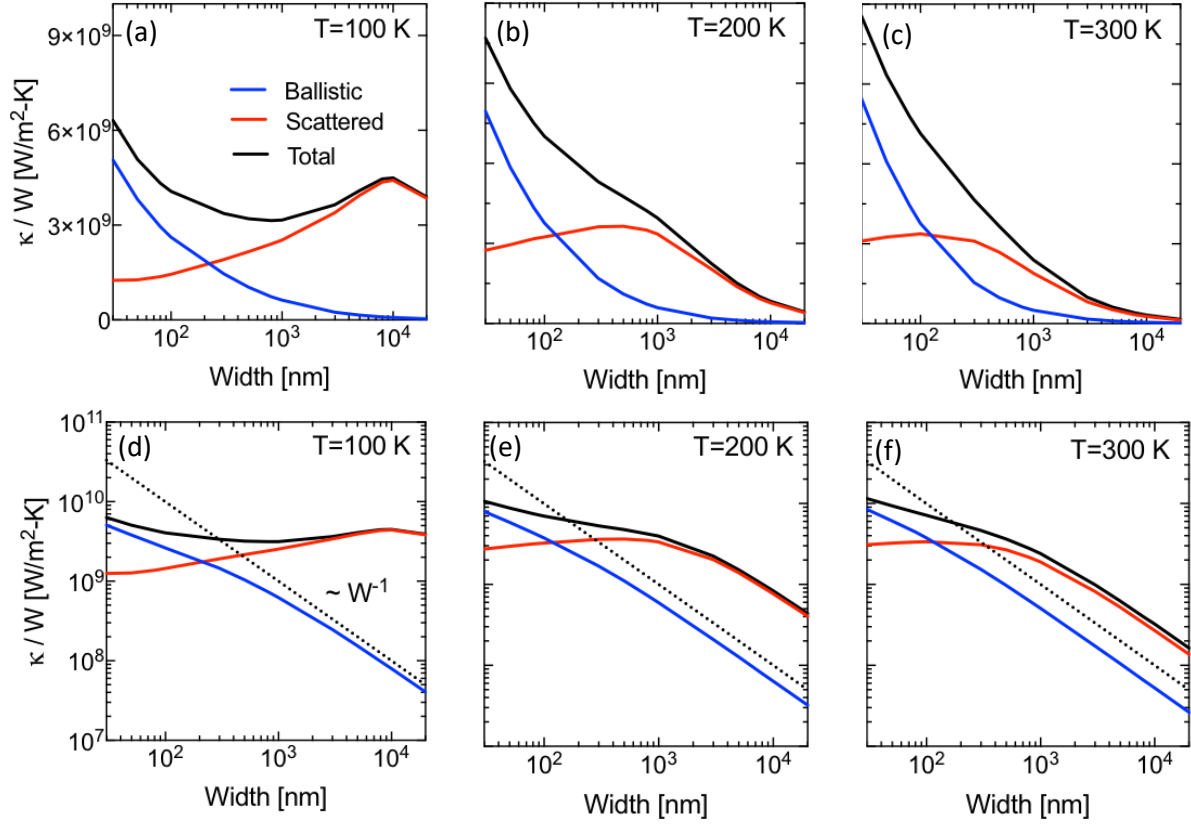


Figure 23 Normalized thermal conductivity contributions from the ballistic and scattered particles at 100, 200 and 300 K. For (d-f), the y-axis is in log scale and W^{-1} dependence is shown as the dotted line for eye-guide.

Reproduced with permission from [16]. Copyright 2019 American Physical Society.

At 200 K shown in Figure 23(b), the hydrodynamic behavior exists, but not as significant as the 100 K case. For width from 100 to 500 nm, the scattered κ/W increases with width, indicating that the hydrodynamic regime still plays an important role in this width range. This can also be confirmed from the momentum balance in Figure 20(b) showing significant hydrodynamic regime in the same width range. However, the increasing behavior of the scattered κ/W is less significant than the 100 K case, mainly due to larger U-scattering rates. From Figure 20(b), the momentum destruction by U-scattering already exists for width below 500 nm at 200 K, while it is negligible at 100 K. This results in a slower increase of the scattered κ/W , and Knudsen

minimum cannot be observed at 200 K. For width from 500 nm to 3 μm , the normalized thermal conductivity is mostly due to the scattered particles, but it does not follow W^{-1} dependence which represents constant thermal conductivity and strong diffusive regime (Figure 23(e)). This shows that the transport is not fully diffusive, and the hydrodynamic regime cannot be neglected. When width is larger than 3 μm , the normalized thermal conductivity follows W^{-1} , showing the fully diffusive regime where the thermal conductivity is a constant regardless of sample width. When temperature is 300 K (Figure 23(c) and (f)), the hydrodynamic features are further weakened. The normalized thermal conductivity does not show increasing behavior with width for any width larger than 100 nm. When width is larger than 1 μm , the dimensionless thermal conductivity is mostly due to the scattered particles, and it follows W^{-1} trend of the fully diffusive regime.

4.6 Conclusions

We have discussed the crossover of the ballistic, hydrodynamic, and diffusive regimes of phonon transport by decomposing the heat flow and wall shear stress into the ballistic and scattered particles contributions. This decomposition framework is applied in our deviational MC simulation of the PBE, where the phonon particles are labeled as scattered or ballistic depending on whether they have experienced internal phonon scattering or not. Using this framework, we compare three different momentum destruction mechanisms, and thus measure the significance of all three regimes in a wide range of temperature and sample width. Based on the relative contribution from each transport regime, we could clearly distinguish between the ballistic, hydrodynamic, and diffusive regimes, as well as the transition among these regimes. The characteristic of the transition between the ballistic and hydrodynamic regimes is shown through phonon Knudsen minimum.

The proposed decomposition framework would be useful to analyze the significance of all three regimes in high thermal conductivity materials.

5.0 Transient lattice cooling by propagation of second sound in graphite

Hydrodynamic features have been theoretically predicted and experimentally observed in graphite at temperatures around 100 K^{27,35}. Here, we show the evidence of second sound in graphite through our deviational MC simulation of the transient PBE. We report a clear propagation of second sound followed by significant lattice cooling that is not possible in ballistic or diffusive transport. Our simulation results are experimentally verified by a picosecond pump-probe thermalreflectance measurements. Such lattice cooling has not been reported in recent measurements but is consistence with both hydrodynamic transport theory and prior heat-pulse measurements of second sound in bulk sodium fluoride.

5.1 Background

Recently, the second sound was observed at temperatures above 100 K in a highly oriented pyrolytic graphite sample using a transient grating experiment³⁵. The measurement detected the diffraction signal from a thermal expansion grating and observed a shift of the peak thermal expansion. This is an unusual feature caused by the second sound. However, their measurements only suggest relative thermal expansion difference between different locations without detailed information of the actual temperature change. In addition, this experiment is different from the direct heat-pulse measurement that clearly showed the propagation of second sound and a possible lattice cooling effect³³.

Observing the transient propagation of second sound using the heat-pulse measurement is still meaningful as it provides the direct evidence and additional insights on second sound in graphite. The experimental measurement, however, is extremely difficult because prior knowledge of the dispersion and attenuation of second sound is needed. The requirement of strong wave signal and weak damping leads to the stringent conditions required for second sound to occur. On one hand, the inverse of the duration of the pulse that creates the thermal excitation should be smaller than U-scattering rates such that U-scattering is not able to significantly destroy the net momentum. The length of the sample should be much less than U-scattering MFP for minimum damping. On the other hand, the pulse should be frequent enough so that N-scattering is strong enough to form collective motion between phonons and phonons do not travel with their own group velocities. The sample should be long enough for the wave to complete at least one period.

5.2 Dispersion and attenuation of second sound

The speed, frequency, and wavelength of second sound can be derived from the momentum and energy balance equations from the PBE^{13,15,112}. Here we follow the same method to calculate the propagation and attenuation of second sound in graphite. We start with the transient PBE with Callaway's scattering model:

$$\frac{\partial f_i}{\partial t} + \mathbf{v}_i \cdot \nabla_{\mathbf{r}} f_i = -\frac{f_i - f_i^{\text{disp}}}{\tau_{i,N}} - \frac{f_i - f_i^0}{\tau_{i,U}}. \quad (5-1)$$

Multiplying the phonon momentum $\hbar q_{i,x}$ and energy $\hbar \omega_i$ on both sides of Eq. (5-1) and sum over all phonon states, we obtain

$$\frac{\partial \sum_i q_{i,x} f_i}{\partial t} + \sum_i q_{i,x} \mathbf{v}_i \cdot \nabla_{\mathbf{r}} f_i = \sum_i -q_{i,x} \frac{f_i - f_i^0}{\tau_{i,U}} \quad (5-2)$$

for momentum balance, and

$$\frac{\partial \sum_i \omega_i f_i}{\partial t} + \sum_i \omega_i \mathbf{v}_i \cdot \nabla_{\mathbf{r}} f_i = 0 \quad (5-3)$$

for energy balance. The right side of Eq. (5-2) does not contain the term due to N-scattering because the momentum is conserved upon N-scattering. The right side of Eq. (5-3) is zero because energy is always conserved upon scattering. Using the solution to Eq. (5-1) and assuming the plane wave for displacement and temperature fields, as described in detail in the previous study¹¹², the dispersion and relaxation length of second sound in graphite can be calculated, as shown in Figure 24(a) and (c).

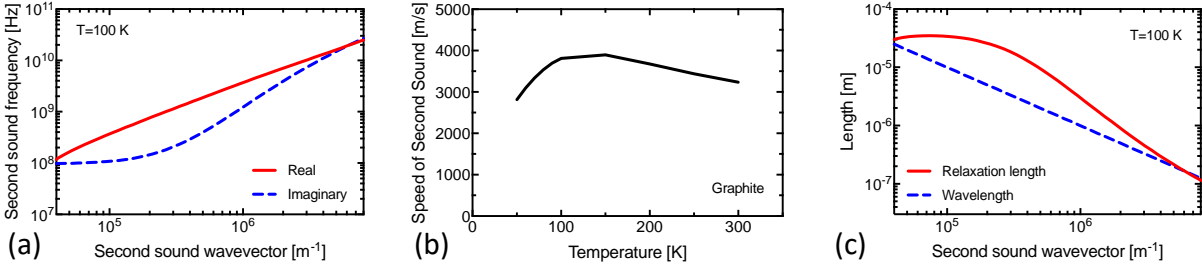


Figure 24 The propagation and attenuation of second sound in graphite at 100 K. (a) The dispersion relation of second sound. (b) Theoretical speed of second sound. (c) The relaxation length of second sound.

The real and imaginary frequencies in Figure 24(a) represent the dispersion and attenuation of a pulse, respectively. The imaginary frequency is caused by U-scattering and viscous damping effect and is the lower limit of second sound frequency. For the best condition for second sound to occur, the frequency should be chosen where there is the largest gap between real and imaginary frequencies. For example, as shown in Figure 24(a), second sound frequency of 1 GHz would be the optimal choice, corresponding to a pulse duration of 1 ns. Under this frequency, the wavevector

and wavelength of second sound are also determined. From the dispersion relation, the speed of second sound can be calculated, as shown in Figure 24(b) at different temperatures. The sample length should also be properly chosen to avoid significant damping of second sound. In Figure 24(c) we show the relaxation length as a function of second sound wavevector. The relaxation length is calculated based on the speed of second sound and the imaginary part of second sound frequency. For a given second sound wavevector, the sample length should lie between the wavelength and relaxation length to ensure the propagation of second sound and the minimum damping.

5.3 Monte Carlo simulation of second sound

To provide theoretical guidance and verification of the pico-second pump-probe thermal reflectance measurements, we perform our MC simulation of the propagation of second sound in bulk graphite. We solve the transient deviational PBE with a full scattering matrix with inputs of phonon dispersion and scattering matrix from first-principles calculations. Our MC simulations are performed under the same experimental setup and conditions, the details of which can be found in the recent study¹²².

5.3.1 Sample geometry and boundary conditions

The sample geometry and the boundary conditions are shown in Figure 25. The sample thickness was chosen to be 1 μm , which is much larger than the thermal penetration depth of 200 nm estimated from the heat diffusion equation. For the front, left, and top surfaces of the sample,

thermally adiabatic boundary condition was applied. The adiabatic surfaces reflect incoming phonons specularly, so only one quarter of the experimental setup is needed because of the symmetry in the in-plane transport. For the entire sample, the phonon distribution was initialized with the equilibrium Bose-Einstein distribution at a homogenous ambient temperature. The sample was discretized into $20 \times 20 \times 3$ control volumes in the real-space domain. The first Brillouin zone of reciprocal space was discretized with a $25 \times 25 \times 5$ grid. The time space was discretized with a time interval of 7, 5, and 3 ps at 80, 100, and 150 K, respectively.

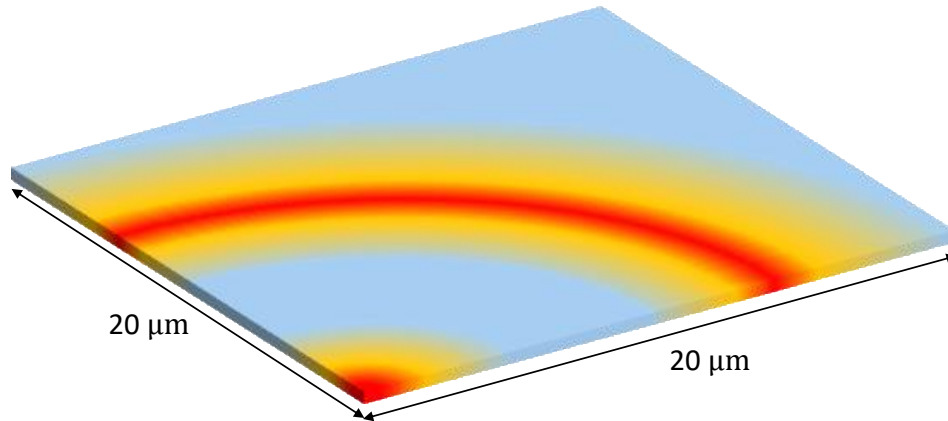


Figure 25 Schematic of a 3D graphite sample with thickness of $1 \mu\text{m}$ for the MC simulation. One quarter of the experimental setup is simulated, with adiabatic boundaries for the front, left, and top surfaces. The back, right, and bottom surfaces are at constant ambient temperature.

5.3.2 Simulation details

The first-principles calculations were performed using the Vienna Ab initio Simulation Package^{92,93,123}. We used the projector-augmented-wave pseudopotentials and local density approximation for exchange-correlation energy functional. The van der Waals interaction was included with a non-local correlation functional, optB88-vdW^{124,125}. The cutoff energy of the plane

wave basis is 520 eV. The crystal structure was relaxed with a $24 \times 24 \times 10$ grid for sampling electronic states (k points) in the first Brillouin zone. The second order force constants were calculated by density functional perturbation theory with $5 \times 5 \times 2$ supercells. The third order force constants were calculated by a real space supercell approach with $4 \times 4 \times 2$ supercells and $8 \times 8 \times 6$ grid of k points, with a cut-off distance to the fifth nearest neighbor. The phonopy¹²⁶ and thirdorder.py⁴ packages were also used in the calculations of second and third order force constants, respectively.

The heating by the pump laser which has a ring-shape was simulated by applying heat source to the control volumes for the time duration of actual laser (400 ps). The intensity of heat source follows the Gaussian distribution with the same full width at half maximum (FWHM) value as the pump beam used in the experiment (6 μm) along the in-plane direction. In the process of heating, phonons were generated following the equilibrium Bose-Einstein distribution at local temperature. The time-and-space-dependent phonon distribution function was calculated to sample the local temperature change. The temporal temperature change at the dot-shape probe beam was collected by averaging the local temperatures weighted by a Gaussian function with a FWHM of 6 μm , which is the same as the actual probe beam used in the experiment.

5.3.3 Comparison in different transport regimes

To validate our MC simulation and show the evidence of second sound, we first simulate the response of the system to the laser heating in ballistic, hydrodynamic, and diffusive regimes, as shown in Figure 26. The ballistic responses (blue lines) are obtained by the MC simulation without including internal phonon scattering, while the real cases with scattering are shown in red lines. For the diffusive responses (orange lines), we use the Ansys-Fluent package that solves the

2D heat conduction equation. One quarter of the ring-shape heating is simulated, and the temporal temperature response is collected at the center of the ring.

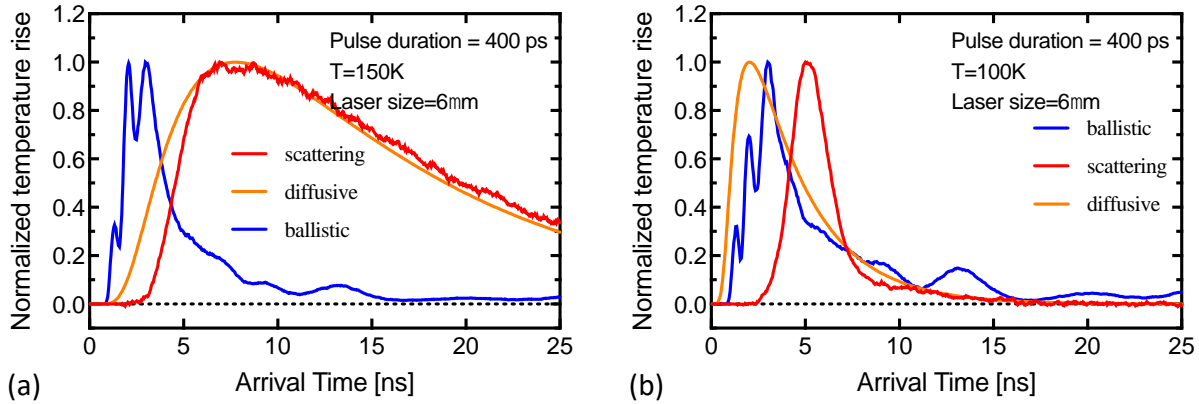


Figure 26 Temporal temperature responses in different transport regimes at 150 K (a) and 100 K (b).

At both temperatures, the ballistic responses show three clear peaks, corresponding to phonons with different branches due to the dispersive nature of phonon dispersion in graphite. The ballistic peaks are wide and have long tails because of phonons with small group velocities. The diffusive responses show the strong damping of the temperature pulse, featured by a slow decay of temperature with a very long tail. This is more significant at higher temperatures, as shown in Figure 26(a). At 150 K, U-scattering dominates and destroys any net momentum, and the transport is in diffusive regime. This can be seen by the excellent agreement between the temperature evolution from the MC simulation when internal phonon scattering is considered (red line) and the diffusive response (orange line). However, at 100 K, a single peak is observed with a well-defined width, different from either ballistic or diffusive signals, as shown in Figure 26(b). This single peak indicates the collective motion and is the direct evidence of the propagation of second sound.

5.4 Transient lattice cooling at adiabatic center

The propagation of second sound in a highly oriented pyrolytic graphite is recently experimentally observed using a picosecond transient thermoreflectance system¹²². In the experiment, a ring-shape pump laser is applied for a duration of 400 ps, and the temporal temperature response at the center of ring-shape pump laser is recorded by a dot-shape probe laser. The experimental observed thermoreflectance signals at different ambient temperatures are shown in Figure 27. Above 150 K, the thermoreflectance signal exhibits an ordinary thermal decay that is expected for diffusive phonon transport since the signal first arises to the peak and then relaxes to the ambient temperature. As the temperature is decreased to 120 K, a positive peak temperature rise is followed by a negative temperature peak. The negative peak becomes clear when the ambient temperature is decreased further to 80 K. The negative temperature peak suggests lattice cooling, which cannot occur in either ballistic or diffusive transport. In both ballistic and diffusive regimes, the pulse heating only increases the lattice temperature. In hydrodynamic regime when phonon momentum is conserved, the temperature field will fluctuate between positive and negative displacement, leading to the transient lattice cooling.

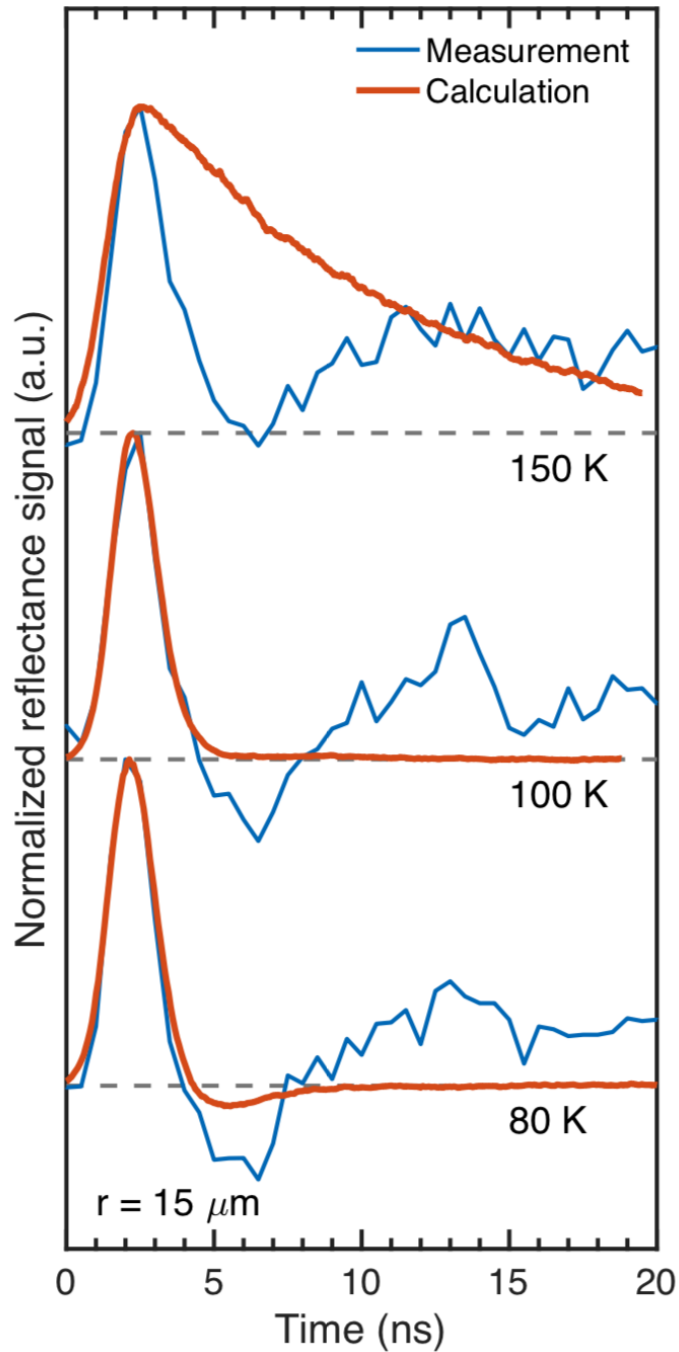


Figure 27 Second sound signal from experiments and simulations at 80, 100, and 150 K.

To better understand the experimental observation, we simulate the same experimental conditions as explained in section 5.3.2. The simulation results are also shown in Figure 27 as the

red lines. At 80 K, the negative temperature peak is also observed in the MC simulation, and qualitatively agrees with the experimental observation. The evolution of temperature profile at 80 K is plotted in Figure 28. As shown in Figure 28(a-b), the local temperature peak by the ring-shape heat pulse propagates toward the center within 2.1 ns after the heating. At 3.5 ns, the temperature peak merges at the center in Figure 28(c), and then propagates outward in Figure 28(d). The negative temperature peak occurs near the center following the outgoing positive peak as shown in Figure 28(e). The evolution of the temperature profile is summarized in Figure 28(f) to show the clear fluctuation of temperature field at the center upon the arrival and departure of the temperature peak.

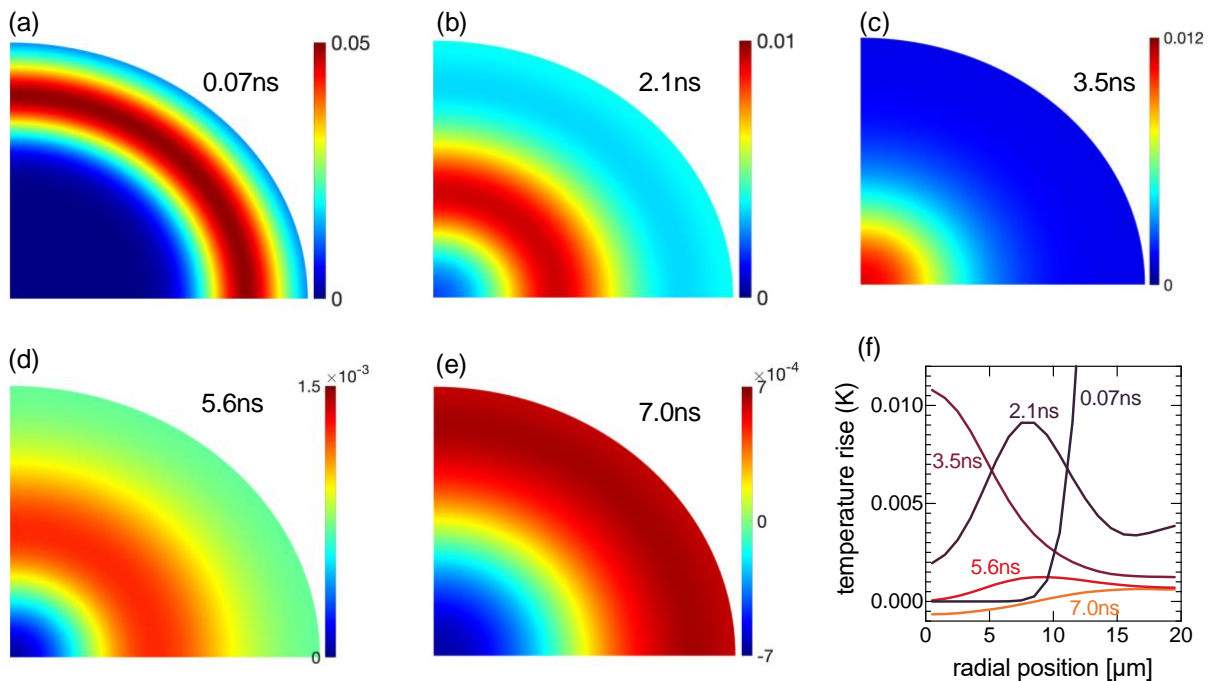


Figure 28 Snapshots of temperature profile on the top surface of the graphite sample at 80 K.

The experimental setup that has a ring-shape pump with a probe at the center is similar to that of the NaF measurement where the probe beam is located at the thermally adiabatic boundary³³. In our case, the center can be considered thermally adiabatic boundary due to the

symmetry. In the previous study on NaF and our current results, the negative temperature peak occurs after the second sound pulse is reflected by thermally adiabatic boundary. The thermally adiabatic boundary is an important condition for the lattice cooling to occur. In comparison, we simulate the offset measurement where the pump and probe beams are separated by a distance without any thermally adiabatic boundary. As shown in Figure 29, for different distances between pump and probe beams, the lattice cooling cannot be observed.

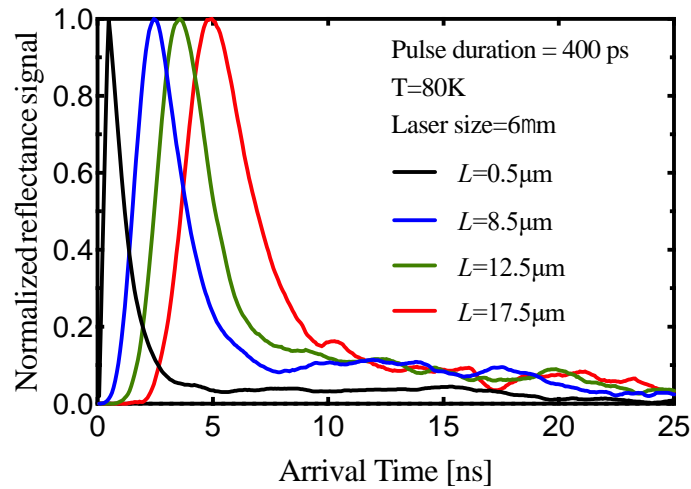


Figure 29 MC results of the offset measurement with different distances between the pump and probe beams.

5.5 Conclusion

The dispersion and attenuation of second sound in graphite is theoretically calculated. By solving the transient PBE with full scattering matrix using the deviational MC simulation, the propagation of second sound is clearly observed. The temperature response in second sound is different from the responses in ballistic regime where dispersive peaks occur and in diffusive regime where the peak slowly decays. Both our simulation and a picosecond thermoreflectance measurement reveal that the pulse heating can create lattice cooling near the adiabatic boundary.

In the hydrodynamic phonon transport regime in graphite, the heat source can propagate over a distance of several micrometers before being reflected by the adiabatic boundary, resulting in lattice cooling. Such lattice cooling has not been reported in recent measurements on graphite and provides more insights on phonon hydrodynamics in graphitic materials.

6.0 Significant interfacial resistance from the scattering of non-equilibrium phonons

In this Chapter, we turn our focus from hydrodynamic phonon transport to interfacial thermal resistance. We present our examination of phonon transport across an interface between silicon and germanium by solving the PBE with inputs from first principles. The phonon distribution is solved in both real and reciprocal spaces, and the local interfacial effects are well captured. By calculating local entropy generation, we find that internal phonon scattering among the phonons at non-equilibrium near the interface provides an important contribution to the overall interfacial resistance. The significant contribution from these non-equilibrium phonons may explain the widely reported difference in interfacial resistance between measurements and the Landauer theory in various systems. We also find that the effect of non-equilibrium is not only at the close proximity to the interface but can be extended to a distance way larger than the specific heat averaged phonon MFP, which suggests that the assumption of a single interface needs to be reconsidered when the system size is small.

6.1 Method for evaluating the non-equilibrium

The non-equilibrium has usually been observed through the temperature profile near the interface where local temperature becomes non-linear. The non-linear temperature profile has been mostly observed in MD simulations^{62,80–83}, but is also clearly shown by solving the PBE with RTA using *ab initio* inputs⁷⁷. In Figure 30, we present the temperature profile for a Si/Ge interface from

our deviational MC solution to the PBE with *ab initio* full scattering matrix. The non-linear temperature is significant on Ge side at all temperatures.

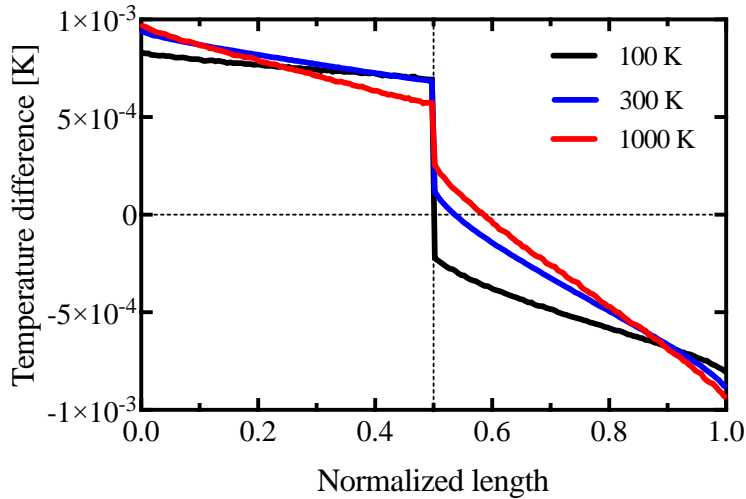


Figure 30 Temperature profiles for a Si/Ge system with length of 200 nm. The non-linear feature is clearly observed.

The temperature, however, is not a good measurement of non-equilibrium because it is not well-defined in this situation. The effective temperature calculated here only shows the total internal energy but does not give any information about phonon distribution function. Phonons can have different distribution functions while the local temperatures are the same. The non-equilibrium should be evaluated by looking directly at phonon distribution. Here we propose two methods to quantify the non-equilibrium: evaluating the symmetry of phonon distribution function and calculating local entropy generation.

6.1.1 Symmetry of phonon distribution function

Phonons follow bulk distribution as in Eq. (2-37) when internal scattering is frequent enough. The deviation of bulk distribution f_i^{bulk} from local equilibrium distribution f_i^0 is

$$f_i^{\text{bulk}} - f_i^0 = \mathbf{F}_i \frac{\partial f_i^0}{\partial T} (-\nabla_{\mathbf{x}} T) \quad (6-1)$$

with

$$\mathbf{F}_i = \tau_i (\mathbf{v}_i + \Delta_i) \quad (6-2)$$

where τ_i is the total scattering rate for phonon state i , $\tau_i \mathbf{v}_i$ is the phonon MFP under RTA, and Δ_i is the measure of deviation from the RTA solution with the dimension of velocity⁴. Considering heat transport along x direction, the deviation from local equilibrium should be symmetric for $+x$ and $-x$ directions because of the symmetry of phonon dispersion. Namely, we have

$$f_{i,v_{x,i}>0}^{\text{bulk}} - f_{i,v_{x,i}>0}^0 = - \left(f_{i,v_{x,i}<0}^{\text{bulk}} - f_{i,v_{x,i}<0}^0 \right). \quad (6-3)$$

This symmetry of deviation from local equilibrium is a characteristic of bulk phonon distribution. For phonons at non-equilibrium near the interface, their phonon states are randomly determined due to the nature of diffuse scattering upon transmission and reflection, and this symmetry cannot be satisfied. Thus, Eq. (6-3) can be used as a measure of non-equilibrium of the actual phonon distribution.

Directly calculating Eq. (6-3) on a modal basis using MC method, however, would introduce large stochastic error due to the limited number of phonon particles that are tracked. Instead, we calculate the total heat flux due to the deviation from local equilibrium for $+x$ and $-x$ directions separately. The heat flux representing the deviation of distribution from local equilibrium is calculated as

$$q_{x,\text{dev}}^+ = \frac{1}{NV_{\text{uc}}} \sum_{i,v_{x,i}>0} \hbar\omega_i v_{x,i} (f_{i,x} - f_{i,x}^0) \quad (6-4)$$

for $+x$ direction, and

$$q_{x,\text{dev}}^- = \frac{1}{NV_{\text{uc}}} \sum_{i,v_{x,i}<0} \hbar\omega_i v_{x,i} (f_{i,x} - f_{i,x}^0) \quad (6-5)$$

for $-x$ direction. Note that subscript x for f and q means the dependence on spatial position. The $q_{x,\text{dev}}^+$ and $q_{x,\text{dev}}^-$ are both positive and different from the conventional heat flux calculated based on actual phonon distribution, as shown in Figure 31 as solid lines.

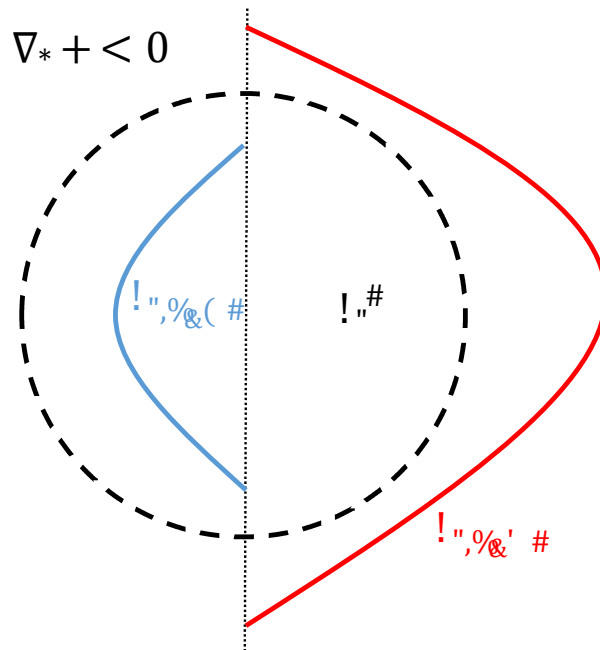


Figure 31 Schematic of heat flux of deviation of distribution from local equilibrium. The red/blue shaded area represents the heat flux along $+x$ / $-x$ direction. The red and blue lines represent the heat flux based on actual phonon distribution along $+x$ and $-x$ direction, respectively.

The dashed line represents the heat flux from local equilibrium distribution and is thus symmetric. The red ($q_{x,\text{dev}}^+$) and blue ($q_{x,\text{dev}}^-$) shaded area should be equal for bulk phonon

distribution. Adding $q_{x,\text{dev}}^+$ and $q_{x,\text{dev}}^-$ together will lead to the same net heat flux in the system because the heat flux from f_i^0 in two directions will be cancelled out. To define the similarity between the actual distribution and the bulk distribution, a parameter that evaluates $q_{x,\text{dev}}^+$ and $q_{x,\text{dev}}^-$ is calculated as

$$|\delta q_{\text{sym},x}| = \frac{|q_{x,\text{dev}}^+ - q_{x,\text{dev}}^-|}{q_{x,\text{dev}}^+ + q_{x,\text{dev}}^-} \quad (6-6)$$

and is a function of spatial position x . For every control volume in the spatial domain, $|\delta q_{\text{sym},x}|$ can be calculated based on local distribution functions. A large value of $|\delta q_{\text{sym},x}|$ indicates that the distribution is far away from the bulk one and at non-equilibrium, while a small value would suggest the bulk distribution.

6.1.2 Local entropy generation

As discussed in section 1.3.4.3, for phonons with bulk distribution, the entropy generation due to internal scattering is a constant, while for phonons at non-equilibrium near the interface, it will be increased because of additional interfacial scattering. Thus, calculating local entropy generation is a good measure of non-equilibrium. The rate of local entropy generation due to scattering is calculated as⁹⁹

$$\dot{S}_x = -\frac{1}{T_0 NV} \sum_i \phi_{i,x} \dot{f}_{i,x} \quad (6-7)$$

where subscript x denotes spatial position along heat transport direction, and $\phi_{i,x}$ is the measure of deviation of phonon distribution for phonon state i from local equilibrium defined as

$$f_{i,x} = f_{i,x}^0 - \phi_{i,x} \frac{\partial f_i^0}{\partial \hbar \omega_i}. \quad (6-8)$$

To evaluate \dot{S}_x in our MC simulation, we calculate $f_{i,x}$ from

$$f_{i,x} = \frac{e_{i,x}^d}{\hbar \omega_i} + f_i^{\text{eq}} \quad (6-9)$$

where $e_{j,x}^d$ is the local deviational energy distribution for phonon state j . The $\dot{f}_{i,x}$ is the rate of change of phonon distribution due to scattering, and can be calculated through full scattering matrix as

$$\dot{f}_{i,x} = \frac{1}{\hbar \omega_i} \sum_j B_{ij} e_{j,x}^d. \quad (6-10)$$

At steady-state, $e_{i,x}^d$ is extracted from MC simulation for each phonon state i and each control volume in the spatial domain, and local entropy generation rate can be calculated.

6.2 Effective interfacial region with strong non-equilibrium

We first quantify the non-equilibrium near the interface between Si and Ge by calculating $|\delta q_{\text{sym},x}|$ from Eq. (6-6), as shown in Figure 32. Near the interface, $|\delta q_{\text{sym},x}|$ is high for both Si and Ge, indicating significant non-equilibrium distribution. This is due to interfacial scattering, including transmission and reflection at the interface, that randomly alters the phonon distribution. Moving away from the interface, internal phonon scattering recovers the non-equilibrium distribution to the bulk distribution, and $|\delta q_{\text{sym},x}|$ decreases. On Si side, $|\delta q_{\text{sym},x}|$ decreases slower with distance from the interface than on Ge side, which is expected because phonons in Si

have larger MFPs than those in Ge, and a longer distance is needed for frequency internal phonon scattering.

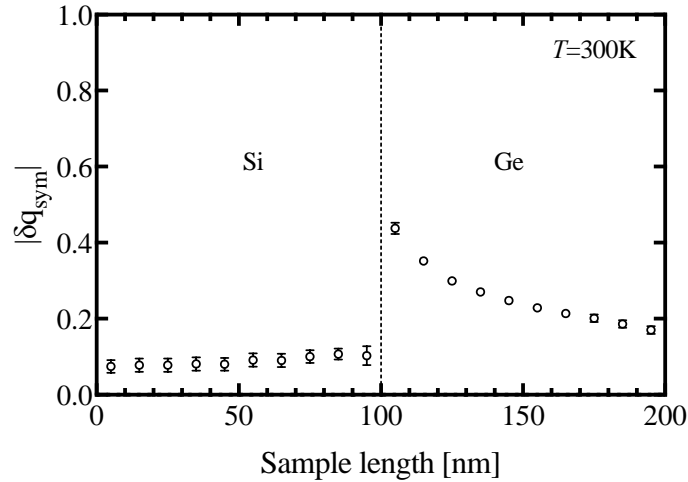


Figure 32 Evaluation of symmetry of deviation of phonon distribution from local equilibrium.

While $|\delta q_{\text{sym},x}|$ on Ge side decreases faster, the values are much larger than those on Si side. This is because the incoming heat flux from Ge is largely reflected by the interface. In Figure 33, we show the spectral heat flux together with transmissivity for both materials. The spectral heat flux is calculated assuming bulk phonon distribution. It is expected that the major heat flux comes from relatively low frequency acoustic phonons, but the transmissivity has drastic change for different frequencies. In Ge, phonons with frequency below 3 THz have generally low transmissivities, while those with frequency between 3 to 6 THz have large transmissivities. The difference in transmissivity comes from the relative phonon DOS between Si and Ge as seen in the DMM. Comparing Figure 33(b) and (d), it is clear to see that major heat carriers in Ge are not likely to transmit across the interface due to small transmissivity but have a high chance of being reflected back. The reflection changes a significant portion of $q_{x,\text{dev}}^-$ to $q_{x,\text{dev}}^+$, leading to a large asymmetry between them and thus large values of $|\delta q_{\text{sym},x}|$. On Si side, most heat carried by low

frequency phonons is transmitted across the interface, thus the ratio of $q_{x,\text{dev}}^-$ and $q_{x,\text{dev}}^+$ is not changed significantly, and $|\delta q_{\text{sym},x}|$ is small.

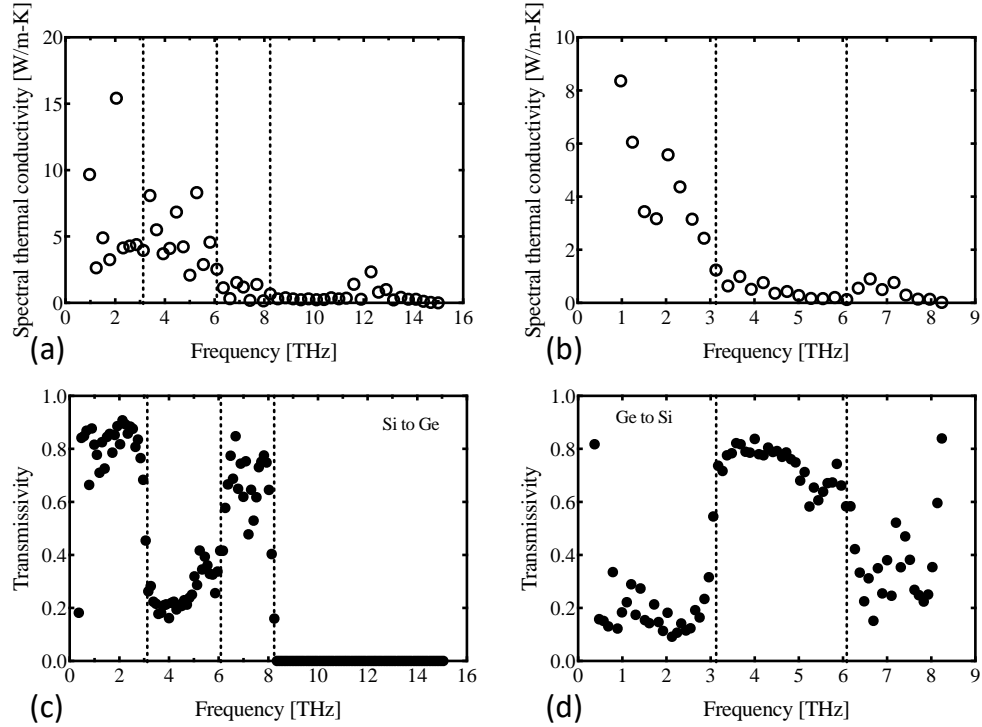


Figure 33 Spectral heat flux from bulk phonon distribution and transmissivity for Si (a,c) and Ge (b,d).

Dashed lines are for dividing different frequencies based on transmissivity.

The system size of 200 nm in Figure 32 is too small for the distribution to recover to bulk distribution at the boundaries. We also calculate $|\delta q_{\text{sym},x}|$ for larger systems as shown in Figure 34. As expected, the data at the same position for different lengths are on top of each other, which indicates that the local phonon distribution is the same, and that there is no size effect as the boundaries generate phonons with bulk distribution. Significant non-equilibrium near the interface is observed in both materials. The decay of the non-equilibrium effect with the distance from the interface is clear and shows that the non-equilibrium is limited within a certain range, which we

define as the effective interfacial region. To estimate the size of interfacial region, we first fit the data for the largest length in each material with an exponential function

$$|\delta q_{\text{sym},x}| = A \exp(Bx_{\text{int}}) + C \quad (6-11)$$

where x_{int} is not the position but the distance from the interface, A , B , and C are constants. We then define the edge of interfacial region as the position when $|\delta q_{\text{sym},x}|$ is decreased to 10% of the value at the interface, which indicates the non-equilibrium effect is negligible. As an estimation, the size of effective interfacial region is around 500 nm on Si side, and around 300 nm on Ge side.

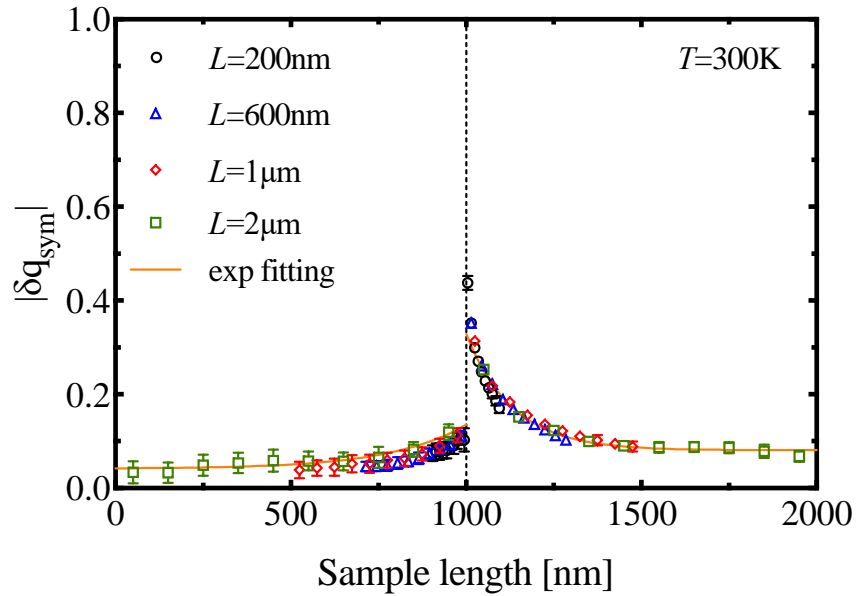


Figure 34 Quantification of non-equilibrium for systems with different lengths.

Highly non-equilibrium phonon distribution near the interface leads to large entropy generation upon internal phonon scattering. The local entropy generation rate calculated by Eq. (6-7) is shown in Figure 35. Near the boundaries, entropy generation rate is constant and agrees well with the entropy generation from bulk thermal conductivity when phonons follow bulk distribution, which will be called bulk entropy generation. Moving toward the interface, entropy

generation rate increases on both sides, and reaches the maximum near the interface. This increase indicates that there is additional resistance from internal phonon scattering. The additional resistance comes from phonons that are at non-equilibrium due to interfacial scattering. The non-equilibrium is most significant in close proximity to the interface, resulting in the largest local entropy generation rate. The position when local entropy generation rate is the same as the bulk entropy generation is similar to the size of effective interfacial region on each side, around several hundreds of nanometers. The same trend observed in both Figure 34 and Figure 35 validates our calculations and clearly shows significant non-equilibrium near the interface.

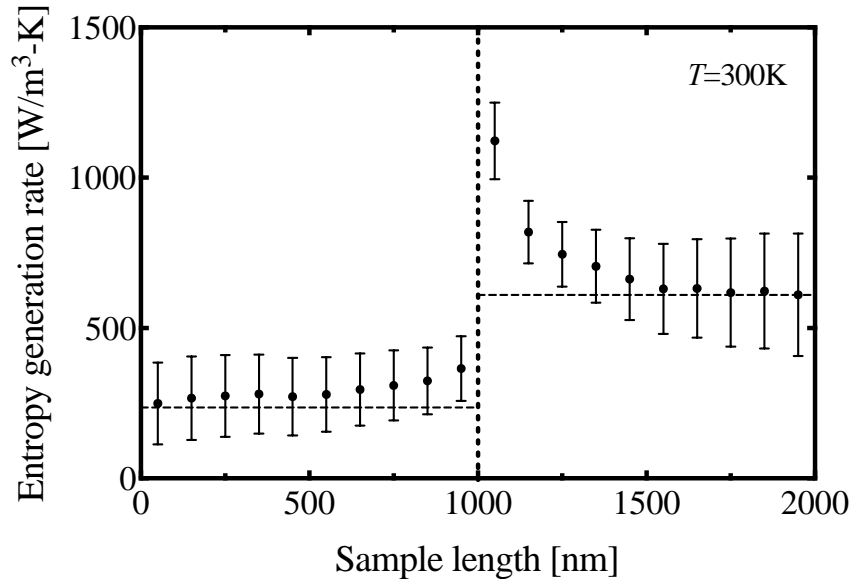


Figure 35 Local entropy generation rate. The horizontal dashed lines are bulk entropy generation values assuming internal phonon scattering with bulk distribution.

The effect of temperature on the non-equilibrium is also studied and summarized in Figure 36 and Figure 37. The $|\delta q_{\text{sym},x}|$ and local entropy generation rate in both figures show the same behaviors as the cases at 300 K, but the estimated size of effective interfacial region decreases at higher temperature due to stronger internal phonon scattering. The non-equilibrium is still

significant even at a high temperature like 1000 K, where the average phonon MFP is much smaller than the system size. This suggests that the average phonon MFP is not a good measure of the size of effective interfacial region.

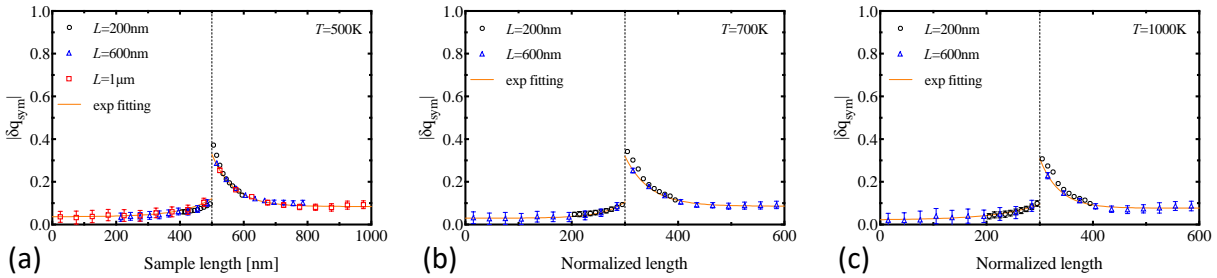


Figure 36 Quantification of non-equilibrium for systems with different lengths at (a) 500, (b) 700, and (c) 1000 K.

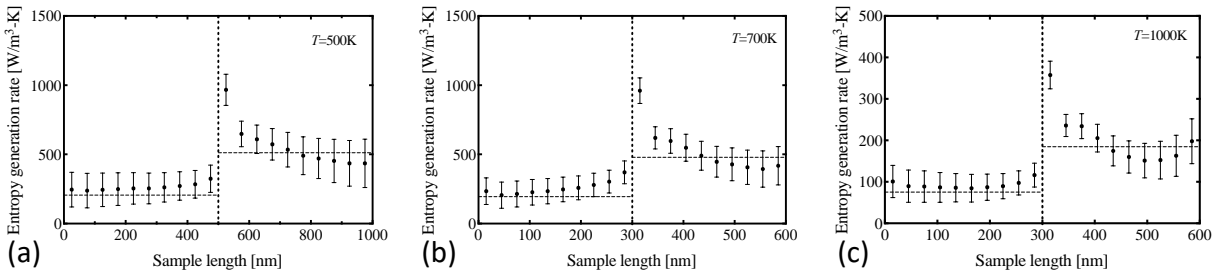


Figure 37 Local entropy generation rate at (a) 500, (b) 700, and (c) 1000 K.

To better understand the range of non-equilibrium, we calculate the accumulated thermal conductivity as a function of phonon MFP along the heat transport direction, as shown in Figure 38. The estimated size of effective interfacial region ranges from 200 to 500 nm for both Si and Ge at temperatures from 300 to 1000 K, which is larger than MFPs of phonons that contribute around 50% of total heat flow. These results demonstrate the importance of the interface when considering the size effect of the system. Usually the quasi-ballistic effect is the major concern

when determining the system size. However, here we show that even when internal phonon scattering is strong, there are also size effects brought by the interface due to the non-equilibrium.

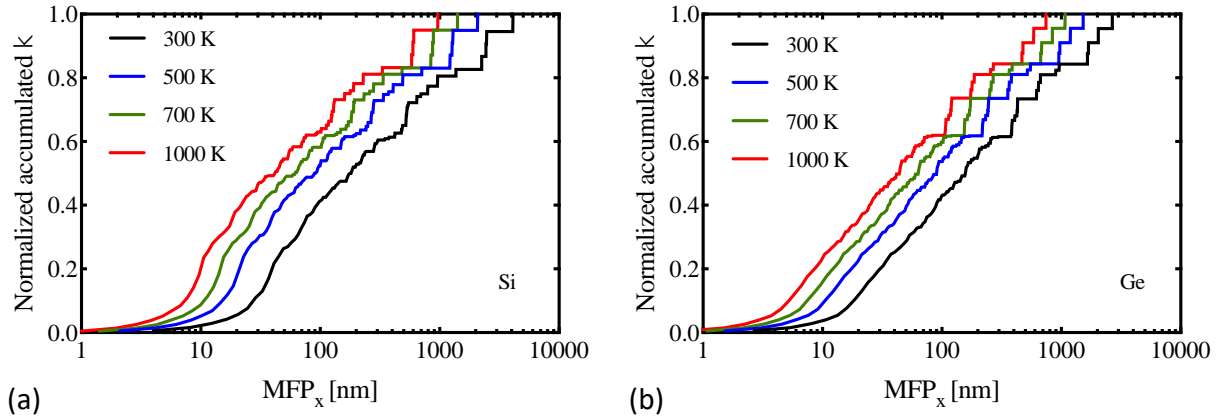


Figure 38 Accumulated thermal conductivity as a function of phonon MFP for (a) Si and (b) Ge at different temperatures.

6.3 Interfacial thermal resistance from MC

6.3.1 Total interfacial resistance assuming bulk thermal conductivity

Now we examine how the non-equilibrium near the interface affects the interfacial resistance. In Figure 39 we show the temperature profiles for different systems at 300, 500, 700, and 1000 K. The temperature drop at the interface is clearly observed in all cases. To calculate the temperature difference at the interface directly from the temperature profile in MC simulation is difficult because an accurate quantification of local temperature close to the interface needs lots of sampling points in the spatial domain. Also, the temperature itself is ill-defined with high non-equilibrium near the interface. Instead, we calculate the temperature drop based on the temperature profiles assuming bulk thermal conductivities in both materials, as the blue dashed lines shown in

Figure 39. These temperature profiles suggest diffusive phonon transport and are clearly different from the actual temperature profiles from the MC simulation near the interface. The deviation again indicates the non-equilibrium nature near the interface.

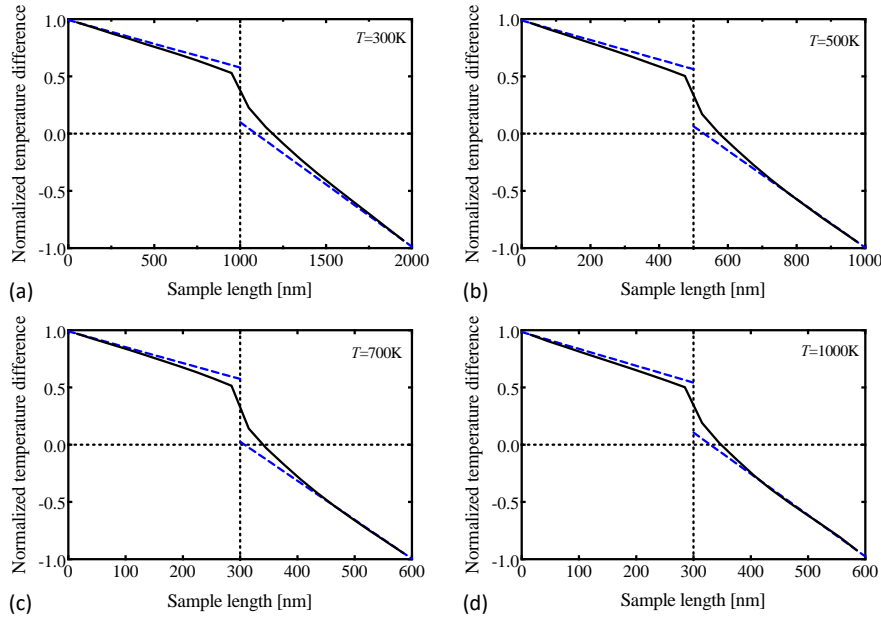


Figure 39 Temperature profiles for the Si/Ge interface from MC. The blue dashed lines are the temperature profiles with bulk thermal conductivities.

The calculated interfacial resistances based on the temperature profiles assuming bulk thermal conductivity is denoted as $R_{\kappa_{\text{bulk}}}$ and shown in Figure 40 as the red circles. The interfacial resistances remain constant at different temperatures. Calculating the interfacial resistance assuming the bulk thermal conductivity is similar to the method in experiments where bulk thermal conductivities are used for the fitting process^{5,40,42,44}. Nevertheless, it is much more complicated in the experimental measurements when all the imperfections at the interface are included.

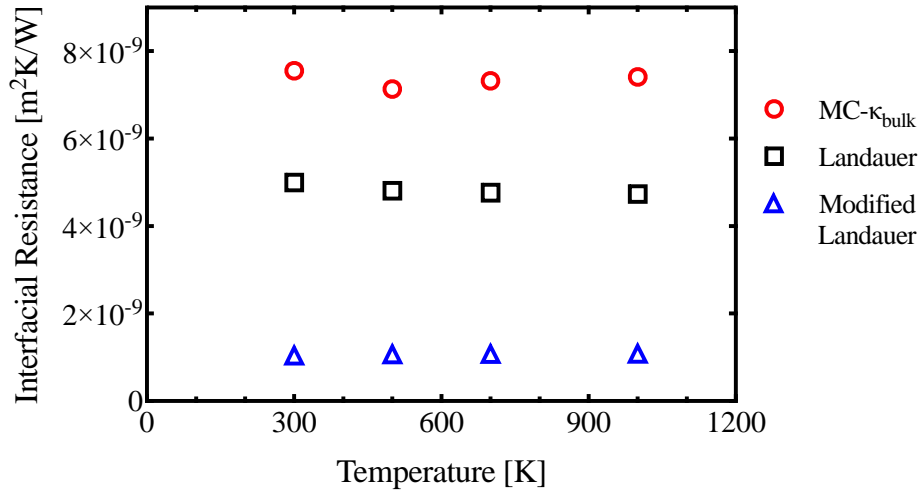


Figure 40 Interfacial thermal resistance from Landauer, modified Landauer, and MC.

We compare $R_{\kappa_{\text{bulk}}}$ with the predictions from the original Landauer formula and its modified version, as described in sections 1.3.3.1 and 1.3.3.2. The large difference between Landauer formula and its modified version comes from the fact that bulk distribution leads to a larger heat flux than that of equilibrium distribution under the same temperature difference, and has been reported in previous studies^{47,49,50}. The bulk distribution is the result of internal phonon scattering which has been shown to largely reduce interfacial resistance⁷⁷. The scattering among high frequency and low frequency phonons provides channels for high frequency phonons in Si to cross the interface which otherwise is impossible under the assumption of elastic interfacial scattering. However, when phonon distribution deviates from the bulk distribution, the interfacial resistance is significantly increased by the non-equilibrium. In Figure 40, $R_{\kappa_{\text{bulk}}}$ is even larger than the resistance predicted by the original Landauer formula. The fact that Landauer formula leads to a much different interfacial resistance has been reported by many experimental studies, as discussed in section 1.3.4.1. The real atomistic structure at the interface in experiments may increase the interfacial resistance and make it harder to explain by a simple theory, but our MC

simulation uses the same assumption of perfect crystalline structure and the transmissivity provided by the DMM. Thus, the large discrepancy between $R_{\kappa_{\text{bulk}}}$ and the Landauer prediction suggests the insufficiency of the theory, and that there are mechanisms at the interface not being described by the current theory.

6.3.2 Significant contribution from non-equilibrium phonons

To explain the large difference between $R_{\kappa_{\text{bulk}}}$ and Landauer prediction, we decompose the total interfacial resistance into the direct resistance at the interface and the resistance caused by internal phonon scattering. The resistance from internal phonon scattering with bulk distribution is reflected as the temperature gradient within the material and is already excluded from $R_{\kappa_{\text{bulk}}}$ which is calculated based on the temperature profile that is extrapolated to the interface using bulk thermal conductivity and heat flux. Thus, $R_{\kappa_{\text{bulk}}}$ can be decomposed as

$$R_{\kappa_{\text{bulk}}} = R_{\text{int}} + R_{\text{neq}} \quad (6-12)$$

where R_{int} is the resistance directly at the interface and R_{neq} is the resistance from internal phonon scattering with non-equilibrium distribution. Since R_{neq} cannot be calculated from the temperature profile, we turn to the local entropy generation rate in Figure 35. As Eq. (1-17) in section 1.3.4.3 shows, the entropy generation is directly related to thermal resistance. While the area under the bulk entropy generation (horizontal dashed lines) suggests the resistance from bulk distribution, R_{neq} can be calculated from the area between the actual entropy generation rate (symbols) and the bulk values. The resistance at the interface, R_{int} , is then obtained from Eq. (6-12).

The values of R_{int} and R_{neq} at different temperatures are shown in Figure 41, with R_{neq} contributed from both Si and Ge. Surprisingly, R_{neq} is comparable to R_{int} and has significant

contribution (around 50%) to the total interfacial resistance. This contribution from non-equilibrium phonons has been ignored in Landauer theory and has not been quantified before. In Figure 41, we show that by adding it to the resistance at the interface, the overall interfacial resistance is 1.5 times larger than that predicted from original Landauer theory. The non-equilibrium contribution explains the gap between Landauer theory and experiments, and the total interfacial resistance matches better with experimental measurements.

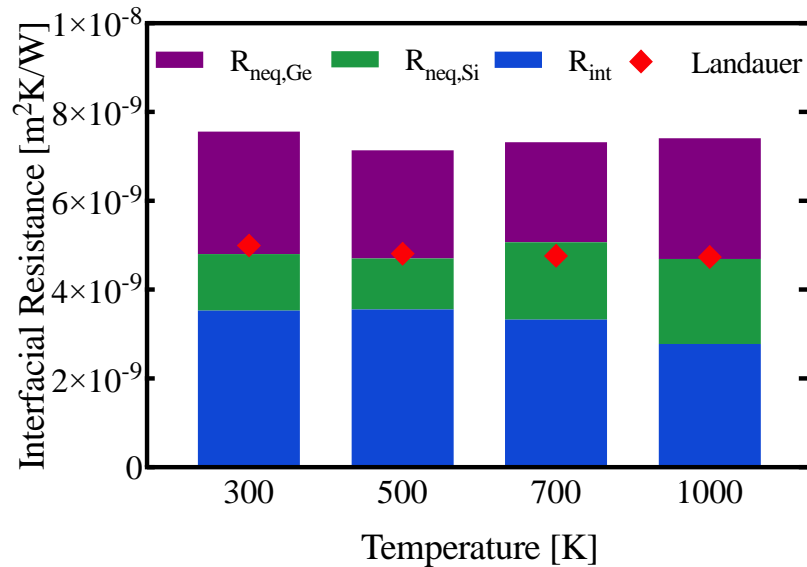


Figure 41 Decomposition of total interfacial resistance from MC. The contribution from non-equilibrium phonons is significant.

6.4 Conclusions

The phonon transport across a Si/Ge interface is studied by solving the PBE with the deviational MC method. The Landauer formula and its modified version are examined. These theories fail to capture the non-equilibrium near the interface due to interfacial scattering. The contribution of non-equilibrium phonons is quantified by calculating local entropy generation. We

find that this contribution is surprisingly significant and can explain the large discrepancy between the Landauer theory and experiments. By quantifying the non-equilibrium, we find that the effect of complex interplay between interfacial scattering and internal phonon scattering can be quite far from the interface. Our studies provide insights on interpreting experimental measurements and emphasize the influence of interface on phonon transport when the system size is small.

7.0 Summary and future directions

7.1 Summary

In this dissertation, using a deviational MC method to solve the PBE with *ab initio* full scattering matrix, we simulate the phonon transport in all seven dimensions (three in reciprocal space domain, three in real space domain, and one in time domain) without any empirical parameter. We have provided a better understanding of the fundamental physics of phonon transport in bulk graphitic materials and across a thermal interface between semiconductors.

Chapters 3 to chapter 5 discussed different transport phenomena of the hydrodynamic phonon transport in suspended graphene and graphite. Chapter 3 studied the peculiar temperature and sample width dependences of thermal conductivity in suspended graphene, a characteristic of phonon Poiseuille flow. We showed that thermal conductivity increases with temperature much faster than that of the ballistic case. The thermal conductivity has a superlinear width dependence at 100 K, clearly distinguished from the sublinear dependence of the ballistic-diffusive regime. These peculiar features were explained with a phonon viscous damping effect of the hydrodynamic regime. Our findings provided important guidance on experimental measurements and insights into detailed mechanisms in phonon hydrodynamics.

Chapter 4 proposed a framework to quantify the contribution of each phonon transport regime in real cases where the features of all three regimes exist to some extent. We assessed the extent of three regimes by comparing momentum destruction rates by three different mechanisms, each of which represents a different regime: diffuse boundary scattering without internal phonon scattering (ballistic regime), diffuse boundary scattering combined with normal

scattering (hydrodynamic regime), and umklapp scattering (diffusive regime). This framework helps us identify the major transport characteristics when transport phenomena are complex. We also discussed phonon Knudsen minimum, a unique phenomenon of ballistic-to-hydrodynamic crossover.

Chapter 5 presented another characteristic of hydrodynamic phonon transport, which is the propagation of second sound, in bulk graphite. The dispersion and attenuation of second sound were theoretically calculated from wave equations, and the optimal conditions for the propagation of second sound were determined. We simulated the heat-pulse measurement for a 3D crystalline graphite using our MC simulations and observed strong signal of second sound propagation that is clearly different from ballistic and diffusive transport. The evidence of direct propagation of second sound has been shown in solids at cryogenic temperatures but has never been experimentally verified at elevated temperatures. In our simulation, transient lattice cooling was observed in graphite for the first time and confirmed by experimental measurements using a picosecond transient thermoreflectance system. These findings provided important evidence on hydrodynamic transport in graphitic materials.

In chapter 6, the Landauer theory for phonon transport across an interface between silicon and germanium was examined. We showed that both the Landauer formula and its modified version underestimate interfacial resistance due to the fact that they ignore a strong non-equilibrium distribution near the interface. We quantified the non-equilibrium by evaluating the symmetry of phonon distribution and calculating local entropy generation rate. We defined an effective interfacial region, beyond which the non-equilibrium distribution recovers to the bulk phonon distribution. The internal phonon scattering within the interfacial region provided an important contribution to the overall interfacial resistance. Our study revealed the disadvantages

of Landauer theory and could help explain the large discrepancies between experimentally measured interfacial resistances and those calculated from the Landauer formula, thus providing a useful way to interpret experimental data.

7.2 Future directions

The dominance of hydrodynamic phonon transport in graphitic materials suggests a new way for thermal design and manipulation of heat flow in nanodevices with these materials. Yet the difficulty in fabricating high quality samples of suspended graphene or bulk graphite without surface contamination hinders the application of phonon hydrodynamics. Recently, hydrodynamic regime has been observed in other three-dimensional materials like strontium titanate¹¹⁰ and bulk black phosphorus¹¹¹, but at low temperatures with a small temperature window. The recent discoveries of the ultrahigh thermal conductivity in boron arsenide^{127–129} and boron nitride¹³⁰ suggest the possibility of hydrodynamic regime in these materials. Exploring new materials in which hydrodynamic phonon transport can occur is still very important for both fundamental understanding and thermal applications, especially in bulk materials at high temperatures.

The capability of our MC solver for the time and space dependent PBE with *ab initio* full scattering matrix makes it suitable to simulate non-diffusive phonon transport in samples with any dimension and any geometry. This is very useful for simulating and explaining experimental measurements in small time and length scales. For heat transport with varying temperature field in time and space, for example, transient and spatial heating in thermoreflectance measurements, phonon distribution in all seven dimensions is needed to accurately describe the transport process. This is impossible in traditional macroscopic solution of heat conduction, and hard to achieve for

other methods that solve the PBE without simplifying the scattering term. Thus, our MC simulation, with such power, can be used to solve these problems.

Another interesting direction is to study the effect of N-scattering on interfacial transport. Internal phonon scattering has been shown to be important for a Si/Ge interface by providing additional channels for high frequency phonons in Si side to transfer energy to low frequency phonons and then cross the interface. The internal phonon scattering in the system, however, is mainly U-scattering as N-scattering is very weak. It is known that N-scattering does not directly cause thermal resistance but can redistribute phonons. When combined with interfacial scattering, the redistribution by N-scattering may affect phonon transport across the interface. Such effect can be studied in the interface between silicon and diamond where N-scattering is significant.

Our current MC simulation is only for phonon transport, but the method can be extended to include electron transport because they are both governed by Boltzmann equations. While the simulation of electron transport in metals may be less of interest, the thermal transport across a metal/semiconductor interface is pretty important because such interface exists widely in thermoreflectance measurements. An accurate solution to Boltzmann equation would provide insights into the mechanisms of the transport process and help with the thermal design of the interface.

Bibliography

1. Broido, D. A., Malorny, M., Birner, G., Mingo, N. & Stewart, D. A. Intrinsic lattice thermal conductivity of semiconductors from first principles. *Appl. Phys. Lett.* **91**, 23–25 (2007).
2. Ward, A., Broido, D. A., Stewart, D. A. & Deinzer, G. Ab initio theory of the lattice thermal conductivity in diamond. *Phys. Rev. B* **80**, 125203 (2009).
3. Lindsay, L., Broido, D. A. & Mingo, N. Lattice thermal conductivity of single-walled carbon nanotubes: Beyond the relaxation time approximation and phonon-phonon scattering selection rules. *Phys. Rev. B* **80**, 125407 (2009).
4. Li, W., Carrete, J., Katcho, N. A. & Mingo, N. ShengBTE: A solver of the Boltzmann transport equation for phonons. *Comput. Phys. Commun.* **185**, 1747–1758 (2014).
5. Cahill, D. G. Analysis of heat flow in layered structures for time-domain thermoreflectance. *Rev. Sci. Instrum.* **75**, 5119–5122 (2004).
6. Schmidt, A. J., Cheaito, R. & Chiesa, M. A frequency-domain thermoreflectance method for the characterization of thermal properties. *Rev. Sci. Instrum.* **80**, (2009).
7. Cahill, D. G. *et al.* Nanoscale thermal transport. II. 2003-2012. *Appl. Phys. Rev.* **1**, (2014).
8. Chen, G. *Nanoscale energy transport and conversion: a parallel treatment of electrons, molecules, phonons, and photons.* (Oxford university press, New York, 2005).
9. Liao, B. *Nanoscale Energy Transport.* IOP Publishing (2020). doi:10.1201/9780367333003-4
10. Lindsay, L., Hua, C., Ruan, X. L. & Lee, S. Survey of ab initio phonon thermal transport. *Mater. Today Phys.* **7**, 106–120 (2018).
11. Balandin, A. A. *et al.* Superior Thermal Conductivity of Single-Layer Graphene 2008. *Nano Lett.* **8**, 902–907 (2008).
12. Seol, J. H. *et al.* Two-Dimensional Phonon Transport in Supported Graphene. *Science* **328**, 213–6 (2010).
13. Lee, S., Broido, D., Esfarjani, K. & Chen, G. Hydrodynamic phonon transport in suspended graphene. *Nat. Commun.* **6**, 6290 (2015).
14. Cepellotti, A. *et al.* Phonon hydrodynamics in two-dimensional materials. *Nat. Commun.* **6**, 6400 (2015).

15. Lee, S. & Li, X. Hydrodynamic phonon transport: past, present, and prospects. in *Nanoscale Energy Transport: Emerging phenomena, methods and applications* 1–26 (Institute of Physics Publishing, 2020).
16. Li, X. & Lee, S. Crossover of ballistic, hydrodynamic, and diffusive phonon transport in suspended graphene. *Phys. Rev. B* **99**, 85202 (2019).
17. Krumhansl, J. A. Thermal conductivity of insulating crystals in the presence of normal processes. *Proc. Phys. Soc.* **85**, 921 (1965).
18. Guyer, R. A. & Krumhansl, J. A. Solution of the Linearized Phonon Boltzmann Equation. *Phys. Rev.* **148**, 766–778 (1966).
19. Guyer, R. A. & Krumhansl, J. A. Thermal conductivity, second sound, and phonon hydrodynamic phenomena in nonmetallic crystals. *Phys. Rev.* **148**, 778–788 (1966).
20. Mezhev-Deglin, L. P. Measurement of the thermal conductivity of crystalline He4. *J. Exp. Theor. Phys.* **22**, 47 (1966).
21. Ackerman, C. C., Bertman, B., Fairbank, H. A. & Guyer, R. A. Second sound in solid helium. *Phys. Rev. Lett.* **16**, 789–791 (1966).
22. McNelly, T. F. *et al.* Heat pulses in NaF: Onset of second sound. *Phys. Rev. Lett.* **24**, 100–102 (1970).
23. Ashcroft, N. & Mermin, N. *Solid State Physics*. (Saunders college, 1976).
24. Gurzhi, R. N. Thermal conductivity of dielectrics and ferroelectrics at low temperatures. *J. Exp. Theor. Phys.* **46**, 719–724 (1964).
25. Majee, A. K. & Aksamija, Z. Length divergence of the lattice thermal conductivity in suspended graphene nanoribbons. *Phys. Rev. B* **93**, 235423 (2016).
26. Guo, Y. & Wang, M. Heat transport in two-dimensional materials by directly solving the phonon Boltzmann equation under Callaway’s dual relaxation model. *Phys. Rev. B* **96**, 134312 (2017).
27. Ding, Z. *et al.* Phonon Hydrodynamic Heat Conduction and Knudsen Minimum in Graphite. *Nano Lett.* **18**, 638–649 (2018).
28. Callaway, J. Model for lattice Thermal Conductivity at Low Temperatures. *Phys. Rev.* **113**, 1046–1051 (1959).
29. Allen, P. B. Improved Callaway model for lattice thermal conductivity. *Phys. Rev. B* **88**, 144302 (2013).

30. Morelli, D. T., Heremans, J. P. & Slack, G. A. Estimation of the isotope effect on the lattice thermal conductivity of group IV and group III-V semiconductors. *Phys. Rev. B* **66**, 195304 (2002).
31. Slack, G. A. & Galginaitis, S. Thermal conductivity and phonon scattering by magnetic impurities in CdTe. *Phys. Rev.* **133**, (1964).
32. Ackerman, C. C. & Overton, W. C. J. Second sound in solid helium-3. *Phys. Rev. Lett.* **22**, (1969).
33. Jackson, H. Second sound in NaF. *Phys. Rev. Lett.* **25**, (1970).
34. Narayanamurti, V. & Dynes, R. C. Observation of second sound in bismuth. *Phys. Rev. Lett.* **28**, 1461–1465 (1972).
35. Huberman, S. *et al.* Observation of second sound in graphite at temperatures above 100 K. **3548**, 1–10 (2019).
36. Giri, A. & Hopkins, P. E. A Review of Experimental and Computational Advances in Thermal Boundary Conductance and Nanoscale Thermal Transport across Solid Interfaces. *Adv. Funct. Mater.* **30**, 1–21 (2020).
37. KAPITZA, P. L. The Study of Heat Transfer in Helium II. *J. Phys.* **4**, (1941).
38. Monachon, C., Weber, L. & Dames, C. Thermal Boundary Conductance: A Materials Science Perspective. *Annu. Rev. Mater. Res.* **46**, 433–463 (2016).
39. Schmidt, A. J. Pump-probe thermoreflectance. *Annu. Rev. heat Transf.* **16**, 159–181 (2013).
40. Costescu, R. M., Wall, M. A. & Cahill, D. G. Thermal conductance of epitaxial interfaces. *Phys. Rev. B* **67**, 54302 (2003).
41. Jonathan A Malen, Kanhayalal Baheti, Tao Tong, Yang Zhao, Janice A Hudgings, A. M. Optical measurement of thermal conductivity using fiber aligned frequency domain thermoreflectance. *J. Heat Transfer* **133**, 081601 (2011).
42. Gundrum, B. C., Cahill, D. G. & Averback, R. S. Thermal conductance of metal-metal interfaces. *Phys. Rev. B* **72**, 245426 (2005).
43. Aller, H. T. *et al.* Chemical Reactions Impede Thermal Transport Across Metal/ β -Ga₂O₃ Interfaces. *Nano Lett.* **19**, 8533–8538 (2019).
44. Cahill, D. G., Bullen, A. & Lee, S. M. Interface thermal conductance and the thermal conductivity of multilayer thin films. *High Temp. - High Press.* **32**, 135–142 (2000).
45. Landauer, R. Electrical resistance of disordered one-dimensional lattice. *Philos. Mag.* **21**, 863–867 (1970).

46. Swartz, E. T. & Pohl, R. O. Thermal boundary resistance. *Rev. Mod. Phys.* **61**, 605–668 (1989).
47. Landry, E. S. & McGaughey, A. J. H. Thermal boundary resistance predictions from molecular dynamics simulations and theoretical calculations. *Phys. Rev. B* **80**, 1–11 (2009).
48. Cahill, D. G. Thermal conductivity measurement from 30 to 750 K: the 3ω method. *Rev. Sci. Instrum.* **61**, 802–808 (1990).
49. Merabia, S. & Termentzidis, K. Thermal conductance at the interface between crystals using equilibrium and nonequilibrium molecular dynamics. *Phys. Rev. B* **86**, (2012).
50. Simons, S. On the thermal contact resistance between insulators. *J. Phys. C Solid State Phys.* **7**, 4048–4052 (1974).
51. Chen, G. Diffusion-transmission interface condition for electron and phonon transport. *Appl. Phys. Lett.* **82**, 991–993 (2003).
52. Little, W. A. The transport of heat between dissimilar solids at low temperatures. *Can. J. Phys.* **37**, (1959).
53. Cheaito, R. *et al.* Thermal boundary conductance accumulation and interfacial phonon transmission: Measurements and theory. *Phys. Rev. B* **91**, 35432 (2015).
54. Dechaumphai, E. *et al.* Ultralow Thermal Conductivity of Multilayers with Highly Dissimilar Debye Temperatures. *Nano Lett.* **14**, 2448–2455 (2014).
55. Hua, C., Chen, X., Ravichandran, N. K. & Minnich, A. J. Experimental metrology to obtain thermal phonon transmission coefficients at solid interfaces. *Phys. Rev. B* **95**, 1–21 (2017).
56. Gaskins, J. T. *et al.* Thermal boundary conductance across heteroepitaxial ZnO/GaN interfaces: Assessment of the phonon gas model. *Nano Lett.* **18**, 7469–7477 (2018).
57. Cahill, D. G. *et al.* Nanoscale thermal transport. *J. Appl. Phys.* **93**, 793–818 (2003).
58. Hopkins, P. Thermal transport across solid interfaces with nanoscale imperfections: effects of roughness, disorder, dislocations, and bonding on thermal boundary conductance. *Int. Sch. Res. Not.* **2013**, 682586 (2013).
59. Ye, N. *et al.* Thermal transport across metal silicide-silicon interfaces: An experimental comparison between epitaxial and nonepitaxial interfaces. *Phys. Rev. B* **95**, 85430 (2017).
60. Gordiz, K. & Henry, A. Phonon transport at interfaces: Determining the correct modes of vibration. *J. Appl. Phys.* **119**, (2016).
61. Gordiz, K. & Henry, A. Phonon transport at crystalline Si/Ge interfaces: The role of interfacial modes of vibration. *Sci. Rep.* **6**, 1–9 (2016).

62. Feng, T., Zhong, Y., Shi, J. & Ruan, X. Unexpected high inelastic phonon transport across solid-solid interface: Modal nonequilibrium molecular dynamics simulations and Landauer analysis. *Phys. Rev. B* **99**, 1–13 (2019).
63. Mingo, N. & Yang, L. Phonon transport in nanowires coated with an amorphous material: An atomistic Green's function approach. *Phys. Rev. B* **68**, 245406 (2003).
64. Mingo, N. & Yang, L. Erratum: Phonon transport in nanowires coated with an amorphous material: An atomistic Green's function approach [Phys. Rev. B 68, 245406 (2003)]. *Phys. Rev. B* **70**, 249901 (2004).
65. Tian, Z., Esfarjani, K. & Chen, G. Enhancing phonon transmission across a Si/Ge interface by atomic roughness: First-principles study with the Green's function method. *Phys. Rev. B* **86**, 235304 (2012).
66. Dai, J. & Tian, Z. Rigorous formalism of anharmonic atomistic Green's function for three-dimensional interfaces. *Phys. Rev. B* **101**, 041301 (2020).
67. Norris, P. M. *et al.* On the Assumption of Detailed Balance in Prediction of Diffusive Transmission Probability During Interfacial Transport. *Nanoscale Microscale Thermophys. Eng.* **14**, 21–33 (2010).
68. Hopkins, P. E., Duda, J. C. & Norris, P. M. Anharmonic Phonon Interactions at Interfaces and Contributions to Thermal Boundary Conductance. *J. Heat Transfer* **133**, 062401 (2011).
69. Stevens, R., Zhigilei, L. & Norris, P. Effects of temperature and disorder on thermal boundary conductance at solid–solid interfaces: Nonequilibrium molecular dynamics simulations. *Int. J. Heat Mass Transf.* **50**, 3977–3989 (2007).
70. Hopkins, P., Norris, P. & Stevens, R. Influence of Inelastic Scattering at Metal-Dielectric Interfaces. *J. Heat Transfer* **130**, 022401 (2008).
71. Lyeo, H.-K. & Cahill, D. Thermal conductance of interfaces between highly dissimilar materials. *Phys. Rev. B* **73**, 144301 (2006).
72. Wu, X. & Luo, T. The importance of anharmonicity in thermal transport across solid-solid interfaces. *J. Appl. Phys.* **115**, 14901 (2014).
73. Murakami, T., Hori, T., Shiga, T. & Shiomi, J. Probing and tuning inelastic phonon conductance across finite-thickness interface. *Appl. Phys. Express* **7**, 121801 (2014).
74. Cheng, Z. *et al.* Thermal conductance across harmonic-matched epitaxial Al-sapphire heterointerfaces. *Commun. Phys.* **3**, 1–8 (2020).
75. Sääskilahti, K., Oksanen, J., Tulkki, J. & Volz, S. Role of anharmonic phonon scattering in the spectrally decomposed thermal conductance at planar interfaces. *Phys. Rev. B* **90**, 134312 (2014).

76. Le, N. Q. *et al.* Effects of bulk and interfacial anharmonicity on thermal conductance at solid/solid interfaces. *Phys. Rev. B* **95**, 1–8 (2017).
77. Maassen, J. & Askarpour, V. Phonon transport across a Si-Ge interface: The role of inelastic bulk scattering. *APL Mater.* **7**, (2019).
78. Singh, D., Murthy, J. Y. & Fisher, T. S. Effect of phonon dispersion on thermal conduction across Si/Ge interfaces. *J. Heat Transfer* **133**, 122401 (2011).
79. Varnavides, G., Jermyn, A. S., Anikeeva, P. & Narang, P. Nonequilibrium phonon transport across nanoscale interfaces. *Phys. Rev. B* **100**, 1–9 (2019).
80. An, M. *et al.* Generalized Two-Temperature Model for Coupled Phonons in Nanosized Graphene. *Nano Lett.* **17**, 5805–5810 (2017).
81. Feng, T. *et al.* Spectral analysis of nonequilibrium molecular dynamics: Spectral phonon temperature and local nonequilibrium in thin films and across interfaces. *Phys. Rev. B* **95**, 195202 (2017).
82. Lu, Z., Shi, J. & Ruan, X. Role of phonon coupling and non-equilibrium near the interface to interfacial thermal resistance: The multi temperature model and thermal circuit. *J. Appl. Phys.* **125**, 1–5 (2019).
83. Shi, J., Yang, X., Fisher, T. S. & Ruan, X. Dramatic increase in the thermal boundary conductance and radiation limit from a Nonequilibrium Landauer Approach. 1–19 (2018).
84. Omini, M. & Sparavigna, A. An iterative approach to the phonon Boltzmann equation in the theory of thermal conductivity. *Phys. B* **212**, 101–112 (1995).
85. Fugallo, G., Lazzeri, M., Paulatto, L. & Mauri, F. Ab initio variational approach for evaluating lattice thermal conductivity. *Phys. Rev. B* **88**, 045430 (2013).
86. Cepellotti, A. & Marzari, N. Thermal transport in crystals as a kinetic theory of relaxons. *Phys. Rev. X* **6**, 041013 (2016).
87. Hua, C. & Lindsay, L. Space-time dependent thermal conductivity in nonlocal thermal transport. *Phys. Rev. B* **102**, 1–10 (2020).
88. Landon, C. D. & Hadjiconstantinou, N. G. Deviation simulation of phonon transport in graphene ribbons with ab initio scattering. *J. Appl. Phys.* **116**, 163502 (2014).
89. Li, X. & Lee, S. Role of hydrodynamic viscosity on phonon transport in suspended graphene. *Phys. Rev. B* **97**, 94309 (2018).
90. Lee, S., Li, X. & Guo, R. Thermal Resistance by Transition Between Collective and Non-Collective Phonon Flows in Graphitic Materials. *Nanoscale Microscale Thermophys. Eng.* 1–12 (2019).

91. Ma, J., Li, W. & Luo, X. Examining the Callaway model for lattice thermal conductivity. *Phys. Rev. B* **90**, 035203 (2014).
92. Kresse, G. & Furthmüller, J. Efficiency of ab-initio total energy calculations for metals and semiconductors using a plane-wave basis set. *Comput. Mat. Sci.* **6**, 15–50 (1996).
93. Kresse, G. & Furthmüller, J. Efficient iterative schemes for ab initio total-energy calculations using a plane-wave basis set. *Phys. Rev. B* **54**, 11169 (1996).
94. Péraud, J. P. M. & Hadjiconstantinou, N. G. Efficient simulation of multidimensional phonon transport using energy-based variance-reduced Monte Carlo formulations. *Phys. Rev. B* **84**, 205331 (2011).
95. Peterson, R. B. Direct Simulation of Phonon-Mediated Heat Transfer in a Debye Crystal. *J. Heat Transfer* **116**, 815 (1994).
96. Mazumder, S. & Majumdar, A. Monte Carlo Study of Phonon Transport in Solid Thin Films Including Dispersion and Polarization. *J. Heat Transfer* **123**, 749 (2001).
97. Hao, Q., Chen, G. & Jeng, M. S. Frequency-dependent Monte Carlo simulations of phonon transport in two-dimensional porous silicon with aligned pores. *J. Appl. Phys.* **106**, 114321 (2009).
98. Landon, C. D. A deviational Monte Carlo formulation of ab initio phonon transport and its application to the study of kinetic effects in graphene ribbons. (2014).
99. Ziman, J. M. *Electrons and Phonons: The Theory of Transport Phenomena in Solids*. Oxford university press, London (Oxford university press, London, 1960).
100. Zhuomin Zhang. *Nano/Microscale Heat Transfer*. McGraw-Hill New York (2007).
101. Gupta, A. K., Russin, T. J., Gutie, H. R. & Eklund, P. C. Probing Graphene Edges via Raman. *ACS Nano* **3**, 45–52 (2009).
102. Lindsay, L., Broido, D. A. & Mingo, N. Flexural phonons and thermal transport in graphene. *Phys. Rev. B* **82**, 115427 (2010).
103. Lindsay, L. *et al.* Phonon thermal transport in strained and unstrained graphene from first principles. *Phys. Rev. B* **89**, 155426 (2014).
104. Lindsay, L., Broido, D. A. & Mingo, N. Flexural phonons and thermal transport in multilayer graphene and graphite. *Phys. Rev. B* **83**, 235428 (2011).
105. Carruthers, P. Theory of thermal conductivity of solids at low temperatures. *Rev. Mod. Phys.* **33**, 92–138 (1961).
106. Vincenti, W. G. & Kruger, C. H. *Introduction to Physical Gas Dynamics*. (Wiley, New York, 1965).

107. Mezhev-Deglin, L. P. Measurement of the thermal conductivity of crystalline He4. *J. Exp. Theor. Phys.* **49**, 66–79 (1965).
108. Bae, M.-H. *et al.* Ballistic to diffusive crossover of heat flow in graphene ribbons. *Nat. Commun.* **4**, 1734 (2013).
109. Cepellotti, A. & Marzari, N. Boltzmann Transport in Nanostructures as a Friction Effect. *Nano Lett.* **17**, 4675–4682 (2017).
110. Martelli, V., Jiménez, J. L., Continentino, M., Baggio-Saitovitch, E. & Behnia, K. Thermal Transport and Phonon Hydrodynamics in Strontium Titanate. *Phys. Rev. Lett.* **120**, 1–6 (2018).
111. Machida, Y. *et al.* Observation of poiseuille flow of phonons in black phosphorus. *Sci. Adv.* **4**, 1–10 (2018).
112. Lee, S. & Lindsay, L. Hydrodynamic phonon drift and second sound in a (20,20) single-wall carbon nanotube. *Phys. Rev. B* **95**, 184304 (2017).
113. Markov, M. *et al.* Hydrodynamic Heat Transport Regime in Bismuth: A Theoretical Viewpoint. *Phys. Rev. Lett.* **120**, 75901 (2018).
114. Tatsios, G., Stefanov, S. K. & Valougeorgis, D. Predicting the Knudsen paradox in long capillaries by decomposing the flow into ballistic and collision parts. *Phys. Rev. E* **91**, 061001 (2015).
115. Feng, T. & Ruan, X. Four-phonon scattering reduces intrinsic thermal conductivity of graphene and the contributions from flexural phonons. *Phys. Rev. B* **97**, 45202 (2018).
116. Knudsen, M. Die Gesetze der Molekularströmung und der inneren Reibungsströmung der Gase durch Röhren. *Ann. Phys.* **333**, 75–130 (1909).
117. Cercignani, C. & Daneri, A. Flow of a rarefied gas between two parallel plates. *J. Appl. Phys.* **34**, 3509–3513 (1963).
118. Greywall, D. S. Thermal-conductivity measurements in liquid 4He below 0.7 K. *Phys. Rev. B* **23**, 2152–2168 (1981).
119. Whitworth, R. W. Experiments on the Flow of Heat in Liquid Helium below 0.7 K. *Proceeding R. Soc. London Ser. A* **246**, 390–405 (1958).
120. Gurevich, V. L. *Transport in phonon systems.* (Elsevier Science Publishers, 1986).
121. Fuchs, K. The conductivity of thin metallic films according to the electron theory of metals. *Math. Proceeding Cambridge Philos. Soc.* **34**, 100–108 (1938).
122. Jeong, J., Li, X., Lee, S., Shi, L. & Wang, Y. Transient Lattice Cooling by Picosecond Laser Irradiation of Graphite due to Phonon Hydrodynamics (under review).

123. Kresse, G. & Joubert, D. From ultrasoft pseudopotentials to the projector augmented-wave method. *Phys. Rev. B* **59**, 1758–1775 (1999).
124. Klimeš, J., Bowler, D. R. & Michaelides, A. Chemical accuracy for the van der Waals density functional. *J. Phys. Condens. Matter* **22**, (2010).
125. Klimeš, J., Bowler, D. R. & Michaelides, A. Van der Waals density functionals applied to solids. *Phys. Rev. B - Condens. Matter Mater. Phys.* **83**, 1–13 (2011).
126. Togo, A. & Tanaka, I. First principles phonon calculations in materials science. *Scr. Mater.* **108**, 1–5 (2015).
127. Tian, F. *et al.* Unusual high thermal conductivity in boron arsenide bulk crystals. *Science (80-.).* **361**, 582–585 (2018).
128. Li, S. *et al.* High thermal conductivity in cubic boron arsenide crystals. *Science (80-.).* **361**, 579–581 (2018).
129. Kang, J. S., Li, M., Wu, H., Nguyen, H. & Hu, Y. Experimental observation of high thermal conductivity in boron arsenide. *Science (80-.).* **361**, 575–578 (2018).
130. Chen, K. *et al.* Ultrahigh thermal conductivity in isotope-enriched cubic boron nitride. *Science (80-.).* **367**, 555–559 (2020).